PaNTERA: Proton Radiography towards medical applications

PaNTERA: Proton Radiography towards medical applications
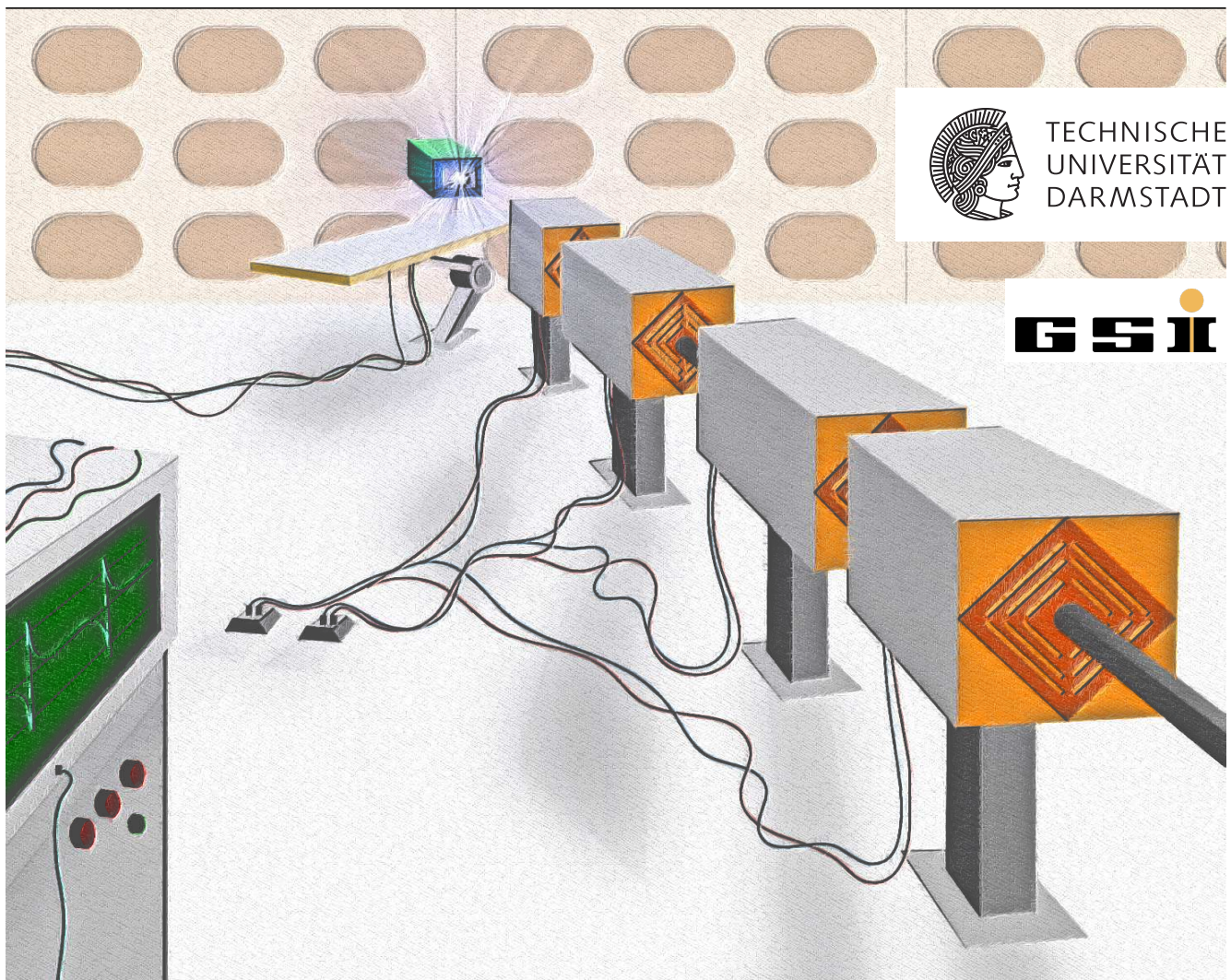PaNTERA: Protonenradiographie für medizinische Anwendungen

Genehmigte Dissertation von M.Sc. Martin Schanz aus Langen, Deutschland

1. Gutachten: PD Dr. Michael Krämer
2. Gutachten: Prof. Dr. Marco Durante

Tag der Einreichung: 12.04.2019
Tag der Prüfung: 17.6.2019

Darmstadt — D 17
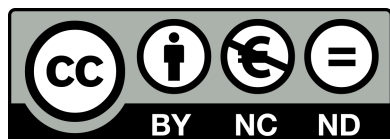
If things are not failing,
you're not innovating enough.
Elon Musk

Abstract

Heavy ion radiotherapy is an accepted form of cancer therapy especially suitable for the precise and effective treatment of tumors close to organs at risk. The high precision of the treatment is currently achieved by using patient geometry data captured using X-ray computed tomography. With the application of new imaging methods directly measuring the density and stopping power of the patient tissue the present accuracy could be further improved.

One of the promising alternatives to X-ray computed tomography is high energy proton radiography capable of providing a precise density analysis of target materials. Within the scope of this work several experimental approaches towards the effective accuracy of this technique regarding density reconstruction were made using different types of targets (simple step wedges and head phantoms). The investigations especially focused on the applicability of radiographic images for treatment planning based on either conventional X-ray data being recalibrated with the help of single proton projections or native proton computed tomography. All of the presented experiments were conducted during parasitic beam times at the LANL pRAD facility in New Mexico, USA. Several issues regarding the stability of the accelerator as well as the optical quality of the available detector systems were disclosed. Nevertheless, high energy proton radiography proved to deliver a more accurate density reconstruction than conventional calibration approaches.

Further investigations with the GSI in-house treatment planning software TRiP98 revealed a significant difference in dose coverage of a virtual tumor volume when using different patient base data (X-ray computed tomography vs. recalibrated X-ray computed tomography vs. proton tomography). Although the current clinical method provided a good result in soft tissue regions, at higher densities, e.g. in the density range of bones, a significantly larger deviation was monitored. This could in specific cases lead to an ineffective treatment of tumors or even to an unwanted dose deposition in healthy organs with the conventional imaging approach.

High energy proton radiography promises to be a suitable technique for medical imaging purposes. Although current facilities are not yet designed for such applications, future treatment centers could be designed in a way to exploit the benefits of this technique. Beforehand, several improvements and modifications to those setups will be mandatory to advance the technique towards clinical implementations. Future experiments for medical applications are scheduled for the FAIR phase 0. Those will focus on including a suitable method for measuring the stopping power of the incident particles. A quality comparison to X-rays at equal dose deposition is planned as well.

Zusammenfassung

Schwerionentherapie ist eine anerkannte Form der Tumortherapie, die sich auf Grund ihrer Präzision und Effektivität insbesondere zur Behandlung von Tumoren in der Nähe von Risikoorganen eignet. Ermöglicht wird diese hohe Genauigkeit durch Aufnahmen der Patientengeometrie mit Röntgentomographie. Durch den Einsatz von neuartigen Bildgebungsmethoden, die direkt die Dichte sowie das Bremsvermögen der verwendeten Ionen im Gewebe messen, kann diese Präzision weiter gesteigert werden.

Eine vielversprechende Alternative zu Röntgentomographie ist die hochenergetische Protonenradiographie, die eine präzise Dichterekonstruktion verschiedenster Materialien ermöglicht. Im Rahmen dieser Arbeit wurden verschiedene Untersuchungen hinsichtlich der Genauigkeit der Dichterekonstruktion von hochenergetischer Protoenenradiographie mit verschiedenen Targets durchgeführt (Stufentargets und Kopfphantome). Ein besonderer Fokus lag dabei auf der Eignung der aufgenommenen Radiographien zur Bestrahlungsplanung, welche sowohl mit rekalibrierten Röntgentomographien als auch mit Protonentomographien durchgeführt wurde. Alle Experimente fanden im Rahmen von parasitären Strahlzeiten an der pRAD Anlage des LANL in New Mexico, USA statt. Obwohl während der Durchführung der Experimente mehrere Schwierigkeiten mit der Stabiliät des Beschleunigers sowie den optischen Abbildungseigenschaften der Detektoren festgestellt wurden, konnte eine exaktere Dichterekonstruktion der Protonenaufnahmen gegenüber herkömmlichen rekalibrierten Röntgenaufnahmen nachgewiesen werden.

Weitere Untersuchungen mit der Bestrahlungsplanungssoftware der GSI (TRiP98) legten eine signifikant unterschiedliche Dosisabdeckung eines Tumors bei Verwendung unterschiedlicher Daten zur Patientengeometrie (Röntgen CTs gegenüber Protonen CTs) offen. Obwohl im Bereich der üblichen Dichten von Gewebe gute Ergebnisse mit der konventionellen Technik erreicht wurden, konnten signifikante Abweichungen bei höheren Dichten, wie man sie beispielsweise in Knochen vorfindet, beobachtet werden. Dieser Umstand kann in speziellen Fällen zu einer reduzierten Effektivität der Bestrahlung oder sogar zu einer ungewollten Dosisdeposition in gesundem bzw. Risikogewebe führen.

Hochenergetische Protonenradiographie verspricht eine vielversprechende Methode für die klinische Bildgebung zu werden. Obwohl aktuelle Anlangen noch nicht für derartige Anwendungen konzipiert sind, wäre eine Implementierung in zukünftigen Bestrahlungszentren zur Ausnutzung der Vorteile dieser Technik durchaus denkbar. Zuvor sind jedoch umfassende Modifikationen und Verbesserungen der Radiographieanlagen notwendig, um die Technologie reif für den klinischen Einsatz zu machen. Weitere Experimente zur medizinischen Bildgebung basierend auf dieser Methode sind bereits für die FAIR Phase 0 vorgesehen. Ein besonderer Fokus wird dabei auf einer geeigneten Methode zur Bestimmung des Bremsvermögens liegen,

ebenso ist ein Vergleich der Bildqualität mit Röntgentomographie bei gleicher Dosisdepostion im Patienten geplant.

Contents

Acronyms

AGS	Alternating Gradient Synchrotron
APPA	Atomic Physics, Plasma Physics and Applied Sciences
CDS	Correlated Double Sampling
CMOS	Complementary Metal-Oxide-Semiconductor
CT	Computed Tomography
DECT	Dual Energy Computed Tomography
DVH	Dose-Volume Histogram
FAIR	Facility for Antiproton and Ion Research
FOV	Field of View
GEM	Gas Electron Multiplier
GSI	Gesellschaft für Schwerionenforschung GmbH
HEDgeHOB	High Energy Density generated by Heavy Ion Beams
HHT	High Energy, High Temperature cave at GSI
HIAF	High Intensity Accelerator Facility, Huizhou, Guangdong, China
HIT	Heidelberger Ionenstrahl Therapiezentrum
HLUT	Hounsfield Lookup Table
HU	Hounsfield Unit
IMP	Institute of Modern Physics, Lanzhou, China
ITEP	Institute for Theoretical and Experimental Physics, Moscow
LANL	Los Alamos National Laboratory
LANSCE	Los Alamos Neutron Science Center
MC	Monte Carlo
MCS	Multiple Coulomb Scattering
MIT	Marburger Ionenstrahl Therapiezentrum
MLP	Most Likely Path
MRI	Magnetic Resonance Imaging
OAR	Organs at Risk
PaNTERA	Proton Therapy and Radiography
PMMA	Polymethylmethacrylat

PMQ	Permanent Magnet Quadrupole
POM	Polyoxymethylene
PUMA	Proton Radiography Setup with Magnetic Optics
PVDF	Polyvinylidene fluoride
PRIOR	Proton Radiography for FAIR
PROSIT	Proton Radiography Simulation Tool
QRM	Quality Assurance in Radiology and Medicine GmbH
SSD	Silicon Strip Detectors
TE	Tissue Equivalent
TOF	Time of Flight
VOI	Volume of Interest
WEPL	Water Equivalent Path Length

1 Introduction

Already in the first half of the last century the rapidly increasing number of cancer cases led to an increased awareness of the general public regarding one of the most complex diseases of modern humankind, cancer. In Germany alone, about 500.000 people are diagnosed with cancer annually, the annual mortality rate is around 230.000 people [1]. Those deceases are mostly correlated to spreading metastasis ($\sim 90\%$) and less often caused by the primary tumor itself. The reason for this is that cancer is frequently diagnosed in an advanced stadium where therapy is already complicated, expensive and less effective. Although cancer screening for most known types of cancer is covered by the German health system, the mortality rates are still increasing. However, the number of cancer cases discovered in an early stadium is also rising leading to an increased demand for modern and effective treatment methods.

Cancer, the *"epidemic plague of the 20th century"*[1].

This leads to a strong scientific community addressing cancer therapy by continuously advancing current techniques and developing new treatment methods. Common therapy forms currently available to patients are surgery, radiation therapy and chemotherapy which can be applied depending on the respective type of cancer. New developments in the fields of immunotherapy and gene therapy might become available during the next decades but require significantly more time for testing and approval.

Radiation therapy employing heavy ions instead of X-rays is a quickly growing sector, not only due to the outstanding results in terms of cancer control, it also causes less side-effects due to an effective sparing of healthy tissue. For this method antecedent patient imaging is a key factor since the precise planning of the delivered dose distribution is an individual procedure for every patient. The current state of the art technique for patient imaging is X-ray Computed Tomography (CT) which is widely available in hospitals and delivers a sufficiently good image quality for primary tumor diagnosis and treatment planning purposes. However, detecting metastases is mostly out of the scope of those machines without applying contrast agents. Another risk factor of this method is the possibility of a miscalculation of the actual tumor position caused by a unit conversion. This conversion – potentially containing deviations of up to several percent – is needed, as the X-ray CT delivers Hounsfield Units (HU) or photon absorption data whereas the treatment planning requires ion stopping power and tissue densities. Both issues can be addressed by the introduction of a new imaging technique suitable not only for cancer diagnosis but also for precise treatment planning. Several techniques are currently developed and evaluated regarding their potential for medical imaging purposes, one of which is high energy proton radiography.

---

[1] Cited from: Der Spiegel 28/1953, "Krebs - Die Krankheit der Epoche", original quote: "Zivilisationsseuche des 20. Jahrhunderts"

Modern proton radiography employing a lens system was first demonstrated in 1995 in the United States of America and motivated by the limited penetration capabilities of X-ray radiography for dense materials with military applications such as plutonium. Since the Manhattan Project, X-rays were the only diagnostics available for the analysis of dynamic experiments with materials driven by high explosives, which were the key factor towards the development of nuclear weapons. High energy proton radiography was then able to revolutionize the field by facilitating a precise and dynamic density analysis suitable for the development of accurate models for the design of novel nuclear weapons [2]. In this context it is – until today – mainly used for monitoring subcritical tests with e.g. plutonium after the USA did agree on the *Comprehensive Nuclear-Test-Ban Treaty* of the United Nation, which came into effect on September 10, 1996.

Despite the focus on the military sector, proton radiography proved to be capable of delivering an extremely precise density reconstruction even for small density differences, a capability which is also beneficial for medical purposes. This led to the launch of the Proton Therapy and Radiography (PaNTERA) project, a joint operation of the GSI and the LANL [3]. The collaboration is focusing on demonstrating the clinical applicability of this technique especially for cancer therapy. Whereas the first stage of the project focused on the general image quality in low density phantoms and preserved small animals, further experiments presented in this work were set up to investigate the dose deposition as well as the density reconstruction accuracy using simple wedge targets. Furthermore, using the proton beam directly for obtaining a full patient CT would completely redundantize the need of X-ray CT scanners for particle therapy and therefore the recalibration of X-ray images for proton or carbon ion therapy. This applicability for cancer treatment planning is also tested using clinical phantoms.

2 Scientific Background

2.1 Heavy ion tumor therapy

Cancer radiotherapy exploiting X-rays is practiced since the late 1890s [4] and nowadays widely-used in clinics mainly due to the compact size of therapy machines and low operation costs. However, the interaction properties of X-rays with matter – here patients – are not necessarily favorable as the dose deposition depending on the penetration depth reaches its maximum already at small depths (see Fig. 2.1, red curve) which may lead to a significant damage of healthy tissue in the entrance channel in front of the tumor. Ions instead show a much more favorable interaction characteristic with matter, the so-called Bragg peak. Depending on the material properties and the initial energy of the penetrating ions the maximum of the dose deposition curve is situated at the end of the range of those particles. This means that the dose maximum can be localized in the tumor volume by adjusting the kinetic energy of the ions resulting in a sparing of healthy tissue in the ion's entrance channel as well as behind the tumor volume. As this volume is usually larger than the dimension of a single Bragg peak, several peaks can be overlapped. This is demonstrated in Fig. 2.1 where several single Bragg peaks are combined to form a uniform dose distribution in the tumor volume.

The use of ions or protons for medical applications due to the favorable dose distribution has already been postulated by Wilson during the mid 1940s [5]. However, compact particle accelerators covering the required energy range from 60 up to around 250 MeV were not available at that time. One of the first clinical applications was conducted at the Harvard Cyclotron Unit during the 1960s starting with a clinical trial on apes [6]. Those early setups were based on *passive beam modulation* where the size of the beam was adjusted using collimators and the energy could be lowered by using degrader plates mostly from plastics. In contrast to those early efforts modern ion therapy uses *active beam modulation* as well as *rasterscanning*. Here the kinetic energy of the ions is adjusted directly by the synchro- or cyclotron. Instead of a broadened beam, a pencil beam with a diameter in the mm-range is used for the irradiation. By installing two fast dipoles upstream of the patient location the beam can be deflected horizontally and vertically to scan slices perpendicular to the beam axis [7]. This intensity modulated ion therapy allows the scanning and therefore treatment of arbitrary tumor geometries and sizes limited only by the penetration depth of the used ions.

The German implementation of this technique has been developed in the 1990s at GSI using carbon ions for treatment [8]. Compared to protons carbon ions are heavier and therefore experience less deflection due to scattering in matter. This reduces the final volume of the highest dose deposition of a single Bragg peak making carbon ion therapy more precise than proton therapy. However, in contrast more target fragments are created leading to an unwanted
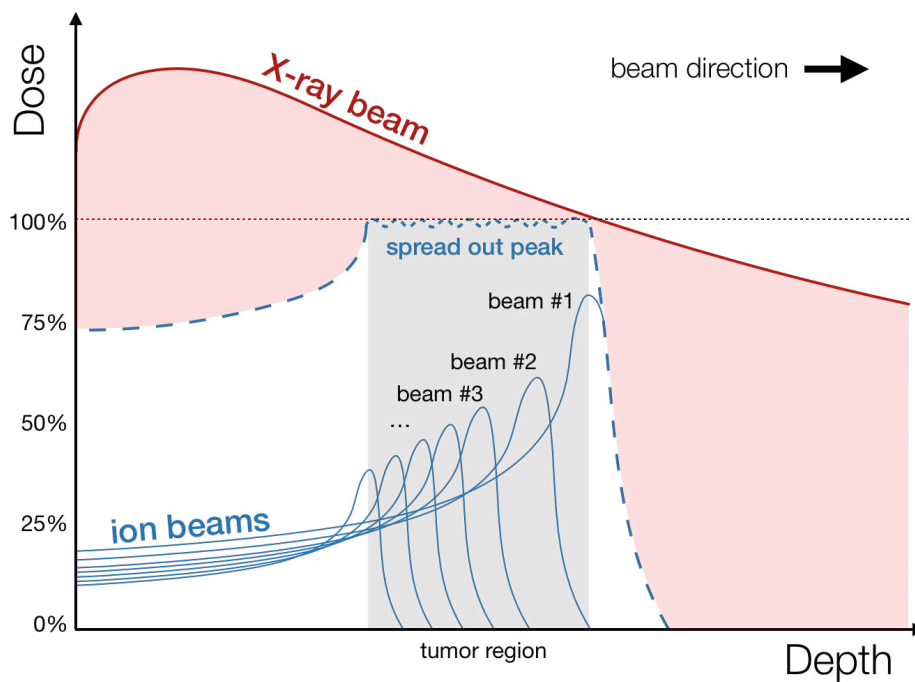
Figure 2.1.: Qualitative dose deposition of X-rays vs. dose deposition of ions in matter. The uniform dose coverage with ion beams is achieved by overlapping several Bragg peaks with a different beam energy and therefore different penetration depth. The red area shows the unwanted overdose of X-rays to healthy tissue compared to ion beam therapy.

dose tail on the beam axis behind the tumor region. On the biological side carbon ions also show a higher biological effectiveness more suitable for killing (cancer) cells towards the end of their range [9, 10].

Up to now a huge number of patients has already experienced the benefits of proton or heavy ion radiotherapy, until 2016 almost 175.000 patients were treated [11]. The majority of those treatments was performed using protons (about 85.6 %) followed by carbon (12.4 %). Other particles such as Helium, Pions or even heavier elements have not been used clinically since 1994, this however may change during the next years. Recent studies have shown that the cell killing effectiveness of different ion species is dependent on the oxygen content in tissue. This so-called *oxygen effect* may partly be overcome by multi ion treatment plans which then increase the total biological effectiveness due to the different radiosensitivity of tumor tissue [12].

2.2 Medical imaging - The concept of X-ray CT

Patient imaging is one of the essential requirements for heavy ion tumor therapy as it is the only way to localize the tumor tissue non-invasively inside the patient. In contrast to other treatment methods, heavy ion tumor therapy requests a high precision imaging method as the treatment procedure itself allows a very precise irradiation even close to organs at risk (OAR). Next to Magnetic Resonance Imaging (MRI) the most common diagnostics facilitating full-body imaging in the clinical environment is X-ray CT.

2.2.1 A brief history of X-ray CT

Following the discovery of X-rays in 1895 by the German scientist Wilhelm Conrad Röntgen [13] the mathematical basis for tomographic reconstruction was already developed in 1917 by Johann Radon [14] with the discovery of the Radon transformation. Although the technical capabilities and therefore the quality of X-ray images did significantly increase during the following years, the lack of sufficient computational power of early computers prevented the development of X-ray tomography until the concept was individually investigated again by the South African scientist Allan MacLeod Cormack since 1963 and by the British scientist Godfrey Newbold Hounsfield since 1967. Cormack – a theoretician – solved the reconstruction issue analytically and proved its applicability using a self-made scanning device [15]. Independently, Hounsfield developed a way of solving the reconstruction algorithms using computational power which effectively was the first practical application of computed tomography [16]. This first approach was carried out using gamma rays which led to an extremely long data acquisition time due to low counting statistics. However, Hounsfield quickly switched from gamma rays to X-rays during the clinical trials which finally led to the construction of the first clinical X-ray CT device, the *EMI Mark I* scanner.

Since the construction of the first device further investigations subsequently led to an increased reconstruction performance, better image quality and more captured slices within a single measurement. From just $80{\times}80\,\text{pixel}^2$ and a single slice, clinical scanners have evolved and can now deliver up to $4\,\text{Mpx}$ and capture around $320\,\text{slices}$ at once. An overview of the recent developments on *Dual Energy CT* further improving the accuracy and image quality of X-ray CT is presented in Sec. 2.2.4.

2.2.2 X-ray interactions and the Hounsfield scale

The attenuation of X-rays in matter can be described by the exponential attenuation law (Beer-Lambert law) which reads

$$I = I_0 \cdot e^{-\mu x}. \tag{2.1}$$

Here I_0 is the incoming intensity, x the material thickness and μ the linear attenuation coefficient of X-rays in the target matter which is in turn defined as $\mu = \mu_m \cdot \rho$ with the mass attenuation coefficient μ_m and the target density ρ. The mass attenuation coefficient can be calculated by

$$\mu_m = \frac{\sigma_{\text{tot}}}{u \cdot A} \tag{2.2}$$

with the atomic mass unit u and the relative atomic mass A of the target. σ_{tot} is the total cross section describing all of the interaction processes of X-rays with matter. It is plotted in Fig. 2.2 for the different interaction processes depending on the photon energy. Considering the energy

range of clinical X-rays from several keV up to around 140 keV, the dominating processes in this region are the Photoelectric effect and the Compton effect which are depicted in Fig. 2.3.
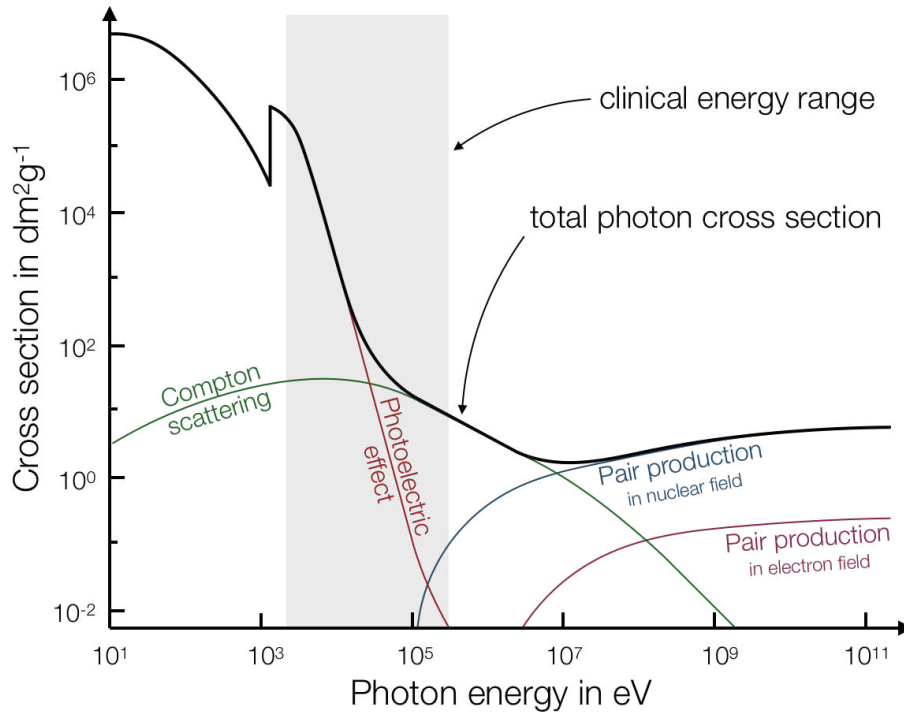
Figure 2.2.: Total cross-section of the interaction of X-rays with matter including the influence of the individual interaction processes for the corresponding energy range.

Photoelectric effect

The Photoelectric effect describes the process of an incoming photon transferring all of its energy to an electron sitting in an inner shell (mostly K-, also L-shell) of the target atom. The photon is absorbed during this process and the electron is ejected from the atom (see Fig. 2.3(a)). Its kinetic energy is equal to the difference between the total energy $h\nu$ of the incoming photon and the binding energy of the electron. The gap in the shell is filled again with an electron of an outer shell. This process is accompanied by the emission of another photon in the energy range of X-rays since the potential of the inner shells is lower than the one of the outer. The probability τ of this process can roughly be described by

$$\tau \propto \frac{Z^n}{(h\nu)^3} \tag{2.3}$$

where Z is the charge of the target atom and $h\nu$ its energy. n may vary between 4 and 5 depending on the energy of the incoming photon [17].

Compton effect

The Compton effect – shown in Fig. 2.3(b) – describes the collision of a X-ray photon and an electron of an outer shell of an atom with a small binding energy. The photon transfers part of its energy to the electron which is ejected from its shell. This ionization process of the atom and scattering of the incoming photon is also referred to as incoherent scattering. The cross section

for this process can be obtained by integrating the Klein-Nishina angular distribution function leading to the Klein-Nishina cross section [17].

Summing up the statements above and considering the energy range of clinical X-rays we can conclude:

$$\text{The Photoelectric effect varies as} \sim \frac{Z^4}{E^3} \tag{2.4}$$

$$\text{The Compton effect varies as} \sim Z \tag{2.5}$$

(a) Photoelectric effect.   (b) Compton effect.
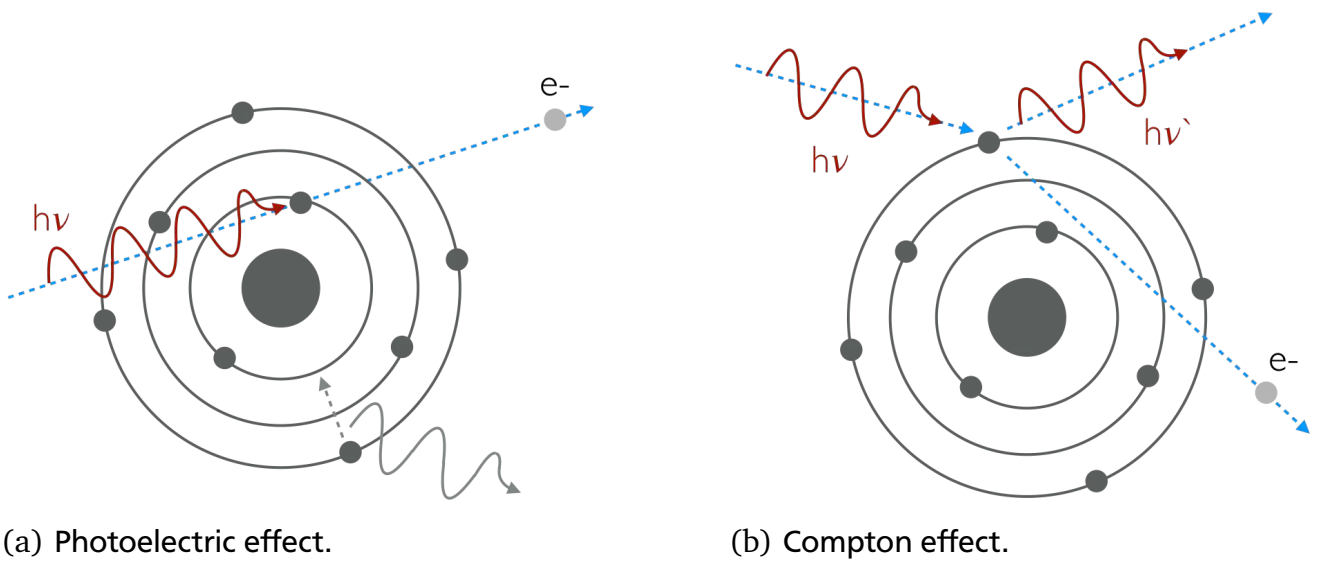
Figure 2.3.: Schematic representation of the two main interaction processes relevant for clinical X-ray imaging.

In effect, X-ray CT machines measure the linear attenuation coefficient μ of a probe. The scale on which the result is presented is called the *Hounsfield scale* (see Eqn. 2.6), named after one of the inventors of X-ray CT. The basis of the scale is the linear attenuation coefficient of water, therefore water will produce a HU or CT number of 0. As most types of organic tissue contain lots of water the HU values are situated close to 0 in an interval of about -100 to 100, more dense structures like bone may reach a HU up to 2000.

$$\text{HU} = \frac{\mu - \mu_{\text{water}}}{\mu_{\text{water}}} \cdot 1000 \tag{2.6}$$

2.2.3 WEPL, HLUT and stopping power calculation

For exploiting the full precision of heavy ion tumor therapy a precise knowledge of the patient geometry is mandatory. Treatment planning requires an accurate map of the particle range in and in front of the target volume to precisely calculate the mandatory energy of the accelerated

particles to optimize the applied dose. The base value chosen for the calculation is the so-called water equivalent path length (WEPL) defined in Eqn. 2.7.

$$l_{\text{WEPL}} = \frac{t_{H_2O}}{t_m} = \frac{\rho_m}{\rho_{H_2O}} \cdot \frac{\overline{S_m(E)}}{\overline{S_{H_2O}(E)}} \qquad (2.7)$$

Here ρ are the corresponding densities and $\overline{S}$ the mean stopping power values of the target material and water, respectively. The mean stopping power is in turn defined by

$$\overline{S} = \frac{\int_E S dE}{\int_E dE}. \qquad (2.8)$$

We can divide the target material into several slabs oriented perpendicular to the beam axis. This allows for the assumption that such a slab is a *radiologically thin* object which leads to a constant fractional energy loss ΔE. This simplification is acceptably accurate for describing materials like polymethylmethacrylat (PMMA) or water but not suitable for heavier elements such as metals [18]. For thin targets $\overline{S(E)} \approx S$ holds and the integration in Eqn. 2.8 can be skipped leading to the thin-target approximation of Eqn. 2.7:

$$l_{\text{WEPL}} = \frac{\rho_m}{\rho_{H_2O}} \cdot \frac{S_m}{S_{H_2O}}. \qquad (2.9)$$

The stopping power of ions inside the target material can in turn be calculated from the electron density of a various material by using the Bethe-Bloch formula in Eqn. 2.10.

$$-\frac{dE}{dx} = \frac{4\pi k_0^2 z^2 e^4 n_e}{m_e c^2 \beta^2 \rho} \left[\ln \frac{2 m_e c^2 \beta^2}{I(1 - \beta^2)} - \beta^2 - \frac{\delta(\beta)}{2} - \frac{C(\beta)}{2} \right] \qquad (2.10)$$

$$k_0 = 8.99 \times 10^9 \text{Nm}^2\text{C}^{-2}$$
$$z = \text{atomic number of the projectile}$$
$$e = \text{electron charge}$$
$$n_e = \text{electron density of the medium}$$
$$m_e = \text{electron mass}$$
$$c = \text{speed of light}$$
$$\beta = \frac{v}{c} = \text{relativistic beta factor}$$
$$\rho = \text{density of the medium}$$
$$I = \text{mean excitation energy in eV}$$

$$I \approx \begin{cases} 19.0 \text{ eV}, & Z = 1 \text{ (hydrogen)} \\ 11.2 + 11.7 \cdot Z \text{ eV}, & 2 \leq Z \leq 13 \\ 52.8 + 8.71 \cdot Z \text{ eV}, & Z > 13. \end{cases} \tag{2.11}$$

Correction terms added to the original Bethe-Bloch formula are the *density correction* $\delta(\beta)$ describing the shielding of remote electrons, which leads to a reduced energy loss in case of higher energies, and the *shell correction* $C(\beta)$ only relevant in case of very low energies. At proton energies of 250 MeV or above both terms are approximately zero [18, 19] and can be neglected. However, close to the Bragg peak those terms have a significantly larger influence and need to be considered for a precise range prediction in therapy applications.

The mean excitation energy I for several materials can be obtained from measurements where all of the other quantities are known [20]. This approximation is comparably accurate as the stopping power does have just a logarithmic dependence on I. With the approximation presented in Eqn. 2.11 the excitation energy can be roughly predicted for any element with atomic number Z.

In case of a compound an additive rule applies as presented in Eqn. 2.12.

$$\ln(I) = \frac{1}{n_e} \sum_i N_i Z_i \ln(I_i) \tag{2.12}$$

Here n_e is the electron density of the compound material and i describes the corresponding element of the compound with the individual electron densities $N_i Z_i$. This drastically simplifies the calculation as just the number of electrons has to be considered to calculate the ratios $\frac{N_i Z_i}{n_e}$. E.g. for H_2O with H ($Z = 1$) and O ($Z = 8$) we obtain $I = 74.6$ eV using the above formulas.

Starting from the original Bethe-Bloch formula we can rewrite Eqn. 2.10 to

$$-\frac{dE}{dx} = \frac{5.8 \times 10^{-31} z^2 n_e}{\beta^2 \rho} [F(\beta) - \ln(I)] \tag{2.13}$$

using the term $F(\beta)$ dependent just on the particle energy.

$$F(\beta) = \ln\left(\frac{1.02 \times 10^6 \beta^2}{1 - \beta^2}\right) - \beta^2 \tag{2.14}$$

E.g. for a proton energy of 800.0 MeV we get $\beta = 0.7088$ and correspondingly $F(\beta) = 14.02$.

In case of conventional X-ray CT providing just HU values or attenuation coefficients there is practically no possibility to accurately determine the WEPL required for the ion beam treatment planning. Therefore, a so-called Hounsfield lookup table (HLUT) is defined in advance, mapping the HU values to WEPL values. This calibration curve is basically a linear interpolation of several experimentally obtained data points. In clinics, e.g. at the HIT, it is usually recorded by imaging a clinical phantom with several insets made from tissue equivalent (TE) types of plastics with slightly different but well known characteristics. A different approach was conducted for the therapy pilot project at GSI where real organic matter was used instead [21]. This

procedure delivers more accurate results but is at the same time more complicated in terms of handling. The accuracy of a conventional clinical lookup table is therefore limited and is in general believed to be around 3 % in the tissue density range [22]. Especially in case of higher densities encountered in bones this accuracy may worsen. This can – in the worst case scenario – lead to a range uncertainty of the treatment ions in the mm-range increasing the required safety margins around the actual tumor volume in order to guarantee a complete dose coverage of the irradiated volume. Furthermore, it has to be considered that the use of a calibration curve will always lead to errors as it is possible to obtain the same WEPL with different density and stopping power combinations.

2.2.4 Recent developments in X-ray imaging

New X-ray machines employ a technique known as dual energy CT (DECT) where two independent X-ray sources and correspondingly two detector systems are used. Both sources produce photons with a different energy, e.g. 80 keV and 140 keV, which drastically improves the reconstruction accuracy of the targets' electron density n_e and also allows to perform a material decomposition. This is possible due to the different response of the target material at different photon energies [23]. A simple method for calculating the electron density is e.g.

$$n_e = a \frac{((1+\alpha)\mathrm{HU}_H - \alpha\mathrm{HU}_L)}{1000} + b \tag{2.15}$$

with the HUs from the **H**igh and **L**ow energy source and the fit parameters a, b and α which have to be determined in advance for the machine. The accuracy of this method was determined to be around 1 % [24]. Correspondingly the effective charge number of the target material can be accessed by

$$\frac{\mathrm{HU}_L \cdot 10^{-3} + 1}{\mathrm{HU}_H \cdot 10^{-3} + 1} = \frac{1 + A \cdot Z_{\mathrm{eff}}^{m-1}}{B + C \cdot Z_{\mathrm{eff}}^{m-1}} \tag{2.16}$$

with the fit parameters A, B, C and m [25]. This method showed an accuracy around 3 %.

The use of DECT is especially beneficial for treatment planning for heavy ion therapy as it is then possible to overcome the conventional treatment planning method which makes use of the inaccurate HLUT. Recent studies on the recalculation of treatment plans on DECT data instead of mono-energetic X-ray CTs revealed a shift of the treated volume by almost 2 mm [26]. Furthermore, a considerably better image quality with less noise was observed [27].

2.3 Proton radiography

High energy proton radiography – also referred to as *proton microscopy* when using magnifying lens setups – is a unique diagnostic technique for high energy, high density scenarios such as material properties in extreme conditions. Due to the large penetration depth and simultaneously small scattering of high energy protons in matter (see Sec. 2.3.6) proton radiography

is capable of probing extremely thick and dense objects. By using a chromatic lens system it is furthermore possible to introduce a correction of chromatic aberrations which leads to a spatial resolution performance on the micrometer scale. Exploiting the capability of current accelerators to provide a pulsed beam structure it is furthermore possible – using a sufficiently fast detector system – to capture time resolved radiographies and to observe fast processes in extreme dynamic environments such as e.g. the propagation of shock waves in various matter.

This enables a huge variety of applications in plasma physics, material sciences, weapons development and in biophysics. Especially for the latter one proton radiography may offer large benefits due to short image capture times, good spatial resolution performance and an accurate density reconstruction of the target volume. This is currently of huge interest as ongoing investigations on improving heavy ion tumor therapy focus on new imaging methods for overcoming the inaccurate HLUT (see Sec. 2.2.3). Proton radiography – along with DECT (Sec. 2.2.4) and single proton tracking (Sec. 2.3.2) – is currently one of the most promising alternatives to the conventional mono-energetic X-ray CT imaging.

2.3.1 History and concept

Although the first proposal for using ions for the purpose of (medical) imaging dates back to the first half of the last century [5] the first actual radiographic images captured with protons just date back to the late 70s and make use of a concept better known as *Marginal Range Radiography* [28]. This technique requires an adjustment of the energy of the incoming protons to the corresponding target properties. Contrast can be obtained by tuning the proton energy to a level where part of the protons are stopped in the thicker or more dense areas of the target to achieve image contrast. This can either be achieved by active modulation of the beam energy or by absorbers placed in front of the object. A simple radiographic plate placed right after or very close to the object serves as a detector. Although this concept is capable of delivering a good image contrast it is not favorable for quantitative evaluation of the captured image as the protons being stopped in the target do not contribute to the final image and therefore cannot provide any information about those parts of the target. A radiography of a thin leaf using this particular technique is shown in Fig. 2.4(a).

A later attempt – introduced by J.A. Cookson – was the exploitation of the proton scattering for achieving contrast [29]. Here the concept was, that the more dense areas of the target cause larger proton scattering angles which in turn lead to less illuminated areas at the detector. This so-called *Scattering Radiography* delivered an extremely good image quality especially when probing fine structures as the transition between optically thicker and thinner parts of the target is boosted by the limning effect (see Sec. 2.3.6). This can be observed in Fig. 2.4(b), especially the petiole of the leaf is clearly visible due to an outline caused by this effect.

Both initial techniques were discussed by Koehler, Cookson [30] and later West [31] and not reviewed favorably in comparison to state of the art X-ray imaging at that time. The captured radiographic images with protons mostly suffered from a poor image quality due to multiple coulomb scattering (MCS) in the target which led to an even worse image quality when increasing the distance from the radiographed object to the detector. As X-ray imaging was a much
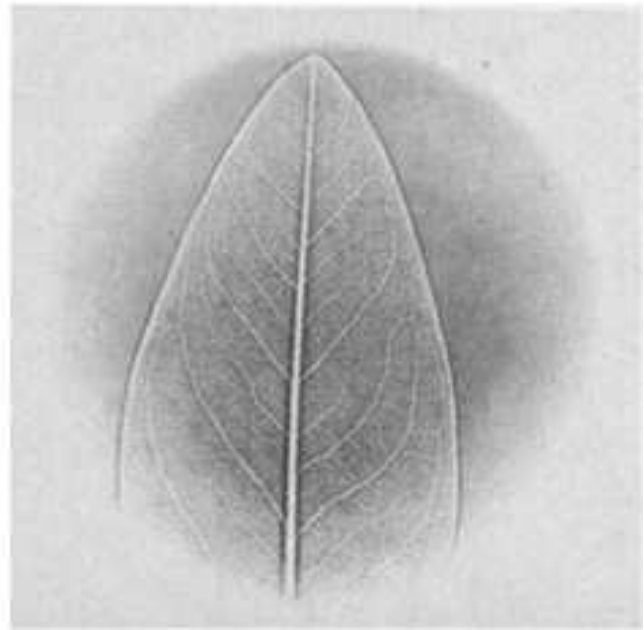
(a) Marginal Range Radiography.   (b) Scattering Radiography.

Figure 2.4.: Comparison between radiography exploiting the energy loss of particles in matter (left) and scattering (right) [29].

more powerful diagnostics and offered a much better spatial resolution performance for thin or low-density objects (i.e. biomedical applications) most investigations on proton imaging were stopped at that time.

An new concept developed at the LANL during the 1990s led to a major improvement of the image quality as the utilization of a chromatic lens system allowed for the correction of the worst 2nd order chromatic aberrations caused by MCS. This simple magnetic lens system in a 'Focusing - Defocussing - Focusing - Defocussing' configuration, creates – in a so-called *matched configuration* – a Fourier plane roughly in the geometric center of the setup which allows for the adjustment of the image contrast by inserting collimators with different acceptances (see Sec. 2.3.3). Since the remaining chromatic image distortions are mainly caused by the energy spread of the beam exiting the target the choice of high energy protons in the GeV range is obvious. In comparison to conventional X-ray techniques those particles are even capable of traversing and probing extremely thick or high-Z materials. Given an accelerator with the capability of providing a timed pulse structure it is possible to visualize dynamic processes such as the propagation of shock waves on the nanosecond scale.

The first radiographic setup of this kind – pRad – was installed at the 800 MeV LANSCE linac of the LANL facility [32], another one using 800 MeV protons was built at the ITEP accelerator in Moscow. The latter one – the PUMA [33, 34] system – is currently not operational. For scientific and commercial experiments using proton radiography as a diagnostics only the pRad system at LANL is available.

A third high energy proton radiography setup utilizing protons up to 50 GeV from the U-70 synchrotron in Protvino, Russia, is capable of penetrating thick materials with a density of up

to >300 g/cm^2 while providing a field of view (FOV) of roughly 60 x 60 mm^2 [35]. Similar experiments with high energy protons up to 24 GeV from the AGS in Brookhaven were conducted by the American team of scientists responsible also for the pRad facility [36]. This setup uses – similar to the one at the LANL – a tantalum diffuser introduced upstream of the target location and matching section to achieve a sufficient beam broadening. This is mandatory to fill the acceptance and therefore FOV of the large aperture electromagnets which allow the imaging of large (up to 120 x 120 mm^2) and thick (density >200 g/cm^2) objects.

In Germany, the PRIOR collaboration was founded in 2009 combining the efforts of the American pRad team at LANL and the Russian Proton Radiography team from the ITEP. The prototype microscope PRIOR-I was developed and commissioned in 2014 at GSI in Germany (see Sec. 2.4) [37]. Since 2014 there are also ongoing efforts to bring proton radiography to the IMP in Lanzhou, China, [38–40] however, up to now it is unclear whether such a project will or could be realized there or at the new HIAF [41, 42] in Huizhou, Guangdong Province, China.

2.3.2 Other radiographic techniques employing ions

Charged particles or ions are highly favorable for imaging mainly due to their physical properties. They can easily be detected by simple detectors and their interaction characteristics with matter are well known. Therefore, it is not surprising that, except from high energy proton radiography, there are several other methods using protons or other sorts of ions for imaging purposes, some of which are presented in this section.

Single Proton Tracking
The currently most common approach for medical imaging with heavy ions is the *Single Proton Tracking* requiring a set of tracking detectors as well as a detector for energy loss measurements (range telescope) behind the patient. The concept is to first measure the proton scattering angle with the help of the two tracking detectors placed in front and right behind the patient. By recording the proton positions at both locations (x_0,y_0) and (x_1,y_1) (see Fig. 2.5) a reconstruction of the occurred scattering is possible using *most likely path* (MLP) approximation methods. This enables the reconstruction of the object density using the Moliere theory. With the help of the range telescope the remaining energy (stopping power) of the corresponding proton can be determined. Both quantities can then be used for the accurate calculation of the WEPL.

The tracking approach is very popular since experiments can be conducted at the energy range of most clinical accelerators, in addition there are no requirements on the incoming beam. Especially the latter condition is important as most facilities treating patients prohibit any variation of the beam line settings even when using dedicated, separate beam lines only for experiments.

First experiments date back to 2004 where the concept was tested with a dog patient [43]. For those early experiments scintillating fiber hodoscopes were used for the particle tracking. Newer experiments are still based either on this type of detector [44] but also make use of silicon strip detectors (SSD) [45] or gas electron multipliers (GEM) capable of a sub-mm spatial track
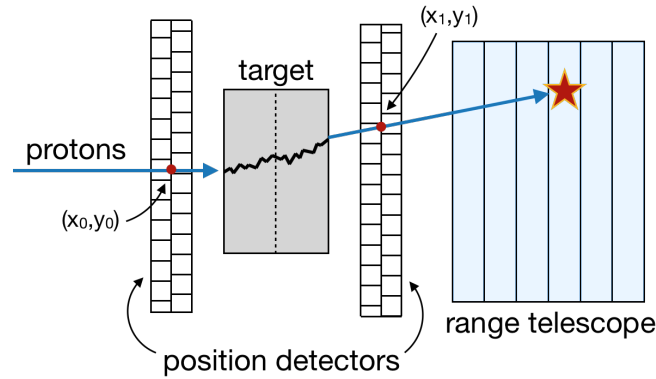
Figure 2.5.: Detector configuration for the single proton tracking approach.

reconstruction [46]. For the energy loss measurements either conventional plastic scintillators [47] or crystal calorimeters, both in combination with photomultipliers, are used [48]. This drastically reduces the speed of the data acquisition as only single protons can be detected by this type of detector. A new approach makes use of pixelated CMOS detectors [49]. Those detectors would also allow direct imaging without using tracking detectors as they can measure not only the remaining energy but also the spatial position of the Bragg peak. A simple approach with this technique was performed using carbon ions and a flat-panel detector at the HIT in Heidelberg [50].

Single proton tracking is a promising technique for future clinical applications, however, recent experiments suffer from several issues which currently prevent any clinical application. First, the data acquisition time is determined by the speed of the tracking and range detectors as well as the used MLP method. The speed of the detectors then determines the maximum particle flux which currently leads to a total acquisition time for a CT around several minutes [51]. It has to be noted that this is already way below the speed of the first scanning devices needing about 12 hours for a full CT scan. Furthermore, the accuracy of the MLP methods is mainly determined by the amount of MCS. Due to the low particle energies of clinical accelerators the air gaps around the target/patient significantly affect the scattering requiring a placement of the detectors as close as possible to the object. This is severely constricting the patient making him uncomfortable during the data acquisition. Finally, the image quality of current setups, defined of course by the spatial resolution capabilities of the tracking detectors, is currently in the mm-range, not better than X-ray CT. A better resolution performance would require better detectors which will again reduce the speed of the whole process.

Dual Energy Proton Radiography

Based on the historical concept of proton radiography already described in Sec. 2.3.1 a prototype setup for small animal treatment planning and position verification was built and tested at the OncoRay in Dresden [52]. The facility uses both *Scattering Radiography* and *Marginal Range Radiography* for obtaining images of a mouse patient at an ion energy of about 150 MeV. The dual energy approach enables the differential enhancement of object features. Despite a poor spatial resolution performance caused by multiple coulomb scattering several key features of

the mouse such as the stomach, the lung and the spine could be identified and used for image registration. Furthermore, the technique allowed for the reconstruction of a relatively accurate WEPL map in beam direction complementing the information obtained by conventional X-ray measurements. It is intended to repeat the measurements with increased proton energies up to 230 MeV to decrease the influence of the MCS and subsequently increase the overall image quality.

Heavy Ion Microlithography

Heavy Ion Microlithography is a technique that was developed and tested at GSI in the 1980s [53]. It employs a method which is known from the development of semiconductor wafers prior to etching but – in contrast to the conventional approach with X-rays – makes use of ions. For this, the object of interest is placed on a nuclear track sensitive material such as PMMA and irradiated with ions up to 1 MeV. This produces a lateral track structure in the upper surface which can later be removed by etching to obtain a replica of the original object. The range of the lateral tracks in the surface is determined by the remaining energy of the incident ions exiting the object of interest. Therefore, the height of the replica is correlated to the material properties of the investigated target. After etching the replica can be investigated using scanning electron microscopy. Heavy Ion Microlithography is suited for investigations of extremely small structures, the theoretical resolution limit is around 100 Å.

2.3.3 Ion optical theory

High energy proton radiography requires a specific beam line / magnet configuration often referred to as 'Russian Quadruplet' [54], which is a symmetric system of four quadrupoles. The outer two (A - Q_1,Q_4) as well as the inner two (B - Q_2,Q_3) lenses have the same strength but are alternatingly **F**ocusing and **D**efocusing. This configuration is often visualized as A_F B_D B_F A_D, a schematic example configuration including the most common installation of the detector setup employing a scintillation detector and a camera setup is shown in Fig. 2.6.

For describing the motion of a charged particle traveling through this setup, first, the force acting on a charged particle by electric or magnetic fields – the Lorentz force – has to be considered which is determined by the expression

$$\vec{F} = q \cdot (\vec{E} + \vec{v} \times \vec{B}). \tag{2.17}$$

The vector product in Eqn. 2.17 indicates that this force is dependent on the orientation of the velocity vector of the particle. Therefore, the total force is never axially symmetric and has to be considered in both the $\vec{x}$- and $\vec{y}$-plane perpendicular to the beam axis $\vec{z}$. An overview of all of the different coordinates in the widely used TRANSPORT notation [55] suitable for describing such problems is given through the convention

coordinate	number	description
x	1	x-coordinate
a	2	p_x/p
y	3	y-coordinate
b	4	p_y/p
t	5	time
δ	6	energy spread

In this section only the $\vec{x}$-plane is considered, the calculation can be performed analogous for the $\vec{y}$-plane. The position and direction of motion of a particle in the $\vec{x}$-plane can in first order be described by a vector

$$\vec{X}_o = \begin{pmatrix} x_o \\ \tan(a_o) \end{pmatrix} \tag{2.18}$$

containing the position of the particle x_o relative to the $\vec{z}$-axis and the tangent of the angle a_o between the particle's trajectory in this plane and the $\vec{z}$-axis equaling the beam axis. In par-axial approximation we can furthermore assume small angles a_o and therefore $\tan(a_o) \sim a_o$. The angle is then determined by the ratio of the particle momenta $a_o = p_x/p$.
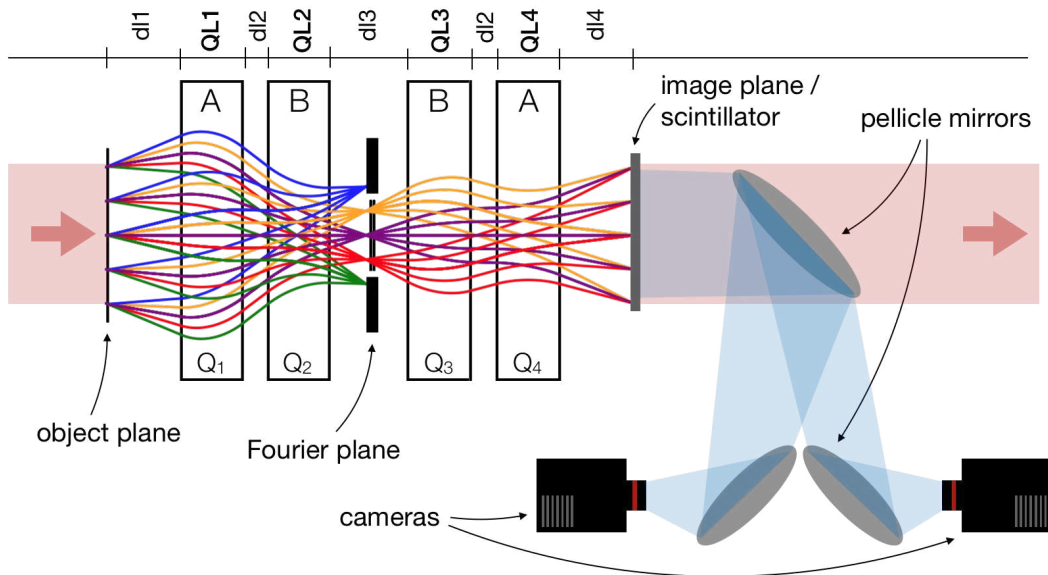
Figure 2.6.: Visualization of a typical beam line configuration for proton radiography. The plotted quadruplet is an identity lens not providing any magnification (m=1), the rays were simulated using COSY INFINITY (see Sec. 3.3.1). The displayed detector setup consists of a scintillation detector which can be observed by several cameras using pellicle mirrors. A detailed description of the respective detector setups used is given in Sec. 3.1.3.

A manipulation of the particle's trajectory, in this case by a magnetic lens, can be described by a first order transfer map **R**. This can be written as

$$\begin{pmatrix} x_i \\ a_i \end{pmatrix} = \begin{pmatrix} (x|x) & (x|a) \\ (a|x) & (a|a) \end{pmatrix} \cdot \begin{pmatrix} x_o \\ a_o \end{pmatrix} = \underbrace{\begin{pmatrix} R_{11} & R_{12} \\ R_{21} & R_{22} \end{pmatrix}}_{\textbf{R}\text{-matrix}} \cdot \begin{pmatrix} x_o \\ a_o \end{pmatrix} \tag{2.19}$$

or in summation notation as

$$\vec{X}_i = \sum_j R_{ij} \cdot X_{j,o} \tag{2.20}$$

where $\vec{X}_o$ is the initial particle coordinate at the object plane and $\vec{X}_i$ the one at the image plane after passing the optical element described by **R**.

Neither the incoming beam nor the beam exiting the object plane is mono-energetic (caused by an initial non-zero beam energy spread as well as by energy loss straggling in the object), therefore, the 6th coordinate from the coordinate table, the energy spread $\delta = \Delta E / E$, does not equal zero. It is mandatory to expand the expression from Eqn. 2.20 to second order terms. Introducing the second order transfer matrix, the **T**-matrix [55], the expression 2.20 can be rewritten to

$$\vec{X}_i = \sum_j R_{ij} \cdot X_{j,o} + \sum_{jk} T_{ijk} \cdot X_{j,o} \cdot X_{k,o}. \tag{2.21}$$

Note, that in case of quadrupole magnets only the $(x|x\delta) = T_{116}$ and $(x|a\delta) = T_{126}$ terms remain in the second sum [56], all other terms equal zero.

In the specific scenario of proton radiography the magnetic lens system projects an image of the object from the object plane to an image plane. This is also described as point-to-point focusing and ensures that every ray or proton coming from the object plane will be focused again – independent of its initial angle a_o – at a specific location after passing the system (in the image plane). As this object-image relation may contain a magnification $-m = (x|x) = R_{11}$, proton radiography is often referred to as *proton microscopy*, although the principle has nothing in common with the operating mode of a microscope.

The above described imaging condition reads $(x|a) = R_{12} = 0$, therefore using also the magnification $-m$ from above and the symmetry of the system leading to $R_{22} = 1/R_{11}$, Eqn. 2.19 can be rewritten to

$$\begin{pmatrix} x_i \\ a_i \end{pmatrix} = \begin{pmatrix} -m & 0 \\ R_{21} & -\frac{1}{m} \end{pmatrix} \cdot \begin{pmatrix} x_o \\ a_o \end{pmatrix}. \tag{2.22}$$

From this we can immediately extract the simple first order object-image correlation and add the valid second order terms so that the final proton position in the image plane reads

$$x_i = -m \cdot x_o + T_{116} x_o \delta + T_{126} a_o \delta. \tag{2.23}$$

Interpreting Eqn. 2.23 it becomes obvious that the $T_{116}x_o\delta$ has the biggest influence on the image quality as position dependent aberrations will lead to a distorted image. By making some assumptions it is possible to cancel this term completely using quadrupole magnets upstream of the object location. Suppose that the initial beam has a sufficiently small emittance and is strongly correlated in the phase plane so that $a_o = W_x \cdot x_o$ upstream of the object. Here $W_x = L_x^{-1}$ is the beam correlation coefficient. Due to scattering – mostly MCS – the protons exiting the object will show a deviation from the original a_o by an angle ϕ so that

$$a_o = W_x \cdot x_o + \phi. \tag{2.24}$$

Eqn. 2.23 can then be rewritten to

$$x_i = -m \cdot x_o + T_{116}x_o\delta + T_{126}(W_x \cdot x_o + \phi)\delta \tag{2.25}$$
$$= -m \cdot x_o + x_o\delta(T_{116} + W_x T_{126}) + T_{126}\phi\delta. \tag{2.26}$$

By preparing the incoming beam in a way that

$$0 = T_{116} + W_x T_{126} \tag{2.27}$$
$$W_x = -\frac{T_{116}}{T_{126}} \tag{2.28}$$

the $x_o\delta$ term – the position dependent chromatic aberration – vanishes leaving just the expression

$$x_i = -mx_o + T_{126}\phi\delta \tag{2.29}$$

for the proton position at the image plane. This method of cancelling aberrations is in general known as *chromatic matching* [57]. At the object location, x_o is only affected by $\frac{T_{126}\phi\delta}{m}$ where ϕ and δ cannot be influenced by the lens system itself. The term

$$C_x := \frac{T_{126}}{m} \tag{2.30}$$

is therefore a measure for the spatial resolution limit and called *chromatic length* of the setup.

Due to the *chromatic matching* another capability of the Russian quadruplet is revealed which is the angular sorting or the formation of a Fourier plane in the mid-plane of the setup. Referring to the above mentioned symmetry of the system the first order transfer matrix **R** can be divided into two transfer matrices **M** describing the first and second half of the setup so that

$$\mathbf{R} = \mathbf{M}^2 = -\mathbf{I}\det(\mathbf{M}) + \tau\mathbf{M}. \tag{2.31}$$

Here **I** is the identity matrix, $\det(\mathbf{M}) = 1$ the determinant of the beam line matrix and $\tau \equiv \mathrm{Tr}(\mathbf{M}) = M_{11} + M_{22}$ the trace of **M**. Then the position x_{fp} of a proton at the mid-plane of the setup using 2.24 is given by

$$x_{\mathrm{fp}} = M_{11}x_o + M_{12}a_o \tag{2.32}$$
$$= M_{11}x_o + M_{12}(W_x x_o + \phi) \tag{2.33}$$
$$= x_o(M_{11} + W_x M_{12}) + M_{12}\phi. \tag{2.34}$$

Rewriting the condition for *chromatic matching* from Eqn. 2.28 using Eqn. 2.31 we get

$$T_{116} + W_x T_{126} = \frac{\partial R_{11}}{\partial \delta} + W_x \frac{\partial R_{12}}{\partial \delta} = \frac{\partial \tau}{\partial \delta}(M_{11} + W_x M_{12}) = 0 \tag{2.35}$$

which shortens Eqn. 2.34 to just

$$x_{\text{fp}} = M_{12}\phi. \tag{2.36}$$

This is angular sorting. At this location the distance of every proton relative to the beam axis is just dependent on its scattering angle ϕ. By inserting a collimator at this location the proton distribution can be cut (e.g. removal of large scattering angles) for generating image contrast.

2.3.4 Interaction of protons with matter

Just as in case of X-rays described in Sec. 2.3, for proton radiography several interaction processes with matter have to be considered. Those mainly are *energy loss, nuclear interactions* and *multiple coulomb scattering* – summarized in Fig. 2.7.
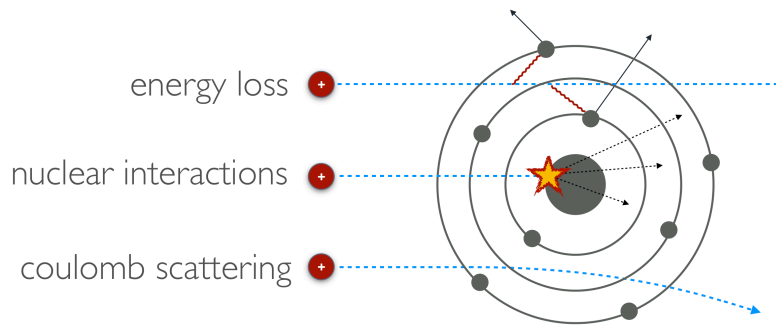
Figure 2.7.: Overview of the different interaction processes of charged particles – here protons – with matter.

Energy Loss
The energy loss of charged particles in matter has already been discussed in Sec. 2.2.3 and is described by the Bethe-Bloch formula Eqn. 2.10. It is dependent on the thickness, density and composition of the target. The interaction in the target with the electrons of the target atoms leads to a nonuniform energy distribution of the exiting beam. This affects the point-to-point focusing as the Lorentz force from Eqn. 2.17, responsible for the bending of the particle trajectories, is dependent on the particle velocity $\vec{v}$ which – in $\vec{z}$- or beam direction – is directly correlated to the particle energy. This causes dispersion in the magnets leading to a z-shift of the focal spot x_i in the image plane. An illustration of this effect is shown in Fig. 2.8. It is difficult to estimate the quantitative effect of the energy loss on the spatial resolution performance of a radiographic setup, mainly because of the unknown influence of the used collimator. Assuming that particles experiencing more energy loss also exit the target with a larger scattering angle due to more interactions, those particles will be the ones traveling further away from the beam

Figure 2.8.: Effect of chromatic aberrations of the imaging lens affecting the z-position of the focal spot.

axis at the location of the Fourier plane. The particles will be sorted out by the mid-plane collimator, therefore this effect can partly be canceled by choosing a different collimator. In (lig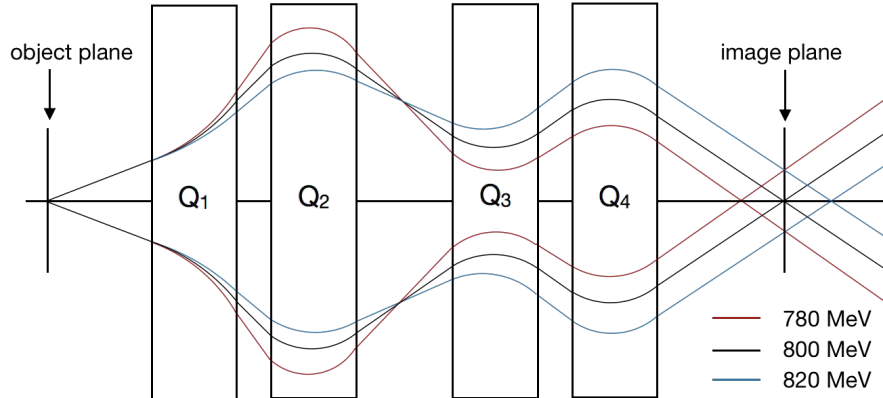ht) optics this is widely known as the limitation of the *depth of field* caused by the size of the aperture of the imaging setup. Investigations on the influence of the collimator have been conducted and are presented in Sec. 4.1.

Nuclear Interactions

In case of nuclear interactions we have to differentiate between elastic nuclear collisions and inelastic nuclear interactions. The elastic collisions – mostly relevant at lower particle energies – cause large scattering angles and possibly even a recoil of the proton. In this case, the interaction between the incident protons and the nuclei of the target happens through charge as described in the following section on MCS. If the velocity of the incident proton is large enough to overcome the electrostatic potential of the nucleus, a nuclear reaction will happen. In this reaction, which is considered as an inelastic interaction, the protons are first absorbed by the target nuclei forming new compound nuclei. Those nuclei are mostly unstable and break up into various fragments being ejected from the initial nucleus. The process is also called *spallation* and happens through strong interaction, it is dominant for the high energies used for proton radiography.

Although both types of interaction usually lead to a removal of the involved primary proton from the particle distribution, the total cross-section for the process and therefore the effect on the total particle distribution at the image plane of a radiographic setup is very small. By integrating the differential cross-section for nuclear collisions outside of the angular acceptance of the utilized radiographic setup the removal probability can be determined, however, this quantity is not measured continuously at the high energies required for proton radiography. Therefore, a simple approximation can be introduced. For sufficiently high beam energies above 1 GeV the probability for a scattering event is related to the nuclear collision length λ_{nc}

[58]. Using the exponential attenuation law known as Lambert-Beer law from Eqn. 2.1 the transmission can then be described by

$$T_{\text{nucl}} = e^{-x/\lambda_{\text{nc}}}. \tag{2.37}$$

The corresponding nuclear collision lengths are tabulated by the particle data group [59]. Due to the small cross section the influence of nuclear collisions on the total transmission is naturally very small but will increase for thick or dense targets. The actual contribution to the total transmission is plotted in Fig. 2.10(a), the dashed lines represent the contribution of the nuclear collision term to the total transmission in percent.

Multiple Coulomb Scattering

Coulomb scattering describes the deflection of charged particles in the electromagnetic potential of the nucleus of the target atoms. During the passage this process does not happen only once but several times, therefore it is also-called *Multiple Coulomb Scattering*. This may in certain cases affect the reconstruction of the initial scattering event and therefore affect the image quality (see Fig. 2.9). For thin objects MCS is the dominant interaction process as the cross section for nuclear collisions is considerably smaller. The theory of MCS was first investigated by
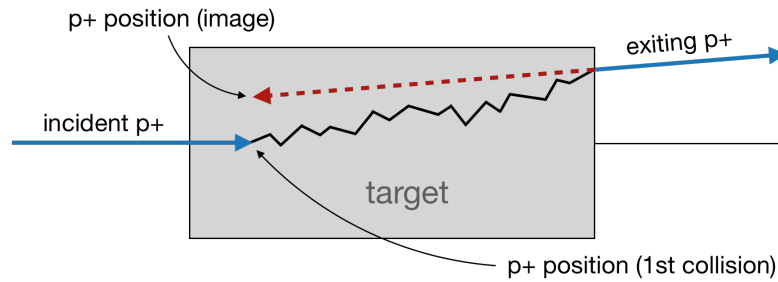
Figure 2.9.: Effect of MCS on the reconstruction of the initial position of the first scattering event.

Moliere [60, 61] and then summarized by Bethe shortly after [62]. The originally complicated theory by Moliere assumes zero energy loss in the target, however the full model by Bethe is capable of taking energy loss as well as compound target materials into account. Due to the complexity of the model and the requirement for the angular beam distribution to be known, which is inaccessible at the LANL and at other current radiographic setups, an empirical fit of the theory by Highland [63] (Eqn. 2.38) is used for the calculation and evaluation of the transmission. A detailed explanation of the Moliere theory itself would exceed the scope of this work.

Highland fitted the Bethe version of the Moliere theory without the Fano correction for low-Z materials and found a dependency on the radiation length λ_{rad} of the target, simplifying the calculation of the scattering angle to just

$$\theta = \frac{14.1 \text{ MeV}}{p\,v}\sqrt{\frac{x}{\lambda_{\text{rad}}}}\left[1 + \frac{1}{9}\log_{10}\left(\frac{x}{\lambda_{\text{rad}}}\right)\right] \tag{2.38}$$

with the particle energy $p\nu$ [63]. The accuracy of the Highland model as well as another approximation by Lynch and Dahl [64] has been investigated by Gottschalk [65] and compared to experiments with a 160 MeV proton beam. Whereas the original Moliere theory complemented with the Fano correction shows an accuracy of better than 1 % compared to the experimental data, the Highland approximation is slightly worse with on average 2.6±0.5 % deviation. The overall accuracy of the fit increases for higher energies as the energy dependence of the scattering correspondingly decreases. Note, that the approximation is only valid for $10^{-3} < x/\lambda_{\text{rad}} < 100$ [59].

2.3.5 Radiographic transmission

The transmission through a proton microscope is – as discussed in Sec. 2.3.4 – dependent on MCS and nuclear collisions as well as obviously on the acceptance of the chosen collimator. The transmission due to MCS can be described by Eqn. 2.39, the contribution from nuclear collisions has already been introduced in Eqn. 2.37.

$$T_{\text{MCS}} = 1 - e^{-0.5\frac{\theta_c^2}{\theta^2}} \tag{2.39}$$

Here, θ_c is the collimator acceptance and θ the scattering angle from the target which can be described by Eqn. 2.38. The total transmission formula then reads

$$T_{\text{tot}} = \exp\left(-\frac{x}{\lambda_{\text{nc}}}\right) \cdot \left(1 - \exp\left(-0.5\frac{\theta_c^2}{\theta^2}\right)\right). \tag{2.40}$$

In the specific case of a non-zero initial angular spread of the beam the initial angular straggling θ_0 has to be considered as well. This leads to Eqn. 2.41.

$$T_{\text{tot}} = \frac{\exp\left(-\frac{x}{\lambda_{\text{nc}}}\right) \cdot \left(1 - \exp\left(-0.5\frac{\theta_c^2}{\theta_0^2 + \theta^2}\right)\right)}{1 - \exp\left(-0.5\frac{\theta_c^2}{\theta^2}\right)} \quad \text{for } \theta_0 > 0 \tag{2.41}$$

An analysis of the transmission is shown in Fig. 2.10. First, the transmission for a fixed collimator ($\theta_c = 7.5$ mrad) dependent on the target thickness is plotted in 2.10(a) for several different target materials. As expected the transmission decreases with an increasing density. The dashed lines represent the contribution of nuclear interactions to the total transmission, as discussed in Sec. 2.3.4 it is more pronounced for heavier/high-Z materials and obviously also increases with an increasing target thickness. In 2.10(b) the dependence on the initial parasitic scattering angle θ_0 is plotted. In case of a small θ_0 only the high transmission part of the curve is affected, more precisely the 'dent' vanishes. For larger θ_0 also the rest of the curve at larger target thicknesses is affected.
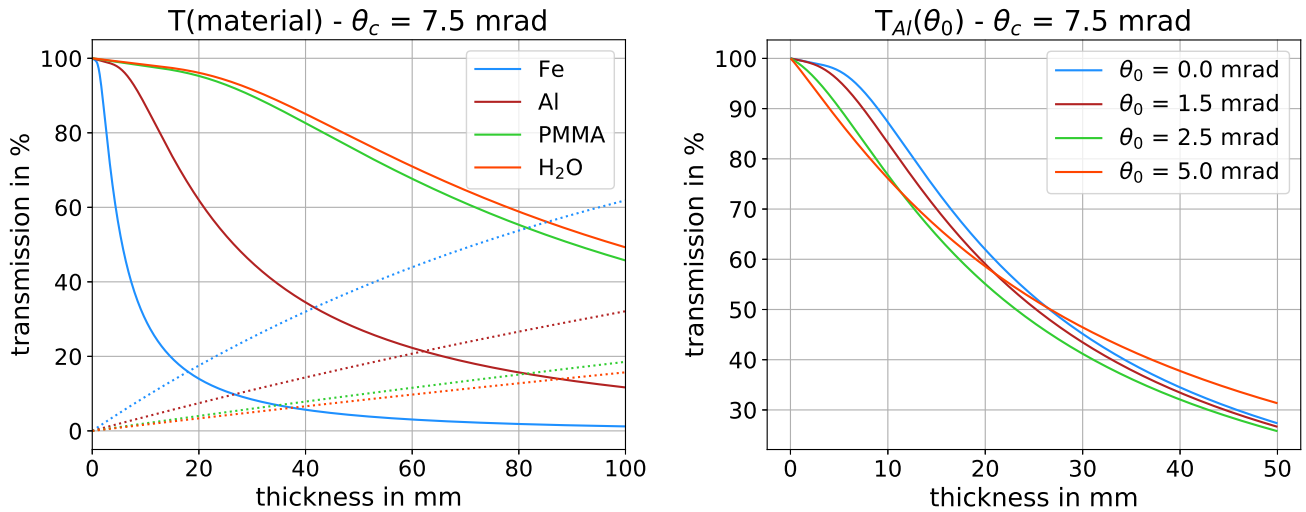
(a) Transmission through a proton microscope for different materials using a 7.5 mrad collimator.

(b) Transmission for different initial θ_0.

Figure 2.10.: Transmission formula plotted dependent on several parameters. On the left also the ratio of the nuclear transmission term contributing to the total transmission is plotted for each material as a dashed line.

In practice, the transmission image from proton radiography is obtained using three different types of pictures. Empty images, the so-called *dark field* images, are recorded in order to compensate for the background noise of the camera. Beam pictures without any object in place, so-called *white field* images, are captured as a measure of the shape of the beam profile and its intensity. In order to calculate the transmission, first the background must be subtracted from every *white field* and every actual radiography. The corrected target images are then divided by the corrected *white fields* resulting in a transmission image.

2.3.6 Image quality

The image quality of a radiographic setup depends mainly on the three factors chromatic aberrations, scattering and detector blur, all of which show an energy or momentum dependence.

Chromatic Aberrations

In Sec. 2.3.3 the influence caused by chromatic aberrations was introduced leading to the definition of the chromatic length (Eqn. 2.30). Considering the result from the imaging relations in Eqn. 2.29 we can conclude that the effect is dependent on the properties and geometry of the object of interest which directly affects the scattering ϕ and the energy loss straggling δ. This may lead to an effect known as *limning*, which is especially affecting steep density transitions. The larger the expected scattering angles, the more pronounced limning will be as depicted in Fig. 2.11. Therefore, the limning effect does also scale with the collimator size as in most cases $\theta_c \ll \phi$ [58].
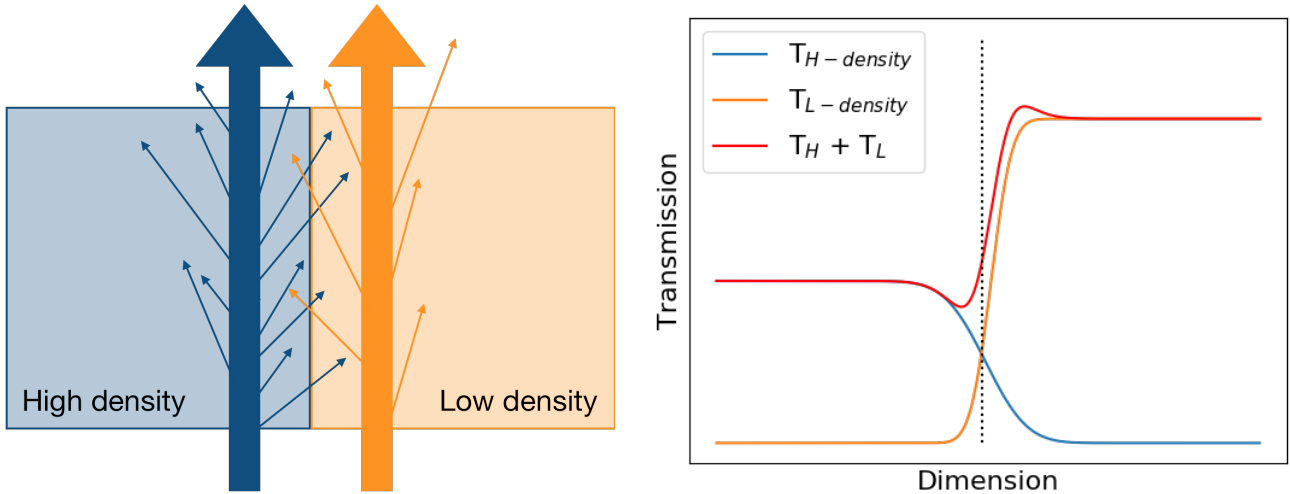
Figure 2.11.: Cause of the limning effect (left) and effect on the single and total (red) transmission profiles (right).

In addition to the limning, the terms ϕ and δ in Eqn. 2.30 show an energy dependence [58]. The matrix element T_{126} also has an inverse dependence on the proton energy [66]. Summing up the influence of all of those effects, we can conclude that the spatial resolution performance regarding chromatic aberrations has a $\propto p^{-3/2}$ dependence on the proton momentum p.

Scattering

Scattering in the object, especially MCS, results in a non-zero scattering angle of the exiting proton but may also cause a shift of the trajectory. It is in general described by Eqn. 2.38 and therefore proportional to the square root of the target thickness (neglecting the correction factor) but also $\propto 1/p$.

Detector Blur

Protons interacting in the used scintillation detector (see Fig. 2.6) mostly do not travel on a trajectory parallel to the beam axis but rather traverse the material with an angle determined by the focusing properties of the lens system. This leads to a non-parallel emission of photons by a single proton track which partly can be reduced by the choice of scintillators grown from columnar crystals capable of containing the produced photons in one column by total reflexion. The effect can also be decreased by the choice of thin scintillators which in turn decreases the total yield of light [58]. Detector blur is also boosted by secondary particles which are created during scattering processes of primary protons in the scintillation material. Summarizing the above findings, the detector blur is $\propto 1/p$ [67] and will decrease with increasing proton energy.

All of the effects above tend to scale inversely with the proton energy, suggesting that an increase of the particle energy will lead to an infinitely good spatial resolution performance. This is however not the case for several reasons. Choosing higher proton energies will decrease the amount of scattering and therefore require longer collimators with smaller angular acceptances

which are not only complicated to handle in terms of alignment but also deliver worse results. This is obvious as the collimator has to be long or dense enough to at least deflect unwanted parts of the angular proton distribution in a way that those protons don't contribute to the final image. However, in theory the Fourier plane is practically just a plane perpendicular to the z-axis with an infinitesimal dimension on that axis. Other investigations [68] showed that there is a minimum resolution limit for each setup even for zero energy spread of the beam.

2.4 Proton radiography with PRIOR-I at GSI

At GSI the PRIOR project – a German spin-off of the US pRad facility – was initiated in 2009. A compact magnifying lens system – PRIOR-I – based on high-gradient NdFeB permanent magnet quadrupoles (PMQ) was developed specifically for boosting the spatial resolution performance using protons up to 4.5 GeV from the SIS-18 ring accelerator. The custom magnets were developed and assembled at the ITEP and had an aperture size of 30 mm and a pole tip field of 1.8 T leading to a fixed field gradient of 120 T/m. In this configuration, with the lens system occupying just 1.4 m, the facility had a magnification factor of 3.5 and provided a spatial resolution of 30 μm at the HHT cave at GSI. Limited by the aperture of the PMQs, the maximum FOV of the setup was 9 x 12 mm^2.

Just as at the facilities at LANL and ITEP the PMQs are Halbach-type arrays – in case of GSI each array has a length of 36 mm and several of them can be combined to form a full PMQ lens. Each array is assembled from two layers of respectively 24 individual magnetic segments. The PRIOR-I lenses consist of 4 (outer lenses) respectively 8 (inner lenses) of those arrays and 6 equally sized dummy arrays made from plastic. Specialized aluminum casings allow the independent adjustment of each single array offering the alignment of the magnetic axes and the field mid-planes to the accuracy of ±20 μm and ±0.1 mrad.

During two separate beam times in 2014 the PRIOR-I setup was commissioned [37] and the performance was evaluated with several static and dynamic tests to approve the predictions on the spatial resolution performance and temporal capabilities. However, already after the first beam time a reduction of the beam energy from 4.5 GeV to just 3.6 GeV was mandatory to compensate for a reduced strength and quality of the magnetic field caused by radiation damage of the PMQs. Most of this damage occurred in the first and third lens, in the first one mainly due to scattering in the target and due to a misalignment of the beam during the first shots, in the third mainly due to scattering in the used collimator. Especially the scattering led to a huge amount of primary protons and secondary neutrons being deflected in the magnetic material and degrading the overall field quality by boosting the presence of higher parasitic multipole components.

Antecedent investigations predicted this effect [69] which was also noticed at LANL [70] but due to insufficient models and a lack of data in the energy range of several GeV a quantification was impossible. Therefore, following the commissioning of PRIOR-I, ongoing investigations on the occurred radiation damage were performed. For this estimation of the expected radiation damage, a spare Halbach array assembled as described earlier as well as single NdFeB wedges with a different orientation of the magnetization were deliberately irradiated with 3.6 GeV pro-

tons. The array was placed in front of the entrance to the beam dump and furthermore aligned in a way that the proton beam hit the upper left corner of the module to achieve a non-uniform dose delivery. In collaboration with scientists from the Material Science Department of the TUD the radiation damage was evaluated and found to be dependent on the dose as well as on the demagnetizing field inside the magnetic material which in turn depends on the geometry and magnetic direction of the wedges [71]. However, the collected data and applied methods were insufficient for developing a quantitative description. The full interaction process of high energetic charged particles with permanent magnet material is up to now not completely understood on a microscopic scale but a recent topic of research [72].

The investigation led to the conclusion that a continuous operation of the PRIOR-I setup at GSI and later at FAIR would require a continuous remagnetization of the lenses after each beam time. Thus, PMQ lenses were considered to be unsuitable for operation with high energetic particles and a new facility based on electromagnetic quadrupoles (PRIOR-II, see Sec. 2.5) was developed for continuous operations.

2.5 PRIOR-II at GSI/FAIR

Following the demagnetization of the PRIOR-I prototype lenses during the commissioning, a new lens system with four strong electromagnetic quadrupole lenses was developed at GSI [68]. Replacing the PMQs proved to be a challenging task since the spatial resolution performance of the setup scales with the total length of the lenses requiring the highest possible field gradients. The PRIOR-II quadrupoles have an aperture of 60 mm with a maximum pole tip field of 1.3 T resulting in a maximum field gradient of 43.3 T/m which is just about a third of the maximum gradient of the PRIOR-I lenses. Here a trade-in was made which leads to a larger FOV of the new PRIOR-II setup but still requires longer lenses (40 cm for the outer two and 65 cm for the inner two lenses).

The PRIOR-II setup was developed for two different scenarios, first of which is the FAIR phase 0 which includes an operation at the present HHT cave of the GSI facility. With a reference energy of 4 GeV protons a magnification of 3.49 can be reached, the theoretical spatial resolution limit is around 10 μm. The beam line at HHT allows beam transport down to around 1 GeV which is mostly interesting for biomedical imaging purposes. Nevertheless, the maximum FOV of around 30×54 mm^2 will be just sufficient for a proof of concept or small animal imaging.

The setup will then be moved to the HEDgeHOB beam line at the new FAIR facility. Due to the increased drift distance between the system and the detector setup the magnification increases to 8.03, furthermore the increased reference energy of now 5 GeV causes a slightly increased spatial resolution performance just below 10 μm. The ion optical scheme of the beam line and the setup is shown in Fig. 2.12. The FAIR facility will boost the performance of the technique not only in terms of spatial resolution performance but also in terms of statistics and temporal resolution. This is of a huge interest especially for the dynamic high energy/density experiments which require a sufficient proton statistics for the short timescales of the experiment. For biomedical imaging mainly the short imaging time is beneficial as too many protons
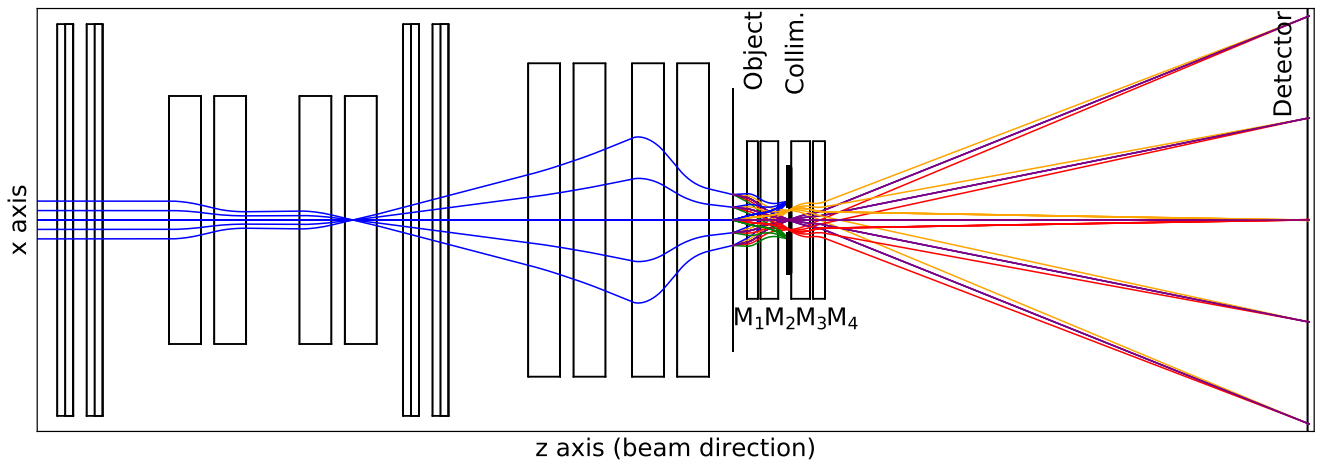
Figure 2.12.: COSY INFINITY ray simulation of the PRIOR-II facility at the HEDgeHOB beam line at FAIR (x-axis only).
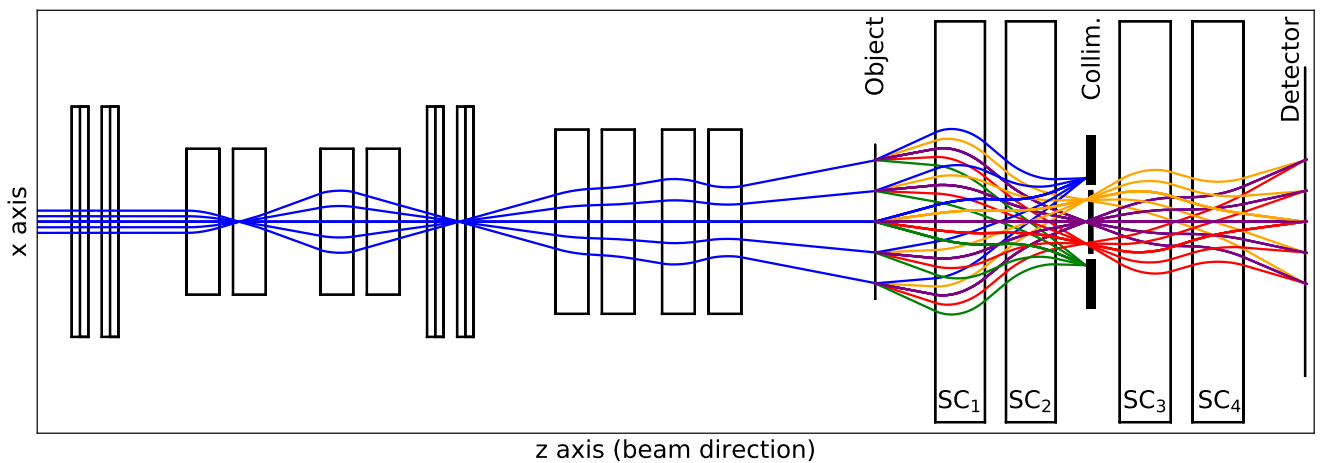
Figure 2.13.: COSY INFINITY ray simulation of the superconducting identity lens at the HEDge-HOB beam line at FAIR (x-axis only).

per spill do increase the density reconstruction accuracy but simultaneously also increase the dose deposition in the target volume.

At the HEDgeHOB beam line another possibility for proton radiography exists employing the high gradient focusing system of the plasma physics group. This quadruplet can be used as an identity lens and offers – with an aperture diameter of 200 mm – a significantly larger FOV. However, as this setup consists of superconducting magnets, the minimum beam energy for a stable operation is above 1 GeV complicating the use of this setup for biomedical applications. The ion optical scheme of this beam line is plotted in Fig. 2.13.

3 Materials and experimental Methods

All of the experiments on PaNTERA conducted during the time frame of this work took place either at the LANSCE linac of the LANL facility or at the university clinic in Heidelberg. This required not only a detailed knowledge of the capabilities of those external facilities but also the development of new software suited for handling the taken data. In this chapter an overview over the accelerator facilities as well as a general description of the used targets and the designed software is given.

3.1 The LANSCE linac

The heart of the LANSCE facility at the LANL is the 800 MeV proton linac. The injector section consists of two ion sources – one for H^-, one for H^+ – as well as two 750 keV Cockroft-Walton generators. The linac itself has two acceleration stages out of which the first one is a 201.25 MHz drift-tube linac for increasing the ions' energy to about 100 MeV. Afterwards the ions are either transferred to the rare isotope production site or to a side coupled cavity linac capable of increasing the energy to about 800 MeV. The ions can then be used for the production of neutrons used for experiments either at the Lujan Center or at the Weapons Neutron Research operations area. Those facilities can also make use of the proton storage ring (PSR). Furthermore, the beam can be transferred to the Areas A, B and C for experiments on ultra cold neutrons or for proton radiography. A scheme of the whole accelerator is presented in Fig. 3.1.
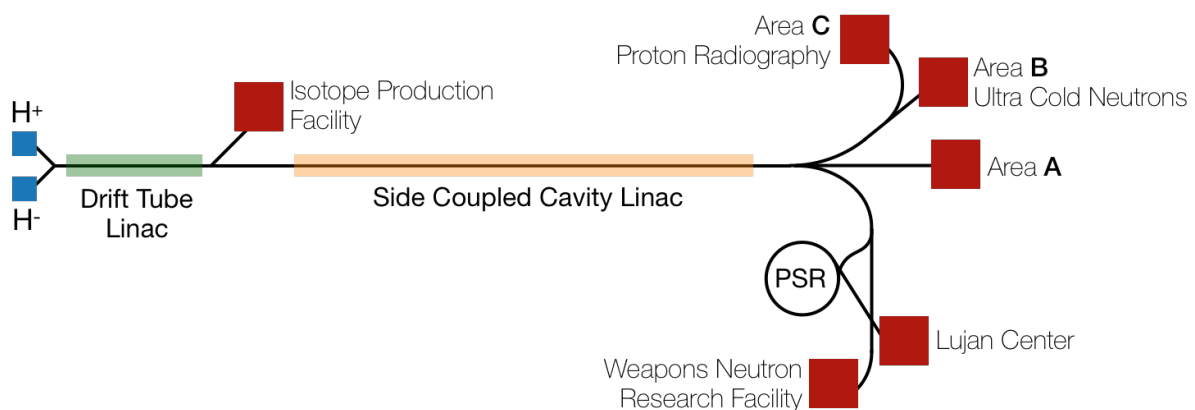

Figure 3.1.: Schematic of the LANSCE accelerator facility.

3.1.1 LANSCE spill structure

At the proton radiography facility a spill structure with a pulse width of 50 ns is used in most of the cases – mainly determined by the requirements of the performed dynamic experiments

[73]. Every pulse does in turn consist of a minimum of 7 bursts, each containing about $5 \cdot 10^8$ protons and a typical burst length of 200 ps which can be decreased to about 100 ps if required – correspondingly decreasing the number of particles to about $3 \cdot 10^8$ per burst. The minimum separation length between the single bursts is 5 ns determined by the 201 MHz radio frequency of the drift tube linac. Depending on the scenario the spacing between single pulses can be adjusted by modulo 358 ns, whereas this minimum spacing is determined by the accelerator pulse programmer (see Fig. 3.2) [32].
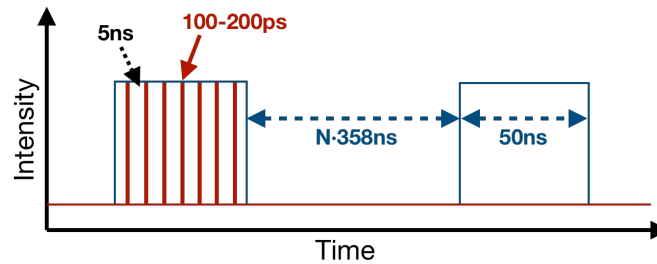

Figure 3.2.: Spill structure of the LANSCE linac used for proton radiography.

The extracted beam is described by a pattern number reading e.g. *lin80*. This for example describes a short pattern with 12 100 ps bursts and 3 60 ns pulses in total per image with a 1 μs spacing resulting in roughly $1.08 \cdot 10^{10} - 1.92 \cdot 10^{10}$ particles per shot (3 pulses equal 3 images). There's an uncertainty of a factor of about 2 included as the first and last bursts (about 10 ns of the pulse) have very few protons due to the finite time period from beam request (chopper activation) to actually receiving beam. The quantitative influence of this effect is unknown and up to date not measured, for the dosimetry we have therefore assumed the maximum flux of $1.92 \cdot 10^{10}$ protons.

3.1.2 The LANSCE proton radiography facility

The LANSCE proton radiography facility is situated in the dome of area C (see Fig. 3.1) receiving only negative hydrogen ions (H^-) from the linac. The accessible beam line consists of a diffuser station at the beam entrance location, three matching quadrupoles and three large aperture identity lenses with two target (OL - object location) and two image locations (IL) visualized in Fig. 3.3. The first two quadrupoles of the second identity lens downstream of the second target location are mounted on rails and can be removed for placing the available x3 and x7 magnifiers.

For most of the experiments a tungsten diffuser with a thickness of 50 mil (~ 1.27 mm) is used. The diffuser does increase the angular width σ_0 of the incoming proton beam by 6.76 mrad[1] which is mandatory for establishing the matching conditions and simultaneously filling the whole acceptance of the radiographic setups. For the x7 setup less broadening is required to fill the acceptance, therefore here only a 10 mil ($\sim 250 \, \mu$m) diffuser is used.

The first object location OL_0 following the matching section is foreseen for the placement of fiducials for measuring the image distortions. There are three different fiducials available, one

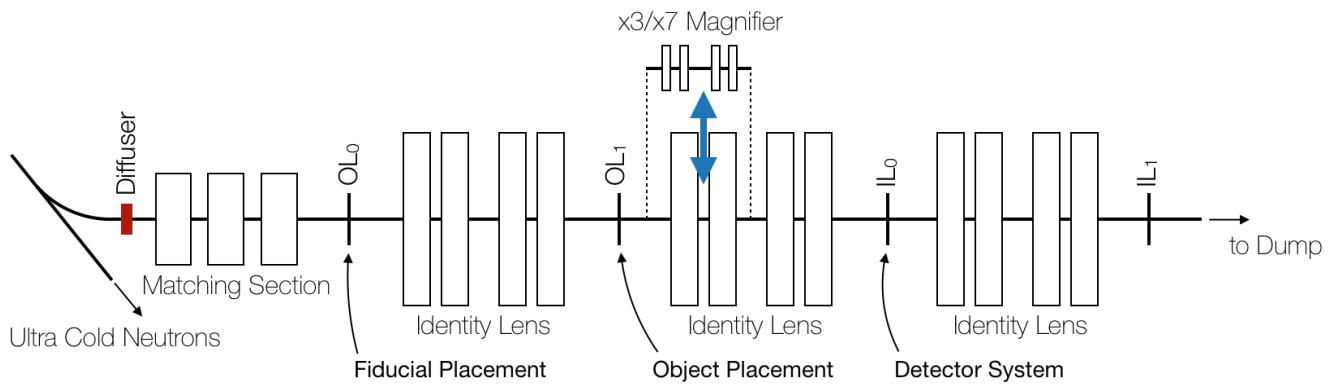---

[1]   Calculated with GSI ATIMA.

Figure 3.3.: The LANSCE pRAD facility.

for each of the radiographic setups (x1, x3, x7). Those targets can automatically be placed in the beam using a simple target wheel. The second target location OL_1 is foreseen for experiments and allows for the mounting of a medium sized cylindrical vessel for powder gun experiments or a large spherical vessel for experiments with high explosives. The target chambers can also be left out using windows on the ends of the beam pipes upstream and downstream of the target location. This enables the placement of static targets such as e.g. wedges on a linear actuator (LANL goniometer) in air.

The specifications of all of the available setups at LANL are listed in Tab. 3.1. Whereas the x1 identity lens and the x3em magnifier are based on normal conducting electromagnets, the x7 setup remains to be made from PMQs in a Halbach-style orientation. This is necessary to reach the high integrated field gradients of up to 5.64 T which would not be possible with conventional electromagnets. Although it is known that – assuming an equal pole tip field in all of the lenses – the optimum ratio between the inner and outer quads is 1.71 [68], in case of the x7 the inner two lenses are twice the length of the outer two.

Facility	Magnification	FOV	Aperture
x1	1.000	120 x 120 mm^2	304.8 mm
x3em	2.775	12.83 x 9.42 mm^2	390 mm
x7	7.010	15.1 x 15.1 mm	25.4 mm

Table 3.1.: Specifications of the available pRad systems [74].

Furthermore, a set of collimators with different acceptances from 2.5 mrad up to 10.0 mrad has been used in the course of the experiment campain. As the technical details are fully known of only the electromagnetic x3em setup, we can only consider the collimators used for this setup. The full specifications of the cutout as well as an overview of the 2σ beam sizes at the Fourier plane calculated by COSY INFINITY are summarized in Tab. 3.2[2]. Those tungsten collimators are placed at the location of the Fourier plane and have a length of 50.8 mm. There are two different sets of collimators available depending on the experiment conditions, either variable

---

[2]   Internal communication with F.E. Mariam, LANL.

collimators which can be changed easily through a sealed opening in the beam pipe or fixed collimators welded to the beam pipe in a way that the whole vacuum section has to be replaced for a collimator change. The latter ones are foreseen for experiments with high explosives to prevent a mechanical shift of the collimator caused by the detonation. Part of those collimators are damaged by fragments ejected from previous explosions unpredictably affecting their actual angular acceptance.

Collimator	Beam Envelope at FP (COSY)	Collimator size
2.5 mrad	6.41 x 4.84 mm^2	6.25 x 4.50 mm^2
5.0 mrad	12.81 x 9.67 mm^2	12.83 x 9.42 mm^2
7.5 mrad	19.52 x 14.54 mm^2	19.42 x 14.3 mm^2
10.0 mrad	25.61 x 19.37 mm^2	26.00 x 19.25 mm^2

Table 3.2.: Specifications of the pRad x3em collimators.

3.1.3 Proton radiography detector systems

For proton radiography two different detector systems using three different cameras are available suiting the different needs of the experimental community.

The dynamic detector system consists of 7 Rockwell/Teledyne cameras focused on a 2 mm Lutetium Oxyorthosilicate (LSO) scintillator using a mirror system (see Tab. 3.3 for full specifications, see Fig. 2.6 for geometric arrangement). The cameras are equipped with a 105 mm Nikon F2.0 lens and offer a dynamic range of 11 bit. As the decay time of the used LSO is roughly 50 ns all bursts in one pulse (see Sec. 3.1.1) are integrated in one image. The minimum inter frame time between two images is 250 ns which does not limit the effective inter frame time given by the accelerator's capabilities [75]. The effective pixel size at the image plane is just 166.7 μm which is less than the theoretical limit of the radiographic setup itself. For static imaging all 7 cameras fire at the same time resulting in 7 identical images per pulse and 21 images per shot in case of a *lin* beam pattern. The effective resolution of the image is reduced to just 600x600 px as part of the frame holding the scintillator crystals in place is also imaged.

For static imaging a pco.dimax camera as well as a 2-Tile Lutetium Yttrium Orthosilicate (LYSO) scintillator is available. The camera offers high resolution images with an effective pixel size of 60 μm matching the x3 setups spatial resolution performance. The used camera was equipped with correlated double sampling (CDS), which is an automated dark field subtraction mechanism. Here the camera averages pixel values between image capture and subtracts the average value from the captured image. Investigations showed, that the accuracy and outcome of the algorithm strictly depends on the spacing between image captures resulting in a nonuniform result. The effects of CDS as well as issues with the pco.dimax firmware are discussed further in Sec. 4.8.2.

With a CsI scintillator also a Dantec Dynamics HiSense 620 camera is available for static imaging. The camera offers a sensor resolution of 4 MPx with a pixel size of just 7.4 μm and

Setup	Rockwell	pco	Dantec
Scintillator	6-Tile LSO	2-Tile LYSO	2-Tile CsI
Decay Time	30 ns	45 ns	$1\,\mu s$
Detector Size		$12x12\,\text{cm}^2$	
Camera	7 Rockwell	pco.dimax PRO	Dantec HiSense 620
Resolution	$720x726\,\text{px}^2$	$2000x2000\,\text{px}^2$	$2048x2048\,\text{px}$

Table 3.3.: Specifications of the available pRad detector systems.

14 Bit depth. During the experimental campaign it was only used for imaging with the x7 magnifier, the used lens produced a Newton's ring pattern discussed in Sec. 4.8.3.

3.2 X-ray measurements

The X-ray CT data was captured at the university clinic in Heidelberg with a Siemens Biograph 40, a Siemens Sensation Open and a Siemens SOMATOM Confidence. The latter two are used for the calculation of treatment plans for heavy ion therapy, the Biograph 40 is just used for experimental purposes. The full capabilities of the machines are listed in table 3.4.

	Biograph 40	Sensation Open	SOMATOM Confidence
Collimator	40×0.6	64×0.6	40×0.6 or 24×1.2
Tube Voltage		80 - 140 kV	
Tube Current		300 - 400 mA	
Pitch	0.3 - 0.35 mm	0.35 mm	0.45 mm
Slice	0.4 - 3.0 mm	0.5 - 3.0 mm	0.6 - 3.0 mm

Table 3.4.: Specifications of the used X-ray machines at the Universitätsklinikum Heidelberg.

In addition to the different machine settings several different tomographic kernels are available from Siemens. Depending on the choice of the kernel several image features can be enhanced or suppressed. The kernel is described by a four-cipher string where the first letter describes the general use ("H" - Head, "B" - Body, "D" - DECT specific kernel, "U" - Ultra high resolution). The following two-digit number is an indicator for the sharpness and simultaneously noise level of the CT images – with an increasing number the sharpness will increase but simultaneously significantly boost the noise of the images. Multiples of 10 are considered as the "conventional" kernels, numbers in-between introduce special features such as "X1" - higher grain noise, "X2" - without beam hardening correction, "X5" - edge preserving noise reduction where X is any number between 1 and 9. The last cipher indicates whether the image is "s" - smoothed or "h" - hardened.

3.3 Simulation software for proton radiography

In order to predict the requirements for the potential biomedical targets simulation software is essential. The pRAD setup at LANL was modeled with the COSY INFINITY beam simulation described in Sec. 3.3.1, with the help of an in-house Monte Carlo (MC) code (Sec. 3.3.2) a pre-assessment of the transmission and expected image quality was performed.

3.3.1 COSY INFINITY beam simulation

COSY INFINITY is a simulation software package for arbitrary order beam dynamics simulations developed and distributed by the Michigan State University, USA [76]. Due to the arbitrary order design the code facilitates to calculate the higher order transfer matrices of the ion optical system which are important for MC simulations (Sec. 3.3.2). Furthermore, the high order beam moments allow for an estimation of the spatial resolution performance. The code is also used for driving the actual experiments. Implementing the matching and imaging conditions it can provide the mandatory settings for the magnets of the upstream matching section as well as for the magnets of the proton microscope.

3.3.2 PROSIT MC simulation

PROSIT is a lightweight Monte Carlo code developed by Dmitry Varentsov at GSI [77] for simulating proton radiography. Compared to a full MC code it does only consider the part of the interaction processes affecting the beam physics, therefore the output just consists of an array of particle vectors containing the position, momentum and remaining energy of the different particles. Any interaction affecting the target, e.g. energy deposition, is not monitored. The software can consider beam interactions in ion optical elements such as magnets, which can be implemented using beam transport maps of arbitrary order calculated by COSY INFINITY (see Sec. 3.3.1), or the interaction with various types of matter. The latter one, the interaction with matter, is based on the idea that the angular straggling and energy loss straggling distributions of an arbitrary beam exiting an object are Gaussian shaped. Splitting the target geometry into thin slabs such a Gaussian "*kick*" can be added to the individual particle trajectories after passing a single slice. The thinner the slices, the more accurate the result which then resembles the output of a classical MC, which handles every particle individually in terms of mean free path and interaction processes. As a result, the PROSIT code offers a much better performance compared e.g. to a conventional GEANT4[3] simulation.

Depending on the available resources the PROSIT code has been used on either the plasma physics internal servers with up to 72 cores or on the Kronos cluster of GSI providing up to 16544 cores.

---

[3]   Geometry and Tracking 4, simulation toolkit from CERN, http://cern.ch/geant4/

3.4 Targets for proton radiography

In order to evaluate the postulated suitability of high energy proton radiography for medical applications a set of different targets has been developed. Wedge targets focus on the influence of image artifacts regarding the general density reconstruction properties. The head phantom has been designed similar to conventional clinical phantoms and is suitable for testing the possibility of cancer treatment planning using proton images. Furthermore, the dosimetry cap introduced in Sec 3.5 allows for a comparison between the dose deposition of a conventional xCT and a proton image.

3.4.1 pRad wedge targets

In order to evaluate the general suitability of proton radiography for medical applications two simple types of wedge targets have been manufactured. The outstanding spatial resolution capabilities of proton radiography have been demonstrated before [3, 37], therefore, the targets focus on the performance regarding the depth of field and the proton flux dependent density resolution. Both quantities are of great relevance due to the fact that due to the geometry of human patients the protons will experience a significant energy loss which is affecting the image quality of proton radiographic images. Furthermore, current imaging techniques are already optimized for reducing the dose to the patient which is more of a challenge in case of high energy protons.
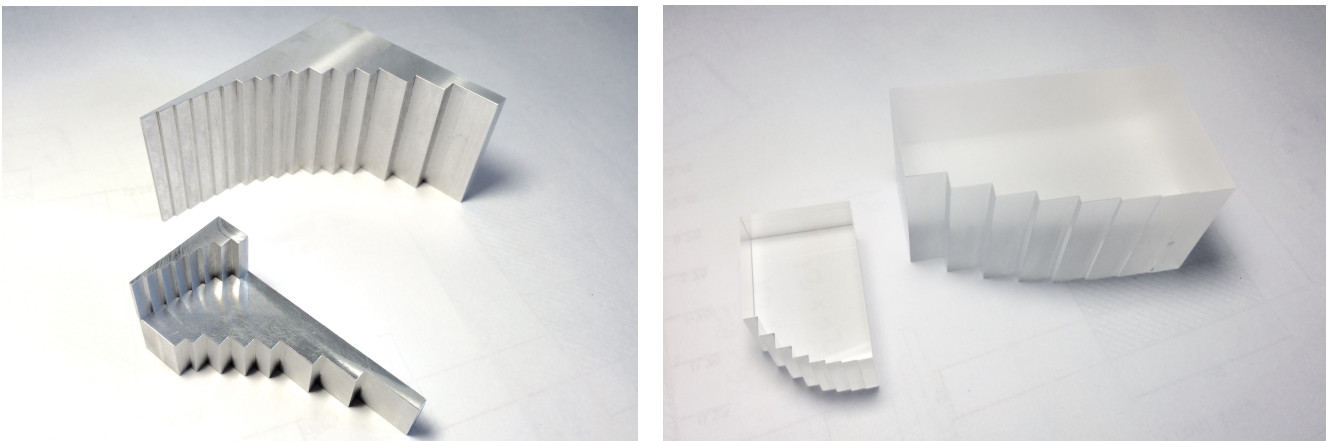
Figure 3.4.: Images of the x1 and x3em Al wedge targets (left) and PMMA wedge targets (right).

The aluminum wedge target is designed in a way so that its transmission range is between 10 and 90 % when using a 5.0 mrad collimator. For the target design the thickness of the steps has been pre-calculated using the Highland transmission formula (see Sec. 2.3.5) and afterwards simulated using the *transmit.py* tool of the plasma physics group (see Sec. 3.3.2). The target has been manufactured at the GSI workshop for the x1 setup as well as a shrinked version for the x3em magnifier consisting of two parts is available (see Fig. 3.4 (left)). The transmission profile of the *transmit.py* simulation is shown in Fig. 3.5(a). Aluminum is an obvious choice for

this type of target especially as its (atomic) properties (Z_{Al}=13 - $\rho \approx 2.7\,\text{g/cm}^3$) allow the easy manufacturing of a reasonably compact target and furthermore it resembles to some extent the characteristics of human bones ($\rho \approx 1.9\,\text{g/cm}^3$ - $Z_{\text{eff.}}$(bone)=9.14 [78–80]).
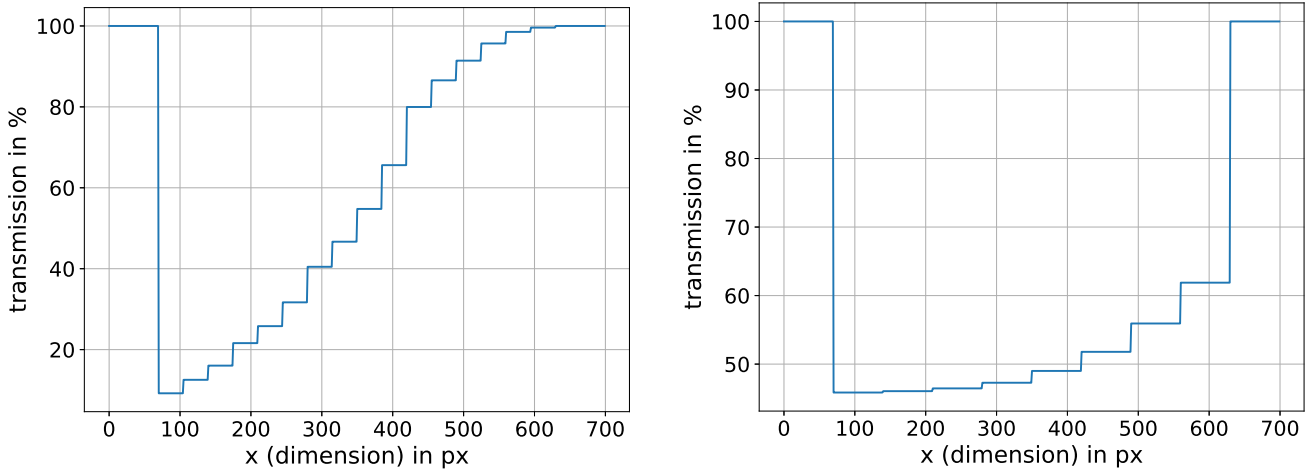
(a) Transmission profile of the x1 version of the aluminum wedge target imaged with a 5.0 mrad collimator.

(b) Transmission profile of the x1 version of the PMMA wedge target with a 5.0 mrad collimator.

Figure 3.5.: Transmission profiles of the wedge targets calculated using the *transmit.py* code.

Similar to the aluminum target a density resolution target made from polymethylmethacry-lat (PMMA) has been designed and manufactured. This target has decreasing differences in density from $0.585\,\text{g/cm}^2$ between the largest steps to just $0.029\,\text{g/cm}^2$ between the smallest steps. Using a 5.0 mrad collimator this difference corresponds to just 0.23 % transmission, with a 7.5 mrad collimator as in the actual experiments this is reduced to just 0.19 %.

3.4.2 The GSI pRad head phantom

For addressing the advantages of proton radiography in heavy ion tumor therapy a head phantom similar to those used in clinics for the calibration of X-ray machines has been developed and manufactured. The cylindric PMMA phantom has a diameter of 60 mm to match the limited FOV and can take up to 3 cylindric insets made from different materials. The diameter of those insets is 15 mm, they're distributed equally with a 120° spacing on a 20 mm radius in the target. This has the advantage that for three different rotation angles per half rotation of the target the insets don't overlap in a side projection. For the determination of the current rotation position a 2 mm drill-hole for an orientation rod is foreseen centered on a 25 mm radius between two of the holders for the insets. For proton radiography an orientation rod made from stainless steel or aluminum can be inserted, for X-ray measurements the drill-hole is left empty to suppress image artifacts usually caused by high-Z materials. A picture of the target is shown in Fig. 3.6.

The size of the phantom is chosen in a way that it fits inside the FOV of the LANL x1 setup (see Sec. 3.1.2) and can be used also with the x3 setup when capturing two side by side projections

which can be stitched together. For use with the x7 magnifier, a smaller version, which is an exact copy of the original one but shrinked by a factor of 6, has been manufactured.

material	density (g/cm^3)	stopping power (MeV·cm^2/g)	electron density $\times 10^{-11}$ (cm^{-3})
PVDF	1.76	2.065[4]	-
POM	1.42	2.232[4]	4.53
PMMA	1.19	2.269[5]	3.87
PE	0.89	2.457[6]	-
TE 0.00	1.083 ± 0.005	-	3.5609
TE 0.34	1.079 ± 0.005	-	3.5493
TE 2.07	1.062 ± 0.005	-	3.4935
TE 3.46	1.048 ± 0.005	-	3.4486
TE 5.25	1.030 ± 0.005	-	3.3902
TE 7.56	1.007 ± 0.005	-	3.3153
Water	1.000	2.333	3.34

Table 3.5.: Specifications of the materials used for the head phantom with decreasing density. For comparison the properties of water are also listed. The stopping powers of PE, PMMA, POM and PVDF have been calculated using several tools.

The material properties of the used insets are summarized in Tab. 3.5. The tissue equivalent (TE) insets were ordered from the external manufacturer QRM, the technical properties of the insets such as density and electron density were obtained from a data sheet. However, after 2 years exposed to air the diameter of the rod insets did decrease from 14.95 mm to just around 14.7 mm. All TE rods – the ones with air bubbles inside and the pure base material – were affected. Although at the same time the weight of the material did decrease leaving the density of the material almost unchanged, the occurrence prevented any further experiments using those materials. An extended discussion of the observed effects can be found in Sec. 4.8.4. The smaller x7 phantom is only available with the high density plastics shown in Tab. 3.5 as for handling reasons the different material rods had to be grouted in the PMMA base structure.

3.5 Dosimetric measurements

For dosimetric measurements thermoluminescence dosimeters (TLDs) were used as they allow measuring low and high doses from the mGy range up to several Gy. The TLD-700 chips type SNO78835 from ThermoFischer Scientific have dimensions of 3.2x3.2x0.89 mm^3 and are rated for recording doses as low as 10 pGy up to 10 Gy. The base material is lithium fluoride (LiF:Mg, Ti). The TLDs were provided and read out by the Deutsches Zentrum für Luft und Raumfahrt (DLR) in Cologne.

---

[4]   NIST PSTAR (`https://physics.nist.gov/PhysRefData/Star/Text/PSTAR.html`)
[5]   ICRU49+73 database (`http://dedx.au.dk`)
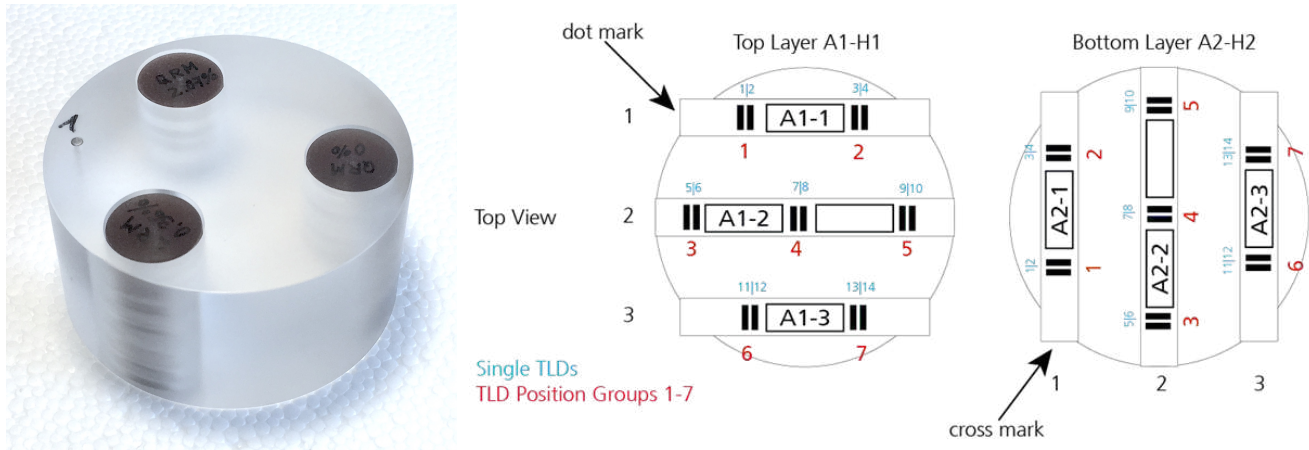[6]   BETHE_EXToo (`http://github.com/APTG/libdedx`)

Figure 3.6.: The GSI head phantom (left) and placement and orientation of the TLD crystals in the corresponding dosimetry cap (right).

The imaged phantoms can be equipped with a dosimetry cap holding 6 soft plastic tubes arranged perpendicular on two layers (see Fig. 3.6). Each layer has 7 measuring spots with 2 TLDs at each position for redundancy resulting in a total of 28 TLDs per measurement. In total 9 sets with 28 TLDs in each set were used, 6 for radiographic imaging with protons at the LANL and 3 for X-ray CT at the HIT. Another set of 8 single TLD chips was always transported with the 9 sets in order to compensate for any additional or background radiation coming from either the much higher radiation background in the volcanic region around Los Alamos or from X-ray scans of the package when shipping the detectors from and to the LANL.

3.6 Data processing

For processing purposes a set of software has been developed using the language *Python* to accommodate the requirements of experimental data. The choice of the programming language is obvious as it can be executed on both, Windows and Unix machines without changes to the code and allows embedding external code (e.g. *C*) for speeding up the calculations. A full overview over the developed tools is given in A.1.

3.6.1 Data flattening

For the calculation of the proton transmission separate beam pictures, also referred to as *white field images*, as well as several non-illuminated pictures (*dark field images*) have been captured. As the beam profile is not stable and does vary between several spills (see discussion in Sec. 4.8.1), the selection of suitable white fields is non-trivial in an experiment scenario compared to simulated data. The tool *quickpr.py* has been specifically designed for handling the LANL experimental data and facilitates the averaging of target pictures as well as the selection of suitable white fields by plotting the resulting central profiles in x- and y-direction of a target image - white field division. When the resulting profile is flat at non-target regions after the

division, the particular white field can be selected with a check box and then used for the calculation of the transmission. Also, several white fields can be combined and averaged to a new, virtual white field to achieve a better flattening result. The selected number of target images is then processed and divided by the clean white fields before an averaged dark field captured during the same run is subtracted. In case of the pco.dimax data no dark field is subtracted due to the activated CDS mode (see discussion in Sec. 4.8.2).

For further flattening the *flattengui.py* tool has been developed to take into account any offset coming from the camera setup or any further deviation caused by the original flattening procedure. The tool itself has a graphical interface based on the *Tkinter* plug-in for *Python* and allows the handling of arbitrary experimental data in the *.tif* format. Based on the assumption that the first flattening approach may lead to a linear offset of the transmission caused by a different intensity in the original images the tool allows further flattening using a fitted correction plane. For this it is possible to select the non-target regions of the image which should be completely flat and to fit a two dimensional plane to those. The plane itself is described by a two dimensional polynomial up to 3rd order, however, for processing the experimental data only first order polynomials have been used as the predicted simple intensity shift does not justify a higher order fit.

3.6.2 Recalibration of single radiographic images
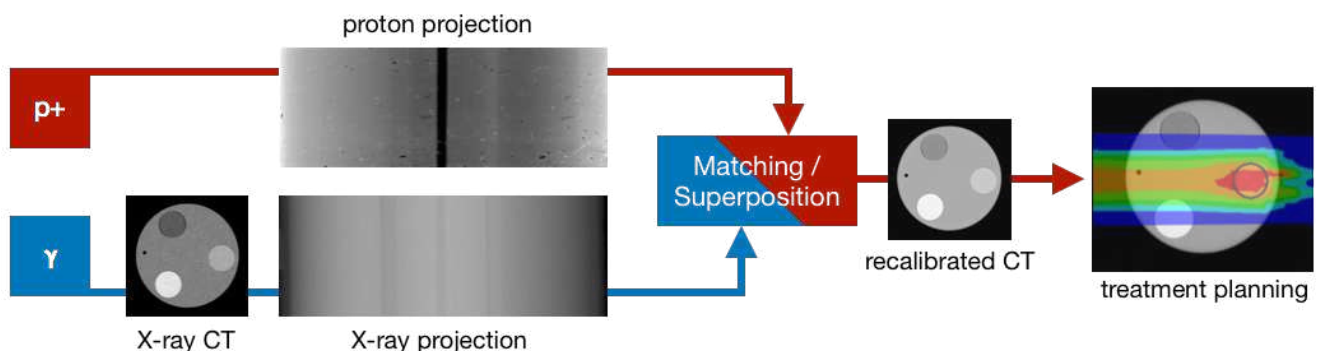
Figure 3.7.: Schematic representation of the recalibration process.

The recalibration of tomographic images is based on the concept that X-ray CT is capable of providing a sufficiently detailed map of the volume of interest inside a patient whereas high energy protons can deliver a much more accurate density analysis. As it is technologically challenging to rotate heavy ion beams – especially high energy beams in the GeV range – around the patient, it is significantly easier to use suitable base data, e.g. X-ray or MRT, instead which is then recalibrated completely avoiding the issues of the current HLUT procedure. The idea of the recalibration is to capture a single proton image which is then matched with a single corresponding X-ray projection. Once a match is found in the stack of X-ray images a new calibration curve is assembled which can then be used to first recalibrate the whole stack of X-ray projections, then a recalibrated CT can be calculated.

Feature detection

For overlapping proton and X-ray projections a feature detection algorithm was developed which recognizes certain image features mandatory for correcting any distortions affecting the procedure. Two separate tools, *pdetect.py* for proton data and *xdetect.py* for photon data, were developed. Both tools use the same algorithm which calculates the second derivative of a specified horizontal selection of the target image. In order to take into account any noise caused by the detector systems, a 1d Gaussian filter with a radius of $\sigma = 3$ px is applied afterwards to this selection. The second derivative, the turning points of the profile, allows for an accurate identification of features as any step in the profile with a small change of the inclination without a change of the sign, caused e.g. by the sides of one of the insets, will be translated into a steep offset in the first derivative. This offset is then translated into a minimum when calculating the second derivative.

Introducing a threshold for counting the calculated minimums, which is automatically adjusted by the number of detected features, we can therefore easily detect the borders of the insets as well as the location of the orientation rod. An exemplary output of the software is shown in Fig. 3.8 including the previously discussed threshold. The position of the orientation rod is then compared at the top and at the bottom of a target image to identify any possible rotation of the target image which is immediately corrected. Furthermore, the position of the orientation rod relative to the position of the sides of the whole target is checked to determine the rotation angle of the phantom. The corresponding location of all features in the rotated image is then automatically stored in a file for further processing. In the exemplary output of the two tools in Fig. 3.8 not all of the sides of the inset were detected. However, for the further processing only the location of the center rod and the sides of the target are used, therefore the absence of one of the unused features is not considered as a failure.
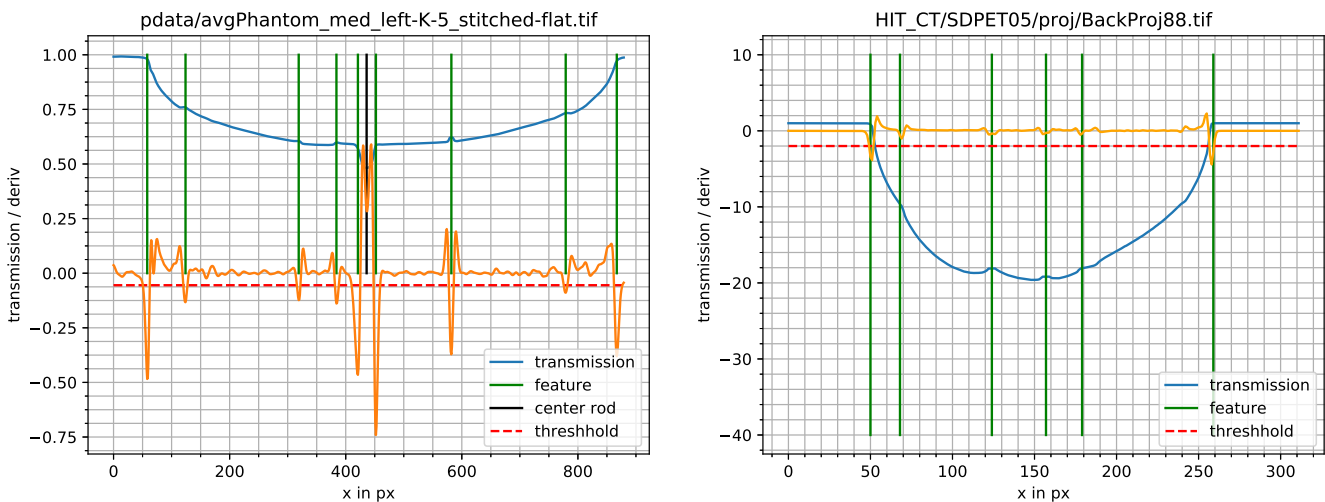

Figure 3.8.: Exemplary output of the feature detection software *pdetect.py* (left) and *xdetect.py* (right).

Assembly of the recalibration curve

The assembly of the recalibration curve is done in two steps using two different tools. First, the corresponding proton and X-ray images are semi-automatically overlapped using the tool *trchk.py*. For this, both images and the corresponding files containing the location of the features from *pdetect.py* and *xdetect.py* are loaded and the smaller X-ray image is automatically scaled to the size of the larger proton projection. Using the location of the orientation rod, the proton and X-ray projections with the same rotation angle are automatically chosen, however, it is possible to verify and manually adjust the choice of the software in case of a significant deviation. Afterwards, the part of the orientation rod is cut out from the profile as the X-ray images were captured without the rod to avoid any artifacts during the CT reconstruction. The remaining correlation between relative HU and proton transmission can then be plotted and exported for the *xctp2pctp.py* tool. The output of this software is presented and discussed in Sec. 4.11. With the second tool, the data from one or several proton / X-ray images can be used to fit a calibration curve. As the exact physical and therefore mathematical correlation between both values is unknown, a spline fit is used to describe the data. The shape of the curve shows an exponential decrease and a characteristic shoulder at high transmission (above 90 %) or small HU. The used *UnivariateSpline* fit of the *interpolate* package in *Python* only allows a degree of $k = 5$ which is not sufficient for describing this complex shape. Therefore, the spline can be separated into two parts maintaining the continuity conditions at the transition spot. For the characteristic shoulder a spline with a degree of $k = 5$ is used, for the rest of the curve a degree of $k = 3$ delivers the best result. The split point as well as the weight of the data points in the shoulder is adjusted automatically by the software using a penalty mode. This means that depending on the input dataset the location of the split is chosen so that the overall deviation between the experimental data and the spline fit is minimized. The *xctp2pctp.py* tool is furthermore optimized for multi-core CPUs to speed up the processing of data stacks.

Recalibration of radiographic images

After converting the HUs to proton transmission a further recalibration is necessary to transform the transmission values into areal density. Inverting the transmission formula (see Eqn. 2.41) is mathematically challenging, therefore again a spline fit of the order $k = 5$ is used in the tool *pcal.py*. If the overall deviation between the spline and the transmission curve is worse than 0.2 %, a fall back mode [81] is integrated based on dividing the horizontal axis (target thickness) into buckets of a width of 0.01 mm. This lookup table is then used instead for the recalibration. Although both variants are optimized for multi-core support, the speed of the lookup table approach is still considerably slower than the spline approach.

3.6.3 Tomographic reconstruction

For tomographic reconstruction two different tools have been developed to enable the handling of the obtained clinical image data. Although the raw output of the used CT scanning devices is accessible, this data itself is encrypted in a SIEMENS specific format and cannot be read by

any available software. Therefore, the easiest approach is to make use of the reversibility of the Radon transformation.

For obtaining projections from a tomographic set of slices we make use of the classical Radon transformation $Rf(L)$ which is the line integral in the space of straight lines L in a classical two dimensional space $\mathbb{R}^2$. Equation 3.1 gives us a a sinogram of each slice, out of the stack of sinograms it is possible to obtain transmission projections by selecting always the same line in each of the obtained sinograms and assembling them into an image.

$$Rf(L) = \int_L f(\mathbf{x})\,|d\mathbf{x}| \tag{3.1}$$

This can be done using the newly developed command line tool *revct.py*, which is based on the highly optimized *Python* package *skimage* including also a method for the radon transformation. As all calculations between loading the stack of CT slices and assembling the projections are independent, the *multiprocessing* package is used to parallelize the tasks and to significantly boost the speed of the application.

For an actual forward tomographic reconstruction the Radon transformation can be inverted reading

$$f(\mathbf{x}) = \int_0^\pi (\mathscr{R}f(\cdot,\theta) * h)(\langle \mathbf{x}, \mathbf{n}_\theta \rangle) d\theta, \tag{3.2}$$

where θ is the corresponding angle of the projection. Here, we apply a convolution kernel h for filtering the back projection which is mandatory for reducing the blurring of the calculated slices [82]. This variant of the inverse Radon transformation is therefore referred to as *Filtered Backprojection*. The best results can be obtained by using a *Hamming* filter, a modification of the classical *Von-Ham* filter shown in Eqs. 3.3.

$$w(n) = \alpha - \beta \, \cos\left(\frac{2\pi n}{N-1}\right), \quad n = 0, \dots, N-1 \tag{3.3}$$

Instead of $\alpha = \beta = 0.5$ we chose $\alpha = 0.54$, $\beta = 0.46$ for improving the suppression of unwanted high frequency components.

The developed tool *fwdct.py* also makes use of the possibility for task parallelization and is capable of reading arbitrary experimental and simulated data.

4 Evaluation

During the course of the project, four separate beam times using all three different lens systems of the pRad facility at LANL (see Sec. 3.1.2) with three different camera/detector setups (see Sec. 3.1.3) were conducted. This was mostly caused by the fact that the project was not granted a dedicated beam time slot, neither at Los Alamos nor at GSI where bureaucratic obstacles delayed the manufacturing and commissioning of the new PRIOR-II setup described in Sec. 2.5. Therefore, most of the data was collected as a parasitic user of the accelerator facility thus creating a large number of different experiment scenarios. Besides complicating the analysis of the data as the detector systems produce different outputs that require individual handling this also affects the comparability of the different results. Furthermore, – in addition to a different behavior of the accelerator during each campaign affecting the stability of the beam and therefore the flattening procedures – the different target placement conditions either in an air gap or in a vacuum vessel affect the accuracy of the density calibration itself and contribute to the overall error of the measurements.

A full overview of all of the performed measurements and the corresponding setting of the facility is shown in Tab. 4.1. This includes also a resolution target eroded from tantalum (*Ta resolution*), foreseen for benchmarking the PROSIT simulation code, which is not presented within the scope of this work. Several issues affecting either directly the measurement or the evaluation are discussed in Sec. 4.8.

System	Beamtime	Target placement	Detector	Target(s)
LANL x3 EM	**SEP16**	Vacuum (Vessel)	Rockwell/LSO	head phantom x1 aluminum wedge x3 PMMA wedge x3 TE wedge x3
LANL x1	**OCT16**	Vacuum (Vessel)	Rockwell/LSO	head phantom x1 Ta resolution x1
LANL x3 EM	**NOV16**	Air	pco.dimax/LYSO	aluminum wedge x3 PMMA wedge x3 TE wedge x3 Ta resolution x3
LANL x7 SmCo	**DEC18**	Air	HiSense/LYSO	head phantom x7

Table 4.1.: Overview of the collected data during the four beam times at LANL.

4.1 Investigations on the depth of field

As described in Sec. 2.3.3, the initial beam preparation (matching) does allow for the canceling of the most significant second order term T_{116}, the position dependent chromatic aberrations. However, the weaker T_{126} term does still contribute to the final image resulting in the definition of the *chromatic length* (Eqn. 2.30) as a measure of the spatial resolution capabilities of a radiographic setup. The magnets of such a device are tuned to enable point-to-point focusing at a certain beam energy leading to a shift of the focal spot upstream or downstream of the beam axis in case of any deviation from this energy (see Fig. 2.8). This second order effect, caused mostly by the T_{126} term but also higher order effects, leads to a blurring of thicker areas of the imaged object (higher deviation from the main beam energy due to a higher energy loss). This effect is widely known as the limitation of the depth of field. It is naturally more pronounced for large apertures or – in case of proton radiography – for large collimators.

In case of a decreased collimator size, the effect can partly be canceled as protons exiting the target with a large deviation from the main beam energy will have also experienced more scattering. Those protons travel on trajectories further away from the beam axis and will therefore be sorted out already at the entrance of the collimator. The influence of this effect has been addressed by experiments using the two part step wedge milled from aluminum which is described in detail in Sec. 3.4.1. The dimensions of the wedge are chosen in a way so that the transmission range – using a 5 mrad collimator – covers the whole transmission range with a transmission from 10 - 90 %.

The x3 version of the wedge was imaged with the x3em magnifier using both the Rockwell and the pco.dimax camera setup. For an analysis of the amount of blurring depending on the collimator acceptance the experiment (in case of the pco.dimax run, **NOV16** beam time) was repeated with all four available collimators with the acceptances 2.5, 5.0, 7.5 and 10.0 mrad. The Rockwell data was collected during the **SEP16** beam time with just the 7.5 mrad collimator and is – mainly due to poor image quality – not shown in this section. It was still analyzed as the determination of the parasitic scattering angle θ_0 is mandatory for the recalibration attempt of X-ray data described later in Sec. 4.3.1. The **SEP16**/Rockwell data was collected with a tune energy of 790 MeV corresponding to a current of 1206 A for the outer lenses Q1,Q4 and 1318 A for the inner lenses Q2,Q3. The target was placed in the vessel for experiments with explosives in vacuum, which is sealed on both ends upstream and downstream of the target location by 0.25 inch (6.35 mm) thick aluminum windows. The lin80 pattern was chosen for the irradiation. The pco.dimax data was collected at a tune energy of 794 MeV corresponding to 1217 A for the outer and 1321 A for the inner lenses. Here the target was placed on the LANL goniometer in an air gap, the ends of the beam pipes at the target location were sealed with 20 mil ($\sim$0.5 mm) Kapton windows. For the 2.5 mrad collimator the lin200 pattern was used, for the 5.0 and 7.5 mrad collimators the lin100 pattern and for the 10.0 mrad collimator the lin80 pattern. The flattened data is presented in Fig. 4.1.

The radiograph captured with the 5.0 mrad collimator (Fig. 4.1(b)) shows a vertical artifact caused by the split of the LYSO scintillator into two tiles. Usually this cut is not visible as it

is canceled during the flattening, however, a mechanical shift of the camera setup between capturing the target images and capturing the *white field* images of effectively just 1 px reveals the transition line. The radiographs captured with large acceptance collimators (Figs. 4.1(c) and 4.1(d)) illustrate the effects of the limited depth of field but also show the limning artifact discussed in Sec. 2.3.6.
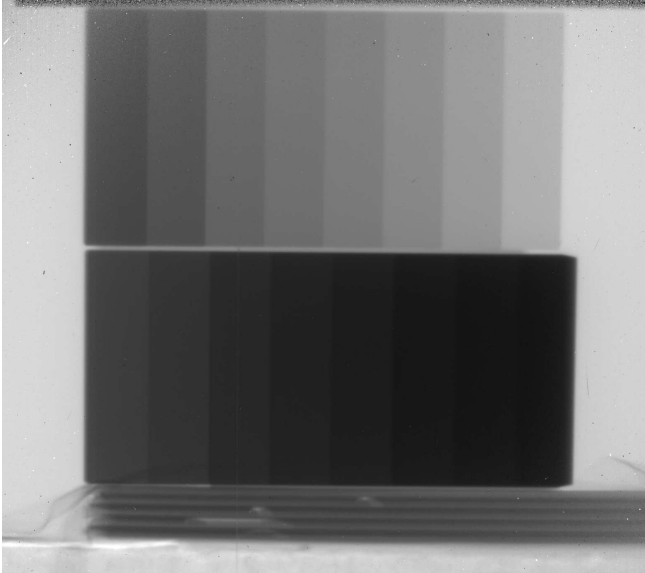
(a) x3em proton image of the Al wedge (with 2.5 mrad collimator).
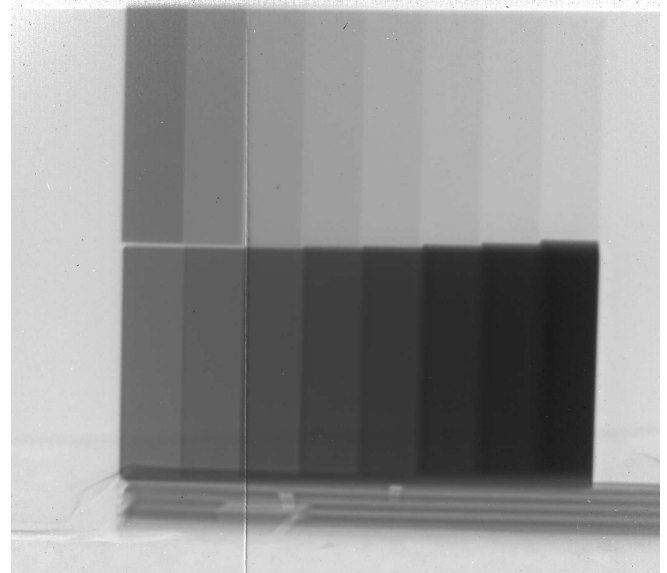
(b) x3em proton image of the Al wedge (with 5.0 mrad collimator).
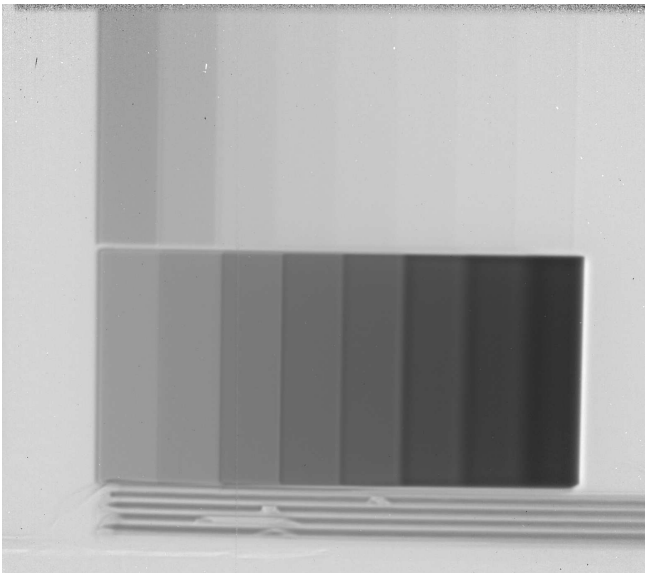
(c) x3em proton image of the Al wedge (with 7.5 mrad collimator).
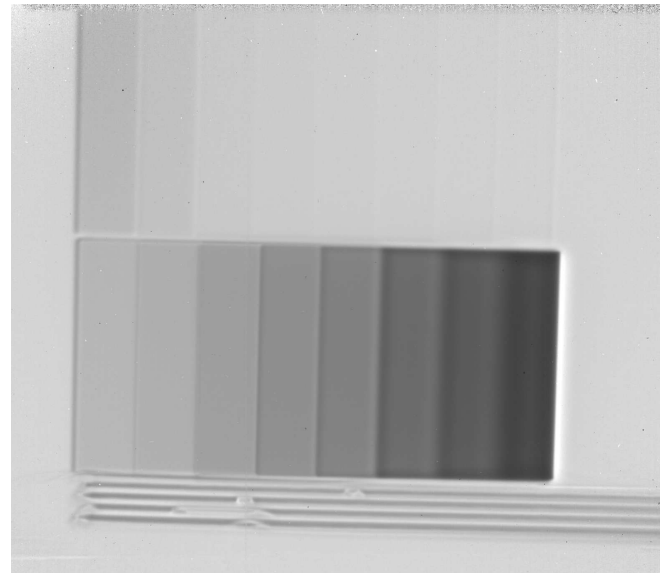
(d) x3em proton image of the Al wedge (with 10.0 mrad collimator).

Figure 4.1.: Proton radiographs of the Al wedge. The vertical artifact in the top-right radiograph is caused by the split of the LYSO scintillator in two tiles. Especially in the lower part of the bottom-right radiograph (10.0 mrad) the limning effect is extremely pronounced significantly blurring the thick part of the wedge.

For a better visualization the horizontal transmission profile of the lower, thicker part of the wedge is extracted from Fig. 4.1(d) and plotted in Fig. 4.2. Towards low transmission it can be observed that the limning effect is overlapping with the blurring causing a significant distortion of the transmission. This holds especially for the two rightmost steps where practically no flat region remains for reconstructing the corresponding density from the transmission. This, however, is a severe problem only for this type of experiments but less important for biomedical imaging since limning only occurs at transitions with a high density gradient. In soft tissue there are no such steep transitions leaving only the blurring which does affect the image quality but – as long as the geometry of interest is larger than the remaining spatial resolution performance with blurring – not the density information.
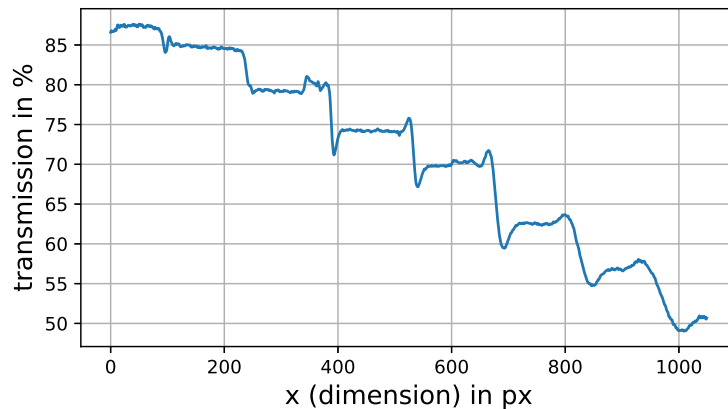
Figure 4.2.: Transmission profile of the lower/thicker part of the aluminum wedge imaged with the x3 magnifier and a 10 mrad collimator (see Fig. 4.1(d)).

In addition to investigations on the image quality the data was also analyzed with regard to the density reconstruction accuracy. For this, the theoretical transmission curve (the unknown parasitic scattering angle θ_0) was fitted for each collimator, then the average θ_0 was calculated for plotting the corresponding transmission curves along with the data itself. This revealed an obvious offset between the thinner and thicker part of the aluminum wedge which is visualized in 4.3. An analysis showed that both parts of the aluminum wedge were not manufactured from the same material but from different alloys (Al7075 and Al6061).

Al7075 - thinner wedge
Zn - 5.8 %, Mg - 2.3 %, Cu - 1.4 %, Al - 90.5 %
ρ =2.81 g/cm^3
nucl. collision length = 0.2515 m, rad. length = 0.07980 m

Al6061 - thicker wedge
Si - 0.6 %, Cu - 0.2 %, Mg - 1.0 %, Al - 98.2 %
ρ =2.70 g/cm^3
nucl. collision length = 0.2586 m, rad. length = 0.08823 m

Assuming the compositions above which represent an average of the min/max specifications for the respective alloys, the nuclear collision and radiation lengths were calculated using the tool GSI Atima. The exact composition is unknown and may vary also due to heavier trace elements, a full chemical analysis could unfortunately not be performed at LANL. The transmission curves were refitted separately obtaining an average θ_0 of (2.300±0.311) mrad for the experiments with the pco.dimax/**NOV16** and a θ_0 of (4.384±0.173) mrad for the single run with the Rockwell/**SEP16** imaging setup. The final result showing the data and fits is plotted in Fig. 4.3. Although the Highland approximation does represent the data very well, there is a visible offset between the data and the model at high densities at the far right side of Fig. 4.3 which is not depending on the collimator size. Here, the measured transmission – especially at the thickest step – is considerably higher than the one predicted by the model. The offset of the Rockwell data point with the highest areal density could be explained by limning and blurring addressed earlier in this section. The reason for the effect in the pco.dimax data is up to now not fully understood and can most probably be attributed to the CDS mode of the pco.dimax camera discussed in Sec. 4.8.2 which mostly affects low transmission areas.
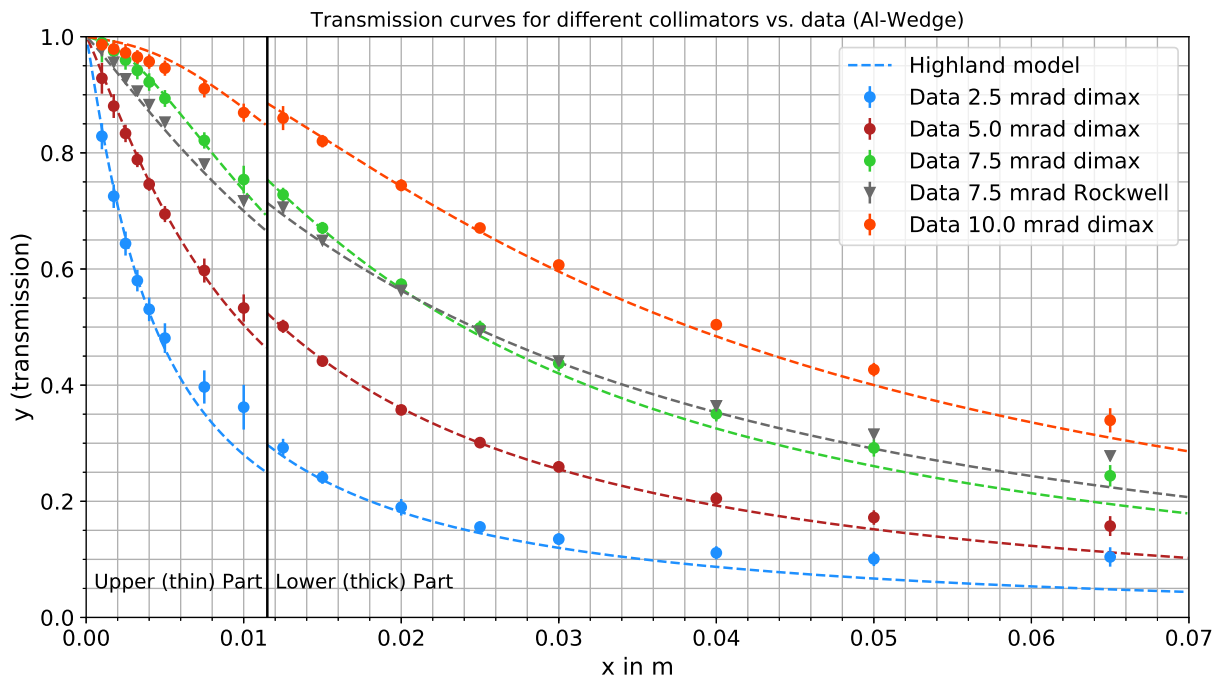
Figure 4.3.: Combined data of the pco.dimax and Rockwell x3em experiment with the aluminum wedge as well as fitted theoretical curves of the transmission model.

4.2 Proton flux dependent density resolution performance

For any medical purpose of this imaging method the reduction of the dose to the patient is the highest priority. Therefore, the proton flux from the accelerator has to be reduced to a minimum to avoid any additional unwanted exposure to radiation. The flux dependent density resolution performance was measured using the PMMA step wedge with steps showing a decreasing difference in areal density from 0.585 to just 0.029 g/cm^2 (see Sec. 3.4.1). PROSIT simulations (see

Sec. 3.3.2) were performed in advance to estimate the required particle flux, however, those simulations cannot reflect all external effects like detector blurring. This is especially crucial as detector blur does influence the image quality in a negative way in case of high proton flux – at low proton flux it may in certain scenarios even enhance the overall image quality. The MC simulation can only map single particle events, therefore at a low flux the image plane will only show discrete events especially if $n_{p+} \sim n_{px}$, where n_{px} equals $4 \cdot 10^6$ in case of the pco.dimax detector setup. For the PROSIT simulations, the effective detector pixel count has therefore been reduced to 1e3 x 1e3 px^2 to curtail the influence of this effect for low statistics. This reduction is still sufficient to not affect the spatial resolution performance as the pixel size at the detector is 132.7 μm, effectively 47.8 μm at the object considering the magnification of the x3em setup. This special type of detector is referred to as dimax 1k. The configuration was equivalent to the run with the aluminum wedge already described in Sec. 4.1, the images captured using the Rockwell detector setup took place in the vessel for high explosives whereas the pco.dimax data was captured in an air gap. The tune energy of 790 MeV corresponds to 1211 A for the outer and 1315 A for the inner lenses. In case of the 10.0 mrad data a slight deviation was monitored attributed to the instability of the power supplies. Here, 1214 A for the inner and 1317 A for the outer lenses was recorded. For the Rockwell data as well as for the 10.0 mrad pco.dimax dataset the lin80 beam pattern was used, for the 5.0 mrad and 7.5 mrad the lin100 pattern and for the 2.5 mrad data the lin200 pattern.
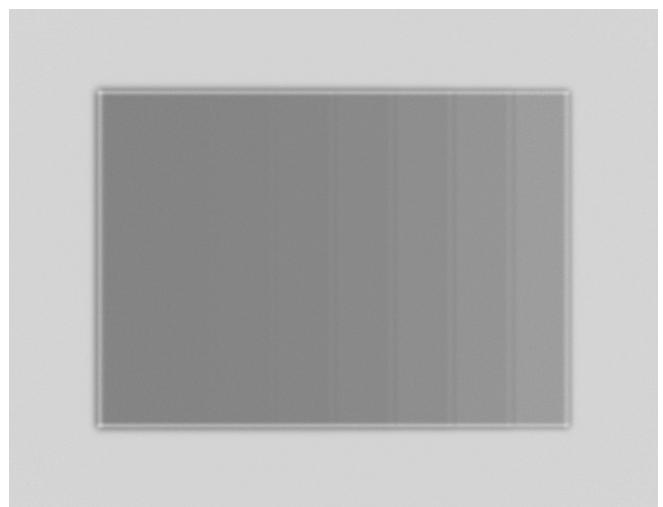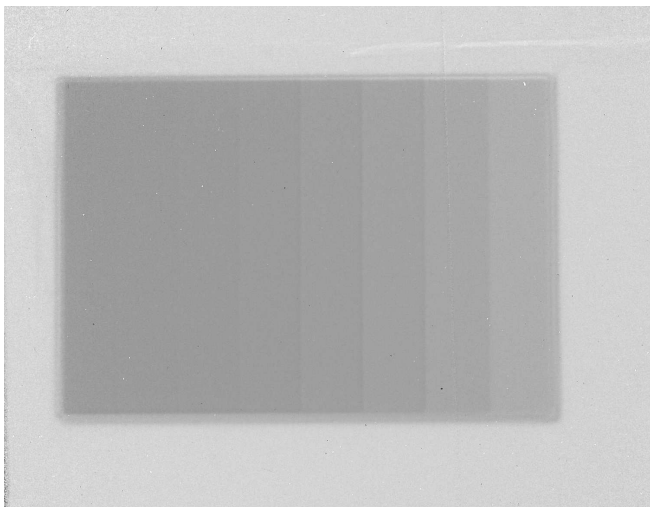
(a) Radiograph of the PMMA wedge using the x3 magnifier and a 7.5 mrad collimator.

(b) PROSIT simulation of the PMMA wedge using a 7.5 mrad collimator.

Figure 4.4.: Comparison between the experimental x3 data and a PROSIT simulation using the same setup with equal settings.

According to the design parameters of the target where a 5.0 mrad collimator is foreseen, for PROSIT we chose the same setting as for the actual experiment settings using the pco.dimax detector system but instead a 7.5 mrad collimator. This is mandatory since the 5.0 mrad pco.dimax data of the PMMA wedge shows the same vertical artifact caused by a mechanical shift in the detector system as already described in Sec. 4.1. We define the standard deviation of the trans-

mission in a selected area on the steps as a measure for the density reconstruction accuracy. This choice is obvious as two steps cannot be distinguished anymore if the fluctuation of the transmission is higher then the actual difference in transmission between the two steps. The areas cover $6.5\,mm^2$ on the steps, they are vertically centered on the image and horizontally centered on each step. A comparison between the raw experimental and raw simulated data is shown in Fig. 4.4.
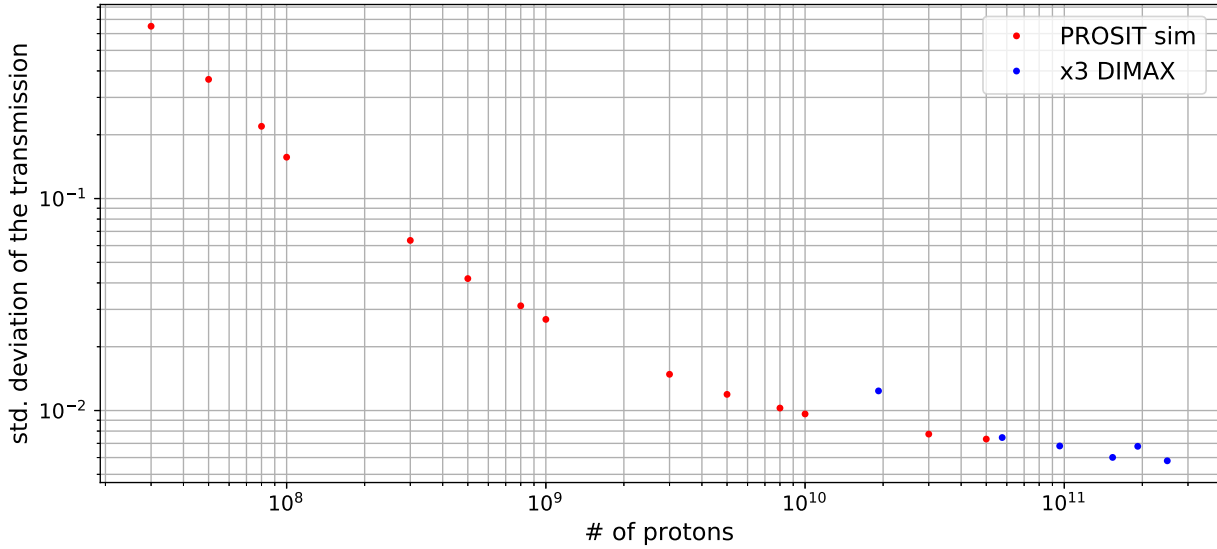

Figure 4.5.: Proton flux dependent density resolution (measured and extrapolated with PROSIT data to low flux).

Limited by the operation mode of the accelerator at the time of the experiment (see Sec. 3.1.1) the minimum statistics for a single image was $5.6 \cdot 10^8$ protons for the Rockwell detector setup and $1.92 \cdot 10^{10}$ protons for the pco.dimax detector setup. This is – in case of the pco.dimax data – above the calculated desired threshold for clinical applications, therefore, we can only extrapolate the experimental data down to lower doses. The standard deviation depending on the proton flux is then plotted in Fig. 4.5. The Rockwell data was again neglected as the occurrence of artifacts affected the image quality in a severe way.

Analyzing Fig. 4.5 it is obvious that a reduction of the flux and therefore theoretical dose to the patient is certainly possible but comes at the cost of a lower density accuracy. Up to 10^{10} protons the density resolution is below $1\,\%$ transmission, at around 10^8 protons, which is a lot more favorable in terms of dose, the resolution would drop just below $10\,\%$ transmission.

Just as with the aluminum wedge a comparison between the experimental data and the theoretical transmission model was performed. The unknown parasitic scattering angle was fitted for each dataset and then averaged leading to $\theta_0 = 2.386 \pm 0.414\,mrad$ for the pco.dimax/**NOV16** datasets and $\theta_0 = 4.015 \pm 0.016\,mrad$ for the Rockwell/**SEP16**. This is in very good agreement with the fit data obtained from the aluminum wedge. The fits are then plotted along with the captured data in Fig. 4.6. This approach is not suitable for the determination of unknown material properties but does confirm the validity of the model and delivers a θ_0 which can be used for the evaluation of different, unknown targets (e.g. for the phantom). Due to the limning effect it is obvious that especially the steps at both sides of the target are affected by a transmission
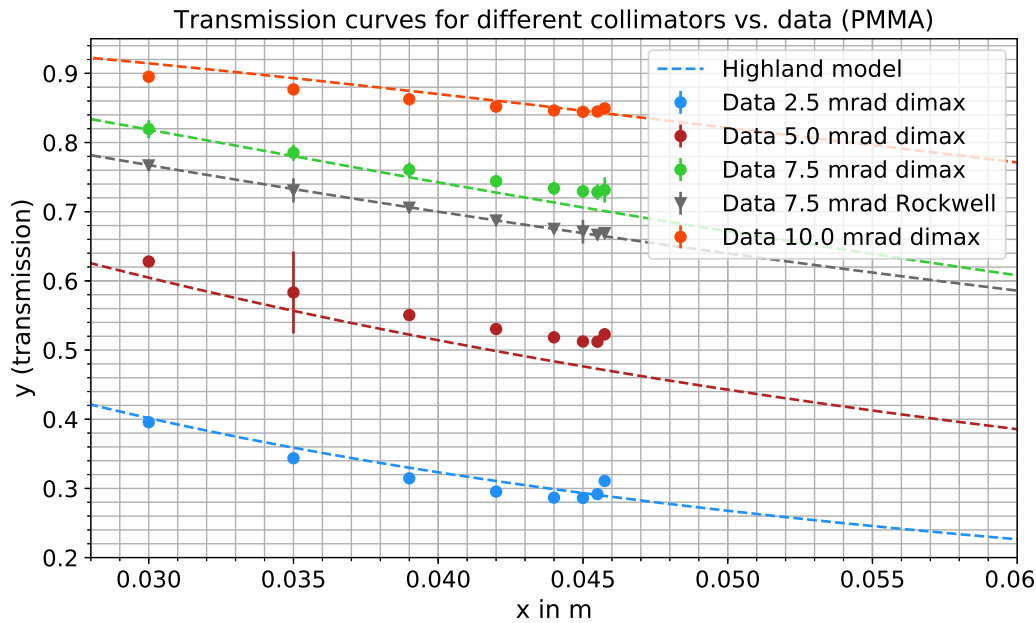
Figure 4.6.: Combined data of the pco.dimax and Rockwell x3em experiment with the PMMA wedge alongside with the fitted theoretical curves of the transmission model.

shift due to the steep change of the areal density. The overshoot is extremely pronounced for the pco.dimax/**NOV16** data point/step with the highest areal density and collimators with small acceptances, however, in the Rockwell dataset it is barely visible. This leads to the assumption that the choice of the focal energy should have been more accurate to reduce the blurring (the theoretical energy loss in the target is around 12.2 MeV).

4.3 X-ray measurements at Heidelberg

During the X-ray measurement campaign at the university clinic in Heidelberg several datasets of the x1 clinical head phantom with all of the available scanners have been collected. For a quality analysis of the obtained CTs three settings have been chosen which are one clinical setting "A" as well as two further settings "B" and "C" exploiting the maximum capabilities of the machine (see Tab. 4.2). The corresponding tomographic reconstruction on the servers of the university clinic was performed using Siemens software and several available kernels from the Siemens database (see Sec. 3.2).

The used reconstruction kernels do enhance certain features of the images which makes a comparison of the stability of the absolute HUs between different measurements necessary. Furthermore, the noise level of the HUs when using different reconstruction kernels has been investigated. As an example, the high density phantom imaged with the Biograph 40 scanner is chosen as the device had the highest availability and therefore allowed for the most measurements. The presented data points refer to circular selections on the CT slices covering ~80 % of the area of the insets to avoid any artifacts at the steep transition between inset and PMMA casing which might occur during the reconstruction. An example of the result of a reconstruction for different scanners is presented later in Sec. 4.5.

CT Scanner	Col.	voltage	current	pitch	slice	setting
Biograph 40	40 x 0.6	80 kV	400 mA	0.30 mm	0.4 mm	-
	40 x 0.6	120 kV	300 mA	0.35 mm	3.0 mm	A
	40 x 0.6	120 kV	300 mA	0.35 mm	0.6 mm	B
	40 x 0.6	140 kV	400 mA	0.30 mm	0.4 mm	C
Somatom Confidence	64 x 0.6	80 kV	400 mA	0.35 mm	0.5 mm	-
	64 x 0.6	120 kV	300 mA	0.35 mm	3.0 mm	A
	64 x 0.6	120 kV	300 mA	0.35 mm	0.5 mm	B
	64 x 0.6	140 kV	400 mA	0.35 mm	0.5 mm	C
Sensation Open	40 x 0.6	80 kV	400 mA	0.45 mm	0.6 mm	-
	24 x 1.2	120 kV	300 mA	0.45 mm	3.0 mm	A
	40 x 0.6	120 kV	300 mA	0.45 mm	0.6 mm	B
	24 x 1.2	120 kV	400 mA	0.45 mm	1.5 mm	-
	40 x 0.6	140 kV	400 mA	0.45 mm	0.6 mm	C

Table 4.2.: Overview of the settings of the captured X-ray scans.
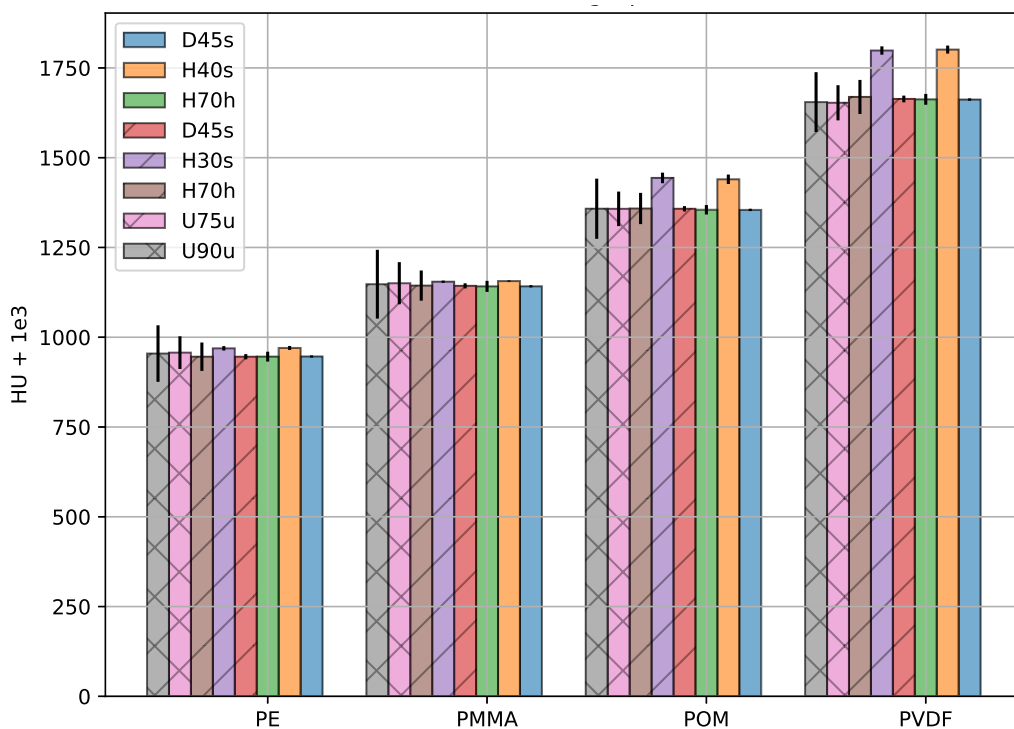
Figure 4.7.: HU fluctuations between different measurements and standard deviation at the corresponding location on the slice (noise level) on the Biograph 40 scanner. Double crossed - "C", Striped - "B", No filling - "A".

In Fig. 4.7 it can be observed that the HU values are not constant for different kernels. Especially the *H30s* and *H40s* kernels deliver a different result than the *H70h* kernel although all of them are specialized head kernels and will make use of the same HLUT for the conversion

to WEPL for particle therapy applications. With increased kernel number not only the spatial resolution performance, but also the noise level and therefore the error of the selected area, increases. This is shown in detail in Fig. 4.8 for the different kernels and plotted dependent on the respective insets sorted by density. No systematic dependence on the density can be observed, however, only the smoothed kernels like *D45s* and *H30s* show a noise level below the one percent level. This behavior of the sharp kernels drastically reduces the density resolution performance, the smallest investigated change in density of 0.36 % between two of the TE insets cannot be resolved.
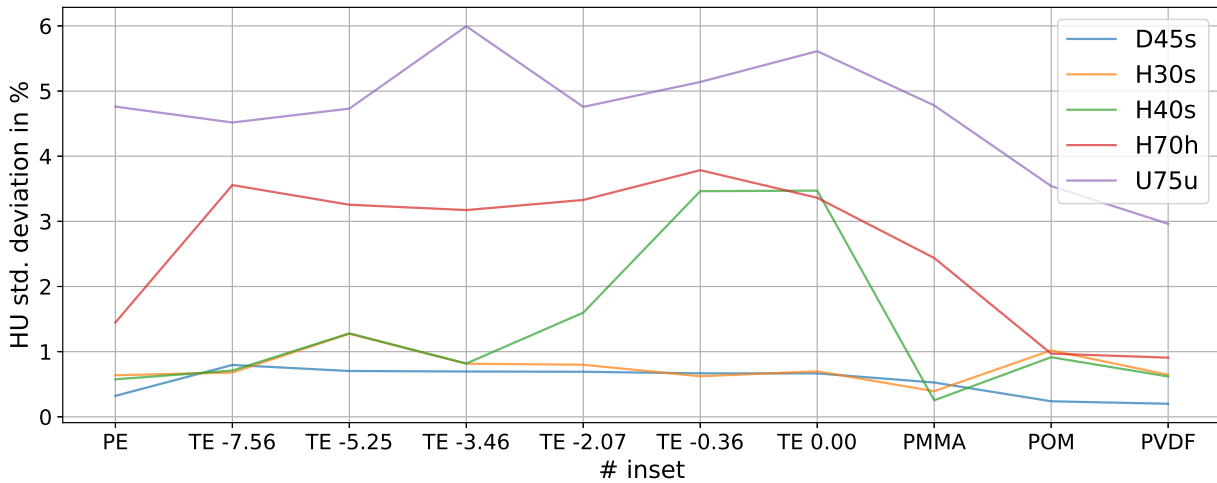
Figure 4.8.: Fluctuation of the HU in % (standard deviation) for different reconstruction kernels on the Biograph 40 scanner dependent on the respective insets sorted by density (density dependent noise level).
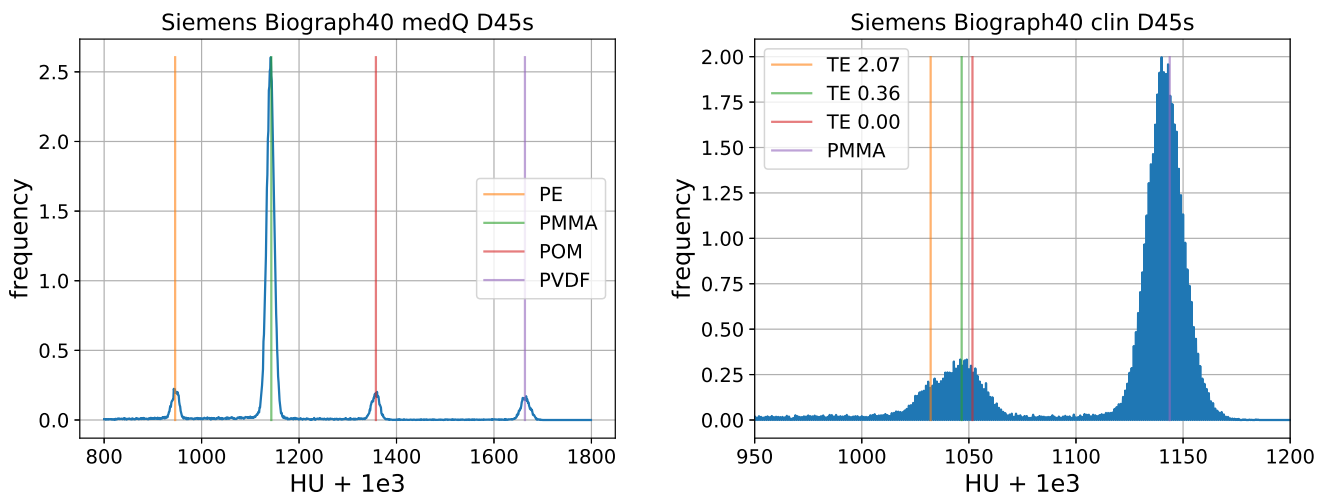
(a) Histogram representation of the high density phantom CT.

(b) Histogram representation of the tissue equivalent density phantom CT.

Figure 4.9.: Comparison between the histogram representation of the low density tissue equivalent phantom and the high density phantom.

By transforming the image data into a histogram this can be visualized easily. Whereas the data of the high density insets shows clear separated peaks due to the huge differences in density (see Fig. 4.9(a)), the peaks of the low density insets – especially the ones of the TE base material and the 0.36 % step in Fig. 4.9(b)) – do overlap and could only be separated analytically.

4.3.1 Recalibration

The recalibration described in Sec. 3.6.2 has been performed using proton images from the x3em and the x1 setup at LANL. For both setups the tune energy was 785 MeV resulting in $I_1(Q_1/Q_4) = 1530.0$ A, $I_2(Q_2/Q_3) = 1526.2$ A for the x1 lenses and $I_1 = 1201.0$ A, $I_2 = 1313.0$ A for the x3em lenses. The x1 setup was equipped with a 10.0 mrad collimator and 0.5 mm Kapton vacuum windows, the x3 setup with a 7.5 mrad collimator and 6.25 mm aluminum windows. In both cases the *lin80* pattern delivering about $1.92 \cdot 10^{10}$ protons per pulse was used. All of the experiments were conducted in the vacuum vessel for high explosives, significantly limiting the adjustment capabilities.
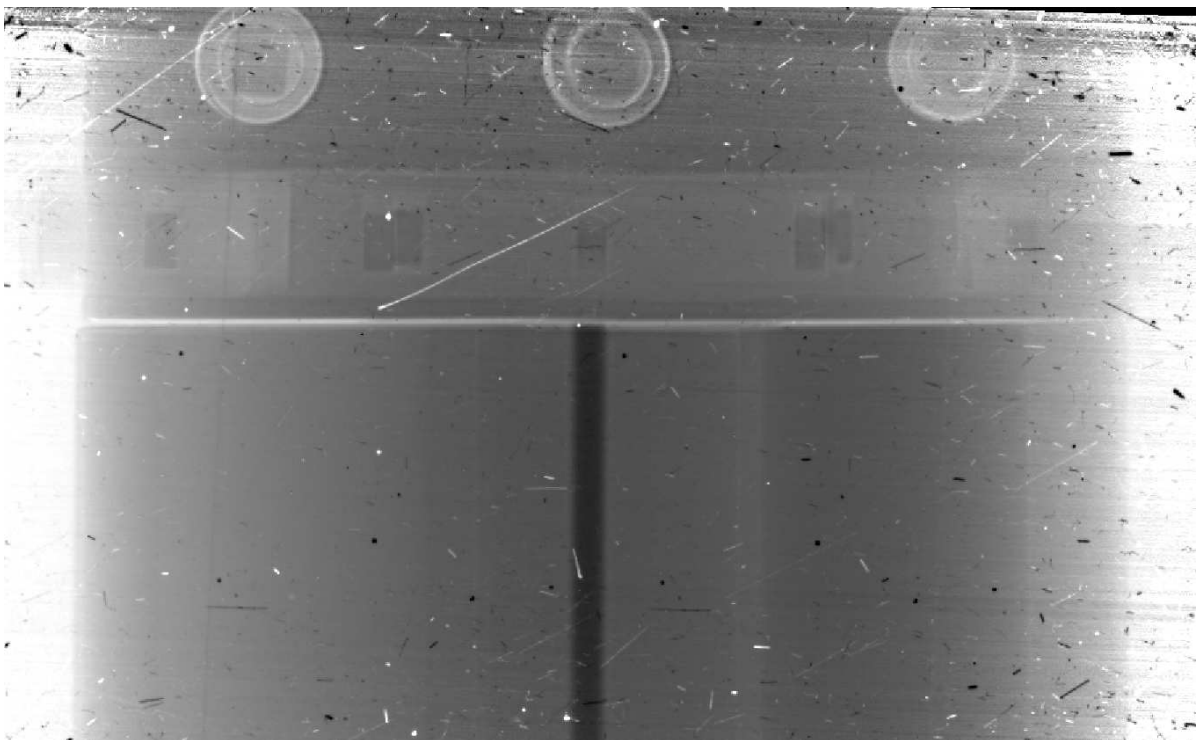
Figure 4.10.: Stitched and flattened x3em projection of the structure head phantom. In the top part the dosimetry cap is situated, the resolution is good enough to see the individual TLDs used for the dosimetry. The bottom part shows the three structure density insets (left - PE, middle - POM, right - PVDF) as well as the centered stainless steel orientation rod.

In case of the x3em setup the phantom does not fit inside the field of view, therefore images of the left and right side of the target were captured. This was possible using the step motors of the target stage inside the vessel which allow a horizontal displacement perpendicular to the

beam axis by around 30 mm. The corresponding two images per phantom were captured at -12 mm and +12 mm displacement, the phantom itself was positioned so that the orientation rod was situated roughly centered on the whole target in the beam eye view. The two parts were then stitched together using the position of the orientation rod as an indicator. For this purpose the tool *stitch.py* was developed which contains an interactive mode based on the matplotlib GUI for combining separate images. The tool can add a plane tilted in horizontal direction simultaneously to the intensity level of both images to compensate for flattening errors. It is also possible to adjust the overall intensity level. Both procedures can be performed manually or automatically by fitting a straight line to the non-target regions of the profile and adjusting the gradient and individual intensity levels so that the non-target region remains as flat as possible. However, as all adjustments just affect the intensity in horizontal/x direction, the flattening tool for radiographic data (see Sec. 3.6.1) has to be used in advance on the single images. The stitching procedure was not mandatory for the x1 data, those radiographs were flattened using just the conventional tools *quickpr.py* and *flattengui.py*. A stitched projection captured with the x3em setup is presented in Fig. 4.10.

On the X-ray side consequently the setting "C" for the best image quality is used. As the Siemens Biograph 40 machine delivered the best image quality (see Sec. 4.5) only those CTs were used for the recalibration.
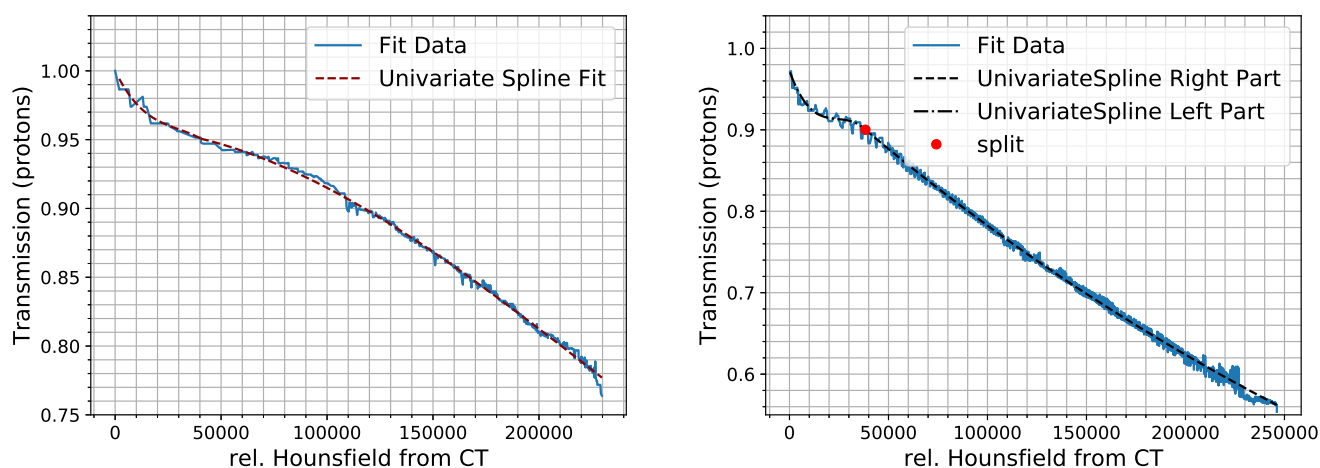
(a) Averaged recalibration data and spline fit of the x1 data.

(b) Averaged recalibration data and spline fit of the x3em data.

Figure 4.11.: Raw recalibration data extracted from overlapping the X-ray projections with corresponding proton projections (x1 and x3em data). The large relative HU originate from the inverse Radon transformation as the procedure requires summing up pixel values over the diameter of the whole phantom.

Employing the tools described in Sec. 3.6.2, first the radiographs and X-ray projections were rotated and cropped, then the location of the sides of the phantom and the position of the center rod were detected. The positions of the sides are required for the overlapping procedure, the position of the center rod is mandatory for identifying the X-ray projection with the correct rotation angle. Having obtained this data, the *trchk.py* tool automatically selects the matching

proton and photon projections and scales the X-ray data up to the size of the proton projection. The projections are then overlapped which leads to a correlation between the relative HU from the X-ray CTs and proton transmission. This correlation is shown in Fig. 4.11 and is – as the proton transmission curve itself is dependent on the collimator acceptance and the initial angular spread θ_0 of the beam – also dependent on those quantities. Therefore, the x1 and x3em results show a different curvature of the correlation. At high transmission / low relative HU numbers a dent is visible in the correlation, especially in case of the averaged x3em data. This is either attributed to the general shape of the proton transmission curve (see Sec. 2.3.5) but could also be caused by low statistics. More measurements with different collimators and possibly a different parasitic θ_0 will be required to confirm one of those assumptions. In the same region of the x3em correlation an oscillation of the data with an amplitude of about 2 % transmission is visible indicating a possible transmission offset between the left and right side of the proton projection. This could be caused by several factors or even an interplay of several factors, e.g. by the flattening or the stitching procedures, by a slight misidentification of the sides of the target during the feature detection caused by artifacts or even by a small horizontal displacement caused by the upscaling of the X-ray projection.

In the following step the stack of projections was recalibrated with the *pcal.py* tool. This requires the specification of the parasitic scattering angle θ_0 which is usually unknown. Theoretically it can be measured at the LANL since a separate identity lens is situated in front of the used target position. At the fourier plane of this setup it would be possible to measure the angular distribution of the beam with a suitable scintillation detector, however, this is currently not forseen. Therefore, two different attempts were conducted to investigate this quantity. For the x3em data two separate measurements were available presented in Sec. 4.1 and 4.2. From those two experiments a mean $\theta_0 = 4.20$ mrad can be extracted which was then used for the recalibration process. This was not possible in case of the x1 data since no separate measurements were available. In this case the parasitic scattering angle was determined by analyzing the evenness of the profile of a reconstructed CT slice. Starting from the fact that a variation of θ_0 mostly affects the high transmission areas and therefore low areal density regions of the transmission curve, it can be concluded that the sides of the target in a projection will then show either a too high or too low transmission depending on θ_0. Reconstructing CT slices from those false profiles leads to a bent surface of the otherwise flat target surface. A parameter scan of θ_0 led to an average parasitic angle of 1.48 mrad for the x1 dataset which is below the x3em result [83] despite almost equal conditions. This can be explained by the choice of the windows of the beam pipe upstream of the target. At 800 MeV the 6.25 mm Al window would lead to an additional $\sigma_\theta = 2.963$ mrad whereas the 0.5 mm Kapton window only results in an additional $\sigma_\theta = 0.468$ mrad. However, performing the same procedure for the x3em data led to an average θ_0 of 2.85 mrad which does not agree with the experimentally obtained data. It can be concluded that the second method using CT slice profile seems to underestimate the actual parasitic scattering, therefore, due to a lack of experimental data, the recalibration data from the x1 is not used for the evaluation in Sec. 4.6.

4.4 Proton tomography

The benefits of proton tomography (pCT) for medical applications using high energy proton radiography have been exploited using the x7 setup at the LANL (see Sec. 3.1.2). For this purpose the miniature version of the head phantom with standard type plastic insets described in Sec. 3.4.2 was placed and rotated on the LANL goniometer.

The refurbished x7 magnifier is based on SmCo PMQs, the lenses have a physical length of QL1,QL4 = 97.7 mm and QL2,QL3 = 195.1 mm. The object was placed in an air gap, the beam pipes at the object location were sealed with a 10 mil (250 μm) Kapton window upstream and a 1 mil (25 μm) Kapton window downstream of the object location. The drift distances between the lenses were adjusted to dl1 = 389.3 mm, dl2u = 221.8 mm, dl3 = 306.9 mm and dl2d = 222.9 mm corresponding to a tune energy of about 785 MeV. The distances between the outer and inner quadrupoles dl2u upstream and dl2d downstream were not equal after the fine tuning of the resolution during the commissioning runs prior to the measurement. For the experiment the *lin80* pattern was chosen delivering about 1.3·10^{10} protons[1] per pulse.
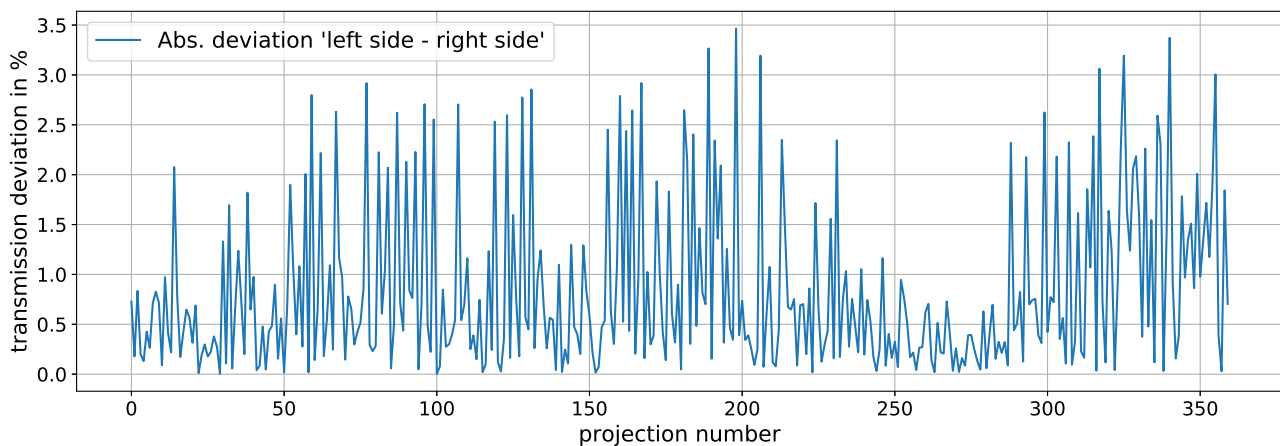
Figure 4.12.: Absolute difference in transmission between the left and right non-target region of the 360 pCT projections.

360 projections with a 0.5 degree spacing over a 180 degree rotation were captured along with 10 *dark field* images and 5 *white fields* images. Due to an extremely unstable beam profile and the occurance of Newton's ring artefacts caused by the lens of the Dantec camera the flattening and processing of the radiographs had to be performed manually using the tools *quickpr.py* and *flattengui.py* (see Sec. 3.6.1). The Newton's rings were neglected in the following flattening process as they occur inconsistently and can therefore not be corrected. An estimation of their influence is performed in Sec. 4.8.3. The object was set up in a way that on both sides a non target area suitable for analysis remained visible, therefore, a quality analysis of the performed flattening was possible. For this as well as for the further processing of the data the stack of projections was automatically cropped after the manual flattening to remove the frame of the scintillator crystal. Afterwards, the lower surface of the target was detected on the far left

---

[1]   Personal communication with M. Freeman, LANL.

and right side of the target by analyzing the derivative of a vertical profile extracted at those locations. With this information any unwanted rotation due to a misalignment during the experiment can be automatically detected and removed for the whole stack of projections. In the last step the sides of the target were detected by analyzing a horizontal profile in the same way as described above to center the target in every image. Then a comparison of the left and right non-target regions was performed which should both show 100 % transmission.

The absolute difference between the left and right non-target regions is plotted in Fig. 4.12. For the procedure a threshold of 3 % was set. If a single projection did not meet this requirement the flattening process was repeated until the threshold was reached. Due to the severe instability of the beam profile and just 5 available beam pictures this was not possible in every case. The average transmission deviation stemming from this procedure is 0.83 %, the maximum observed deviation is 3.47 %. In the high transmission range around 100 % assuming a water target this corresponds to an average target dimension error of 0.97 mm water up to 3.40 mm in the worst case scenario. However, the observed difference on both sides can partly also be attributed the Newton's rings as they – especially on the right side (see Fig. 4.14(b)) – severely affect the transmission values.

The parasitic scattering angle for the pCT target was determined by fitting the transmission of three step wedges (aluminum, copper and tungsten) imaged during the same run with the 5.0 mrad collimator. The data from the different wedges proved to give a consistent result leading to an average θ_0 of 5.558 ± 0.130 mrad.

The resulting radiograph as well as the CT reconstruction is presented in Fig. 4.14(b), a further analysis of the density reconstruction is described in Sec. 4.6.

4.5 X-ray vs proton radiography

In order to estimate the benefits of proton radiography, a qualitative and quantitative comparison between X-ray and proton single projections and X-ray and proton CT has been performed. The X-ray data were collected within the framework of the recalibration attempt described in Sec. 4.3.1, the proton data was either simulated or collected during the pCT experiment from Sec. 4.4. The performed comparison allows to evaluate the benefits of both techniques for feature/tumor detection and treatment planning. Again, only data from the structure phantom is used as it is the only one which was imaged with every different imaging method.

Despite the same X-ray data as for the recalibration approach being used, the results from the Siemens Somatom Confidence cannot be presented as inadvertent overwriting of the clinical settings at the HIT due to equal file names caused the loss of these data. The *clinical* and *maximum quality* settings correspond to the settings A and C (see Sec. 4.3). For the comparison to pCT, a separate proton dataset has been simulated with PROSIT using the LANL x3em setup but assuming a larger FOV to overcome the stitching. Experiment data comes from the **DEC18** beam time with the x7 head phantom and the x7 SmCo magnifier.
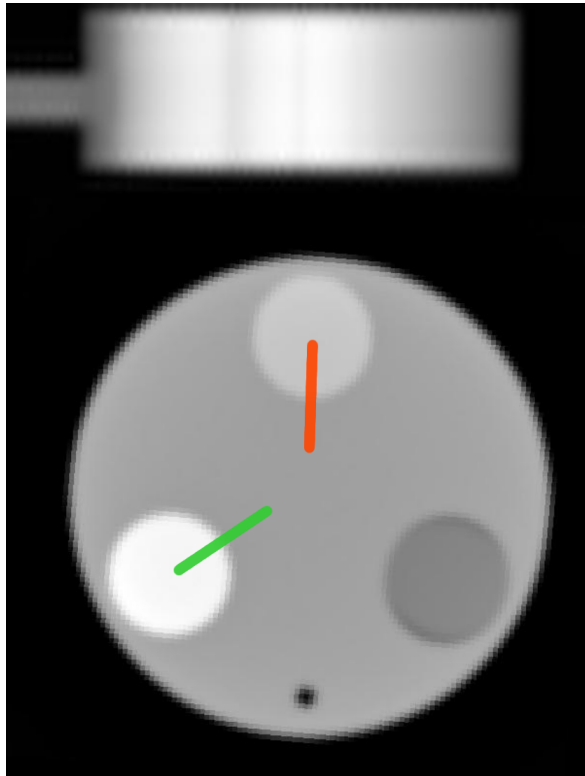
(a) Siemens Biograph 40 H40s.
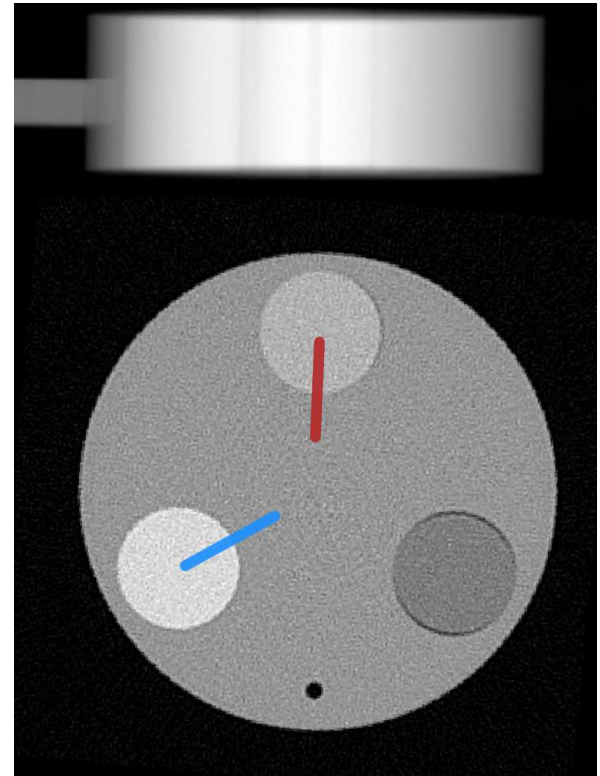
(b) Siemens Biograph 40 U90u.
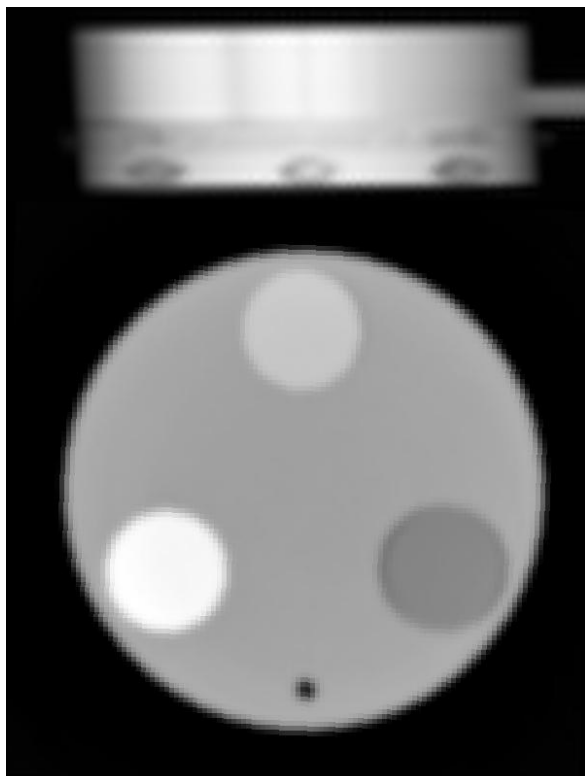
(c) Siemens Sensation Open H30s.
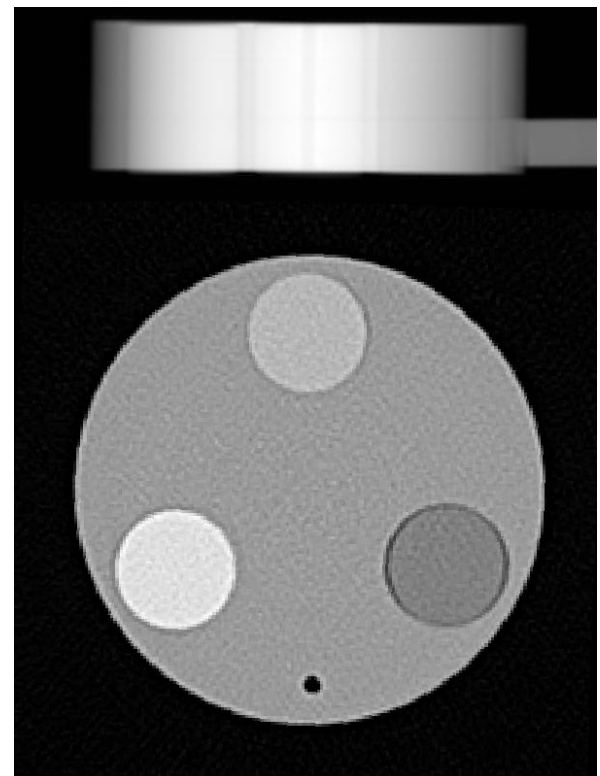
(d) Siemens Sensation Open H70h.

Figure 4.13.: Comparison of the clinical (left) and maximum quality (right) settings from the xCT scanners. The chosen profiles for the analysis of the spatial resolution at the PMMA-POM and PMMA-PVDF transitions (Fig. 4.15(a)) are marked in 4.13(a) and 4.13(b).
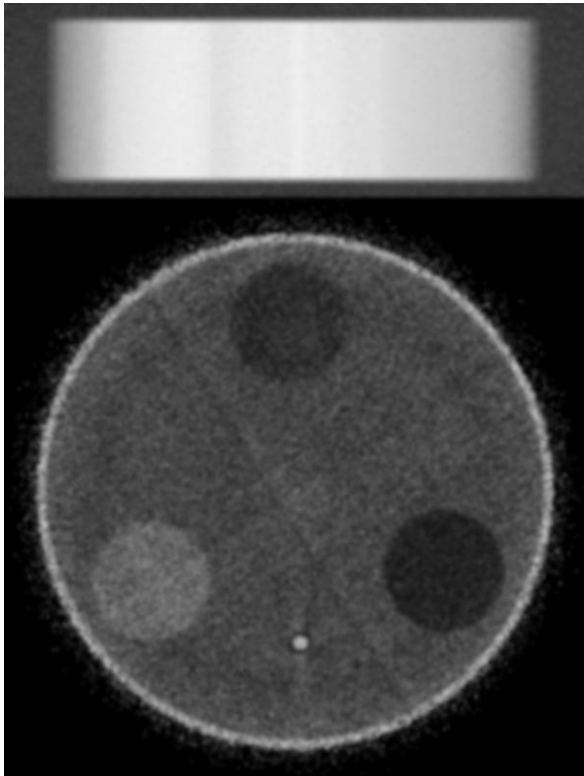
(a) PROSIT LANL x3 5e8 p$^+$.
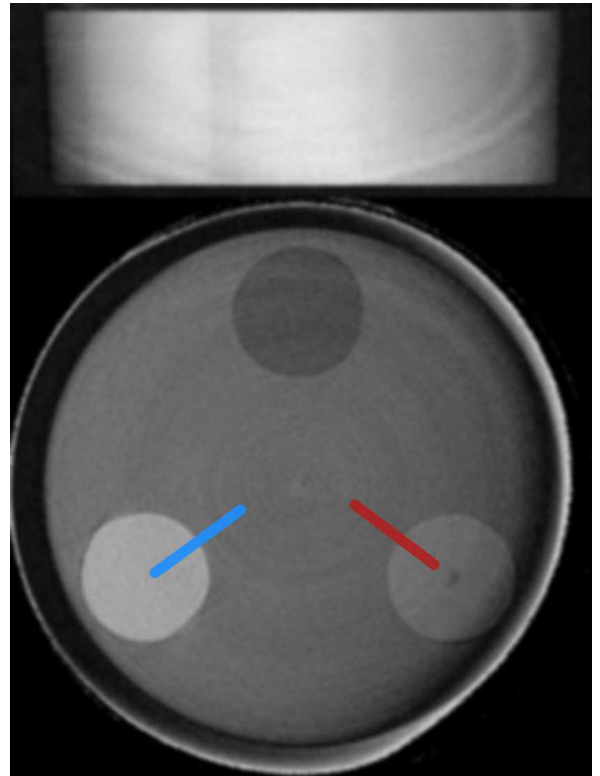
(b) pRad LANL x7 1.3e10 p$^+$.

Figure 4.14.: Comparison of the pCT PROSIT MC simulation and an actual pCT with the x7 magnifier and the x7 head phantom. The chosen profiles for the analysis of the spatial resolution of the pCT (Fig. 4.15(b)) are marked.

By comparing just the two Siemens xCT scanners it can be observed that the quality of the clinical settings (A) is very similar. This is caused by the fact that – despite a slightly different collimator in the Sensation Open machine for setting A – the general specifications of both devices are almost the same. Only in case of the high quality setting C the Biograph 40 machine has a slight advantage when it comes to the suppression of artifacts at steep density transitions. This is clearly visible at the transition between the outer PMMA structure of the phantom and the insets where – induced by the manufacturing process – a small air gap is present. E.g., the PE inset in the Biography 40 CT (bottom-right inset in Fig. 4.13(b)) has less dark borders than the one in the Sensation Open CT (bottom-right inset in Fig. 4.13(d)).

The proton simulation data was produced for a potential clinical setting with a drastically reduced proton count to compare the quality of xCT and pCT at similar dose deposition. It therefore suffers from the issue of discrete detector events already discussed in Sec. 4.2. This severely affects the noise level of the projections and correspondingly also the reconstructed CT as no additional filtering is applied. Nevertheless, the quality would still be sufficient for clinical applications as it is very similar to the clinical settings of the X-ray devices.

For a quantitative comparison of the spatial resolution performance an error function (see Eqn. 4.1) was fitted to the transition between the PMMA and the POM and PVDF insets, respectively. Intensity profiles from the Biograph 40 clinical and maximum quality settings as well

as from the pCT were then chosen, the corresponding σ serves as a measure for the spatial resolution. The discussed dark ring artifacts around some of the insets were spared during the selection process to prevent any influence due to image artifacts.

$$I(x) = a - b \cdot \mathrm{erf}\left(-\frac{x-c}{\sqrt{2}\sigma}\right) \tag{4.1}$$

The results are presented in Fig. 4.15. Whereas the clinical setting from Fig. 4.13(a) shows an average σ_{clin} of 569.4 μm, the maximum quality setting is able to achieve a remarkable σ_{max} of 160.8 μm. Nevertheless, the x7 pCT shows an even higher spatial resolution performance than the high quality xCT settings with a σ_{pCT} of 34.2 μm. Unfortunately the ring artifacts affecting the projections cause a non-flat transmission profile of the CT slices. As the projections cover 180 degrees this affects the right part of the reconstructed image. It is best visible in the first quadrant where a visual decrease of the transmission can be observed towards the edge of the phantom. The ring artifact issue is discussed further in Sec. 4.8.3.
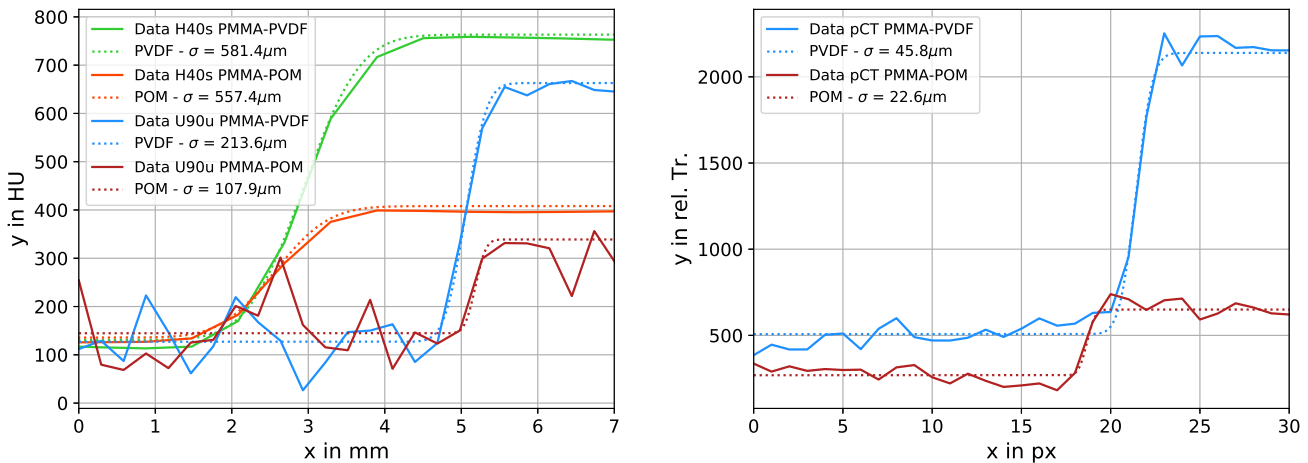
(a) Error function Eqn. 4.1 fitted to the xCT data from Fig. 4.13(a) and 4.13(b).

(b) Error function fitted to the pCT data (Fig. 4.14(b)).

Figure 4.15.: Comparison of the spatial resolution performance of the different imaging methods.

4.6 Density reconstruction and treatment planning

In order to verify the suitability of high energy proton imaging for medical purposes, all of the experiments described in the sections 4.3-4.5 using the head phantom are evaluated regarding the quality of the density or WEPL reconstruction. The tissue equivalent insets are neglected in this chapter mainly because capturing a full pCT with those was not possible but also due to structural problems with this type of material (see Sec. 4.8.4). For the PROSIT simulation (Fig. 4.14(a)), first the required material parameters (nuclear collision length and radiation length) are calculated using the tool GSI ATIMA. The material densities are already summarized

in Tab.3.5, the mass ratios are derived from the chemical compositions.

PE - C_2H_4
Mass ratio: 14.37 % H, 85.63 % C
nucl. collision length = 0.6305 m, rad. length = 0.5031 m

PMMA - $C_5H_8O_2$
Mass ratio: 8.05 % H, 59.99 % C, 31.96 % O
nucl. collision length = 0.4879 m, rad. length = 0.3407 m

POM - CH_2O
Mass ratio: 6.71 % H, 40.00 % C, 53.29 % O
nucl. collision length = 0.4125 m, rad. length = 0.2699 m

PVDF - $C_2H_2F_2$
Mass ratio: 3.15 % H, 37.53 % C, 59.32 % F
nucl. collision length = 0.3506 m, rad. length = 0.2081 m

The result of the WEPL reconstruction is then plotted in Fig. 4.16. The leftmost bar represents the theoretical value of the WEPL calculated using the literature values (see Tab. 3.5) and Eqn. 2.9. These values may already contain an unknown uncertainty as the plastic materials were bought without a material certificate. The exact parameters are therefore unknown, a measurement of the stopping power was not possible within the scope of this work. Currently, proton radiography is only capable of reconstructing the material density, the material stopping power mandatory for the WEPL calculation remains unknown. The missing information for the calculation was taken from literature, a possible method of measuring also the stopping power is discussed in Sec. 5.5.

Comparing all results it becomes obvious that close to the density of water in case of the polyethelene and polymethylmethacrylate all different techniques deliver a good result. The fact that the assumed WEPL of the PMMA is slightly too low for all methods can be attributed to the tomographic reconstruction procedure which produces – under certain circumstances – a curved density profile for the CT slices (see Sec. 4.3.1). This mostly affects the PMMA measurement as data points are taken from the center and from side regions of the phantom and then averaged. At higher densities the accuracy changes drastically, here the conventional HLUT method is less accurate since less data points are available in this region. This will especially affect the treatment of head tumors where high density bone of the skull has to be traversed by the therapeutic ions to access the tumor volume. Proton radiography delivers a significantly better overall result when it comes to density reconstruction. Using xCT data as base data is in many cases sufficient for most medical purposes. However, calibrating these data with actual patient data from ion imaging rather than using a static lookup table could boost the accuracy of future treatment planning. Full proton CT also delivers good results but struggles to keep up with the image quality of xCT – not regarding the spatial resolution performance but image
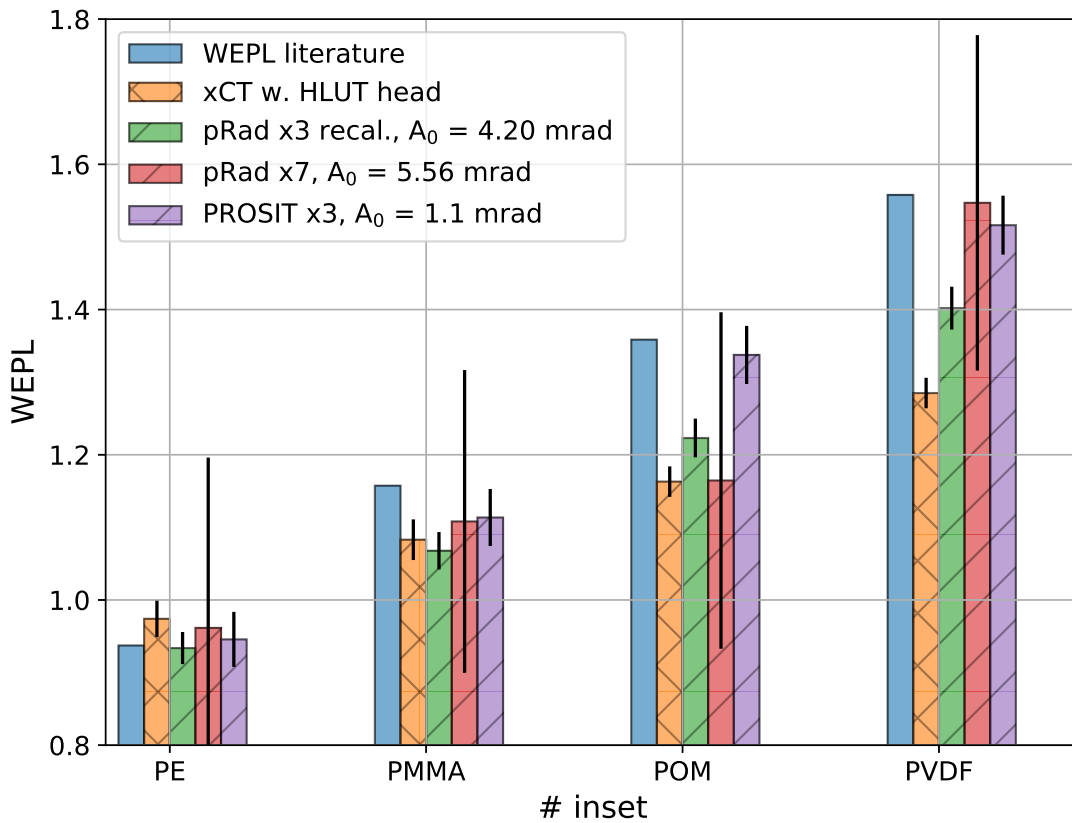
Figure 4.16.: Result of the WEPL reconstruction with different experimental methods (X-ray HLUT, X-ray p-recalibration and pCT simulation and experiment). The theoretical value was calculated using Eqn. 2.9 and the measured density and calculated stopping power from Tab. 3.5.

fluctuations which are already filtered perfectly in commercial systems (see Sec. 4.5). This leads to the huge error bars visible in the evaluation. Nevertheless, applying those filtering methods also to pCT would certainly improve the output and deliver a better result close to that of the simulation.

For an estimation of the effect of the different density reconstruction on actual patient treatment planning further studies were performed with the xCT HLUT, the recalibrated xCT and the pCT dataset. The clinically obtained xCT dataset relying on the conventional HLUT was used as the base data as it reflects the current state of the art technique. Investigations on the provided HLUT from the HIT did already reveal a severe discrepancy between the actual WEPL and the HLUT data independent from the used scanner/protocol as shown in Fig. 4.17. It has to be noted that the biggest differences occur at large HU and therefore large WEPL. The region of soft tissue close to a HU of 0 does still show an offset but a significantly better agreement with the theoretical data.

For treatment planning the TRiP98-64 treatment planning software [84, 85] V1201 was used simulating a proton beam at the HIT; further information on the used software can be found in the appendix A.2. Two different scenarios have been considered to describe the effect of the
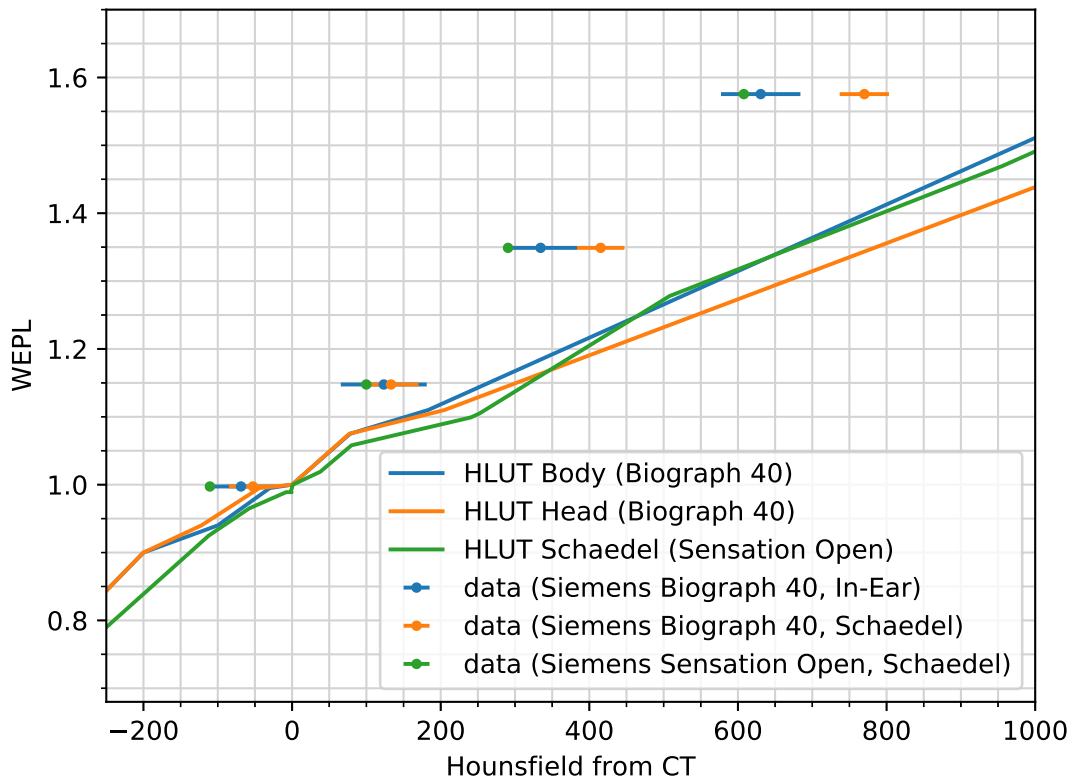
Figure 4.17.: Clinical HLUTs from the two xCT scanners Biograph 40 and Sensation Open using different protocols. The theoretical WEPL of the used plastics is plotted along with the HLUTs showing a good agreement at tissue densities but a rather large discrepancy towards large densities.

observed differences in density reconstruction on the current clinical procedures. The plan was first calculated using the conventional clinical approach with the Biograph 40 xCT base data and the corresponding *Schaedel* HLUT and then applied to the recalibrated xCT and the pCT to illustrate potential differences. As TRiP currently does not use direct WEPL CTs this requires a forward/backward transformation of the values with an identity HU table in case of the pCT. All initial treatment plans were optimized on a $3{\times}3\,\mathrm{mm}^3$ raster in the x-y-plane and a $2\,\mathrm{mm}$ spacing in z-direction, the target dose was $2\,\mathrm{Gy}$. The irradiation was performed from the left side as the Newton's ring artifacts cause declining WEPL values at the right side of the pCT as well as concentric ring artifacts in the upper part of the respective slice which would severely falsify the results. In general, irradiating calculated plans in the pCT is a challenging task as the geometry is slightly different. The size of the x7 phantom was scaled up and the target was rotated to obtain the best possible result.

The first plan is calculated on a soft tissue scenario, the tumor – a virtual cylindric volume of interest (VOI) which is about the size of the insets – is sitting in PMMA between the PVDF and POM insets. The corresponding treatment plan was calculated so that only the PE inset had to be traversed. The result is plotted in Fig. 4.18 for the initial plan and the irradiation of the field into the other base data. Corresponding to the depth of the tumor of $28.1\,\mathrm{mm}$, the treatment

plan consists of 13 energy slices in z-direction with a range from 72.87 MeV up to 93.02 MeV. Note, that the darkest contour in red corresponding to 1.9 Gy or 95 % of the target dose is larger than the actual VOI framed in white. This is caused by the safety margins and due to the fact that the phantom as well as the VOI is very small compared to typical clinical scenarios. The pCT in Fig. 4.18 (bottom right) can be seen as a proof of concept as the discussed concentric ring artifacts already cause a shift of the right part of the field and lead to a non-optimal dose deposition.
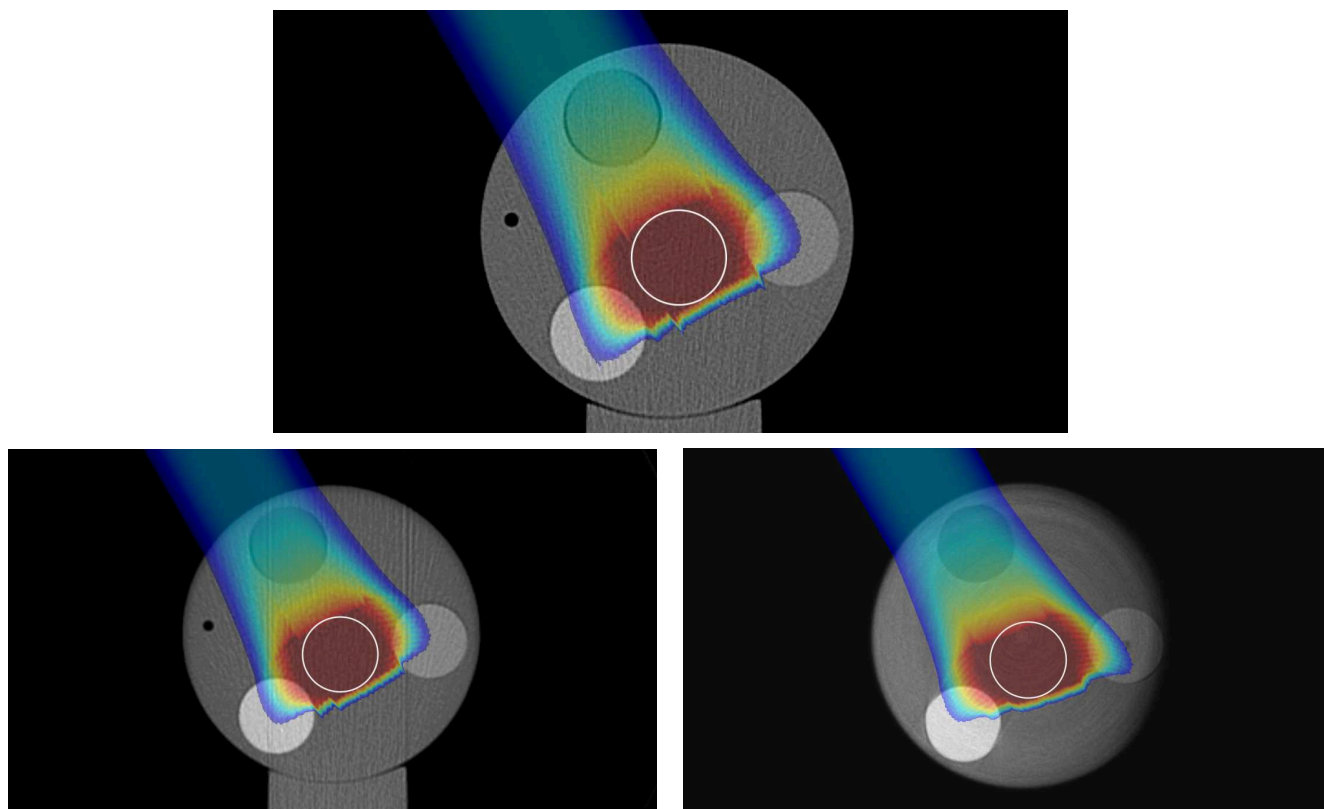
Figure 4.18.: Field from the treatment plan in soft tissue using xCT base data from the Biograph 40 scanner and a clinical HLUT (top). The field was irradiated in the recalibrated xCT (bottom left) and the pCT (bottom right) in order to demonstrate the shift of the dose distribution when using more accurate data. The actual target dose distribution is larger than the VOI (white circle) not only due to the safety margins but also due to the fact that the target is rather small considering the width of a typical proton pencil beam.

Another scenario was simulated with a target VOI located again in PMMA between the PE and POM insets, simultaneously an OAR was introduced in the POM inset (highlighted in red). The irradiation was performed from the lower left side through the PVDF inset which serves as a bone obstacle. This is a common scenario e.g. for head tumors where both, the skull and the vulnerable brain stem, have to be considered in the treatment planning. Corresponding to a tumor depth of 40.7 mm, the treatment plan now spans an energy range from 81.75 MeV up to 100.46 MeV. The results are shown in Fig. 4.19, in this case severe differences of the dose

distributions can be observed. The lower part of the dose distribution close to the fictional OAR is the most affected one due to the significant WEPL reconstruction results for the PVDF inset. For this inset, the WEPL difference between the conventional HLUT and the recalibration attempt is 8.5 %, in case of the pCT, which is closest to the literature value, the difference increases to 17 %. Therefore, an upstream shift of this part of the dose distribution can be observed which even causes cold spots with considerably less dose on the tumor volume in case of the pCT.
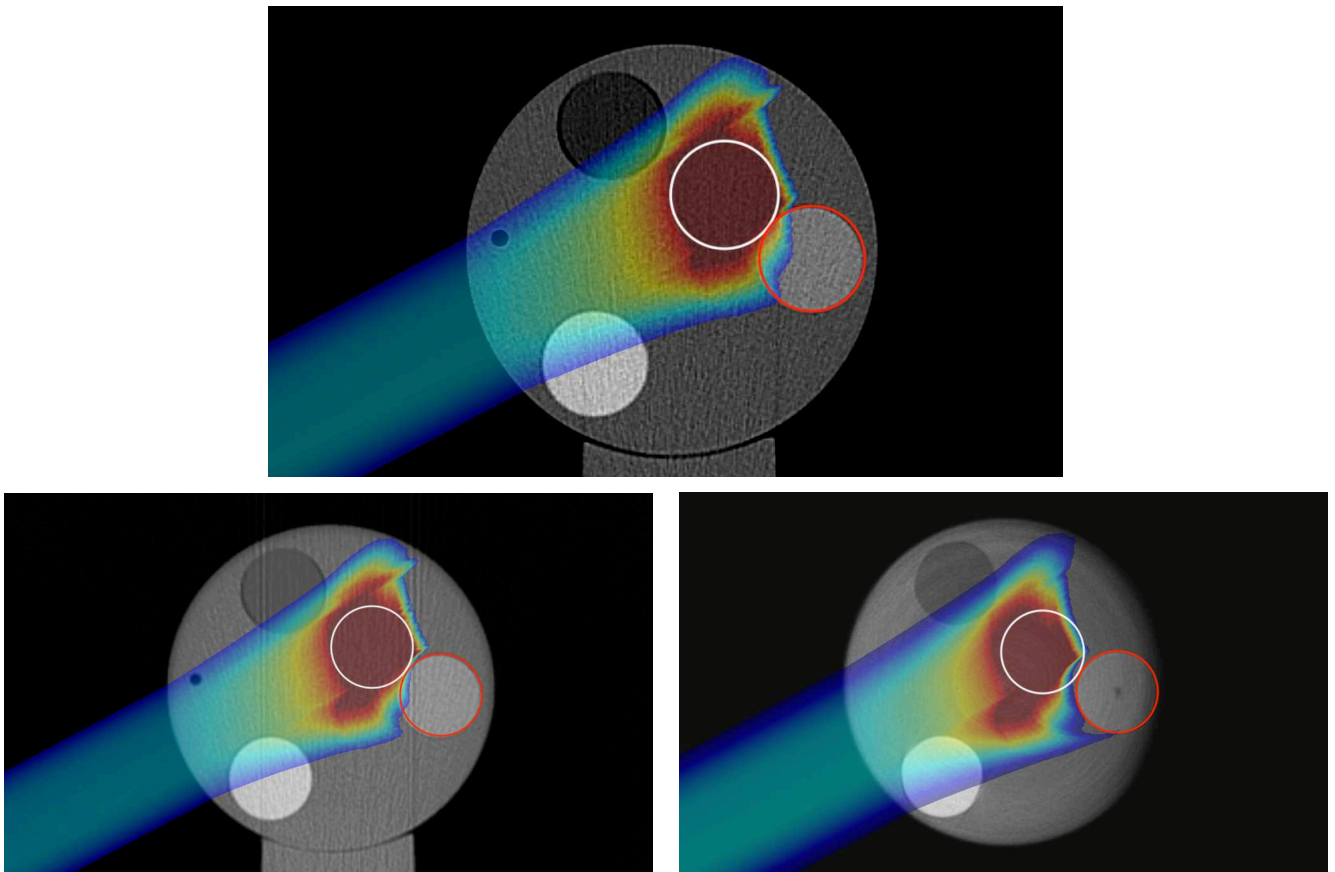
Figure 4.19.: Fields from the treatment plan mimicking an outer bone structure and an OAR using a clinical HLUT (top) irradiated in the recalibrated xCT (bottom left) and the pCT (bottom right). The VOI and the OAR are highlighted in white and red, respectively.

The two presented scenarios indicate the issues of the conventional clinical HLUT especially at large WEPL, where less data points contribute to the unit conversion. A more quantitative comparison between the different treatment plans for the two scenarios is given by the Dose-Volume histograms (DVHs) presented in Fig. 4.20. For the soft tissue scenario (left) almost no difference between the conventional method and the recalibration attempt is visible. Our pCT delivers a worse result here, mostly due to the discussed issues. In case of the second scenario including an OAR a significant difference can be observed leading – in case of the pCT – to cold dose spots on the tumor volume. This could, in the worst case scenario, cause a recidivism of the cancer after the treatment procedure.

Due to the geometrical issues and known image artifacts the pCT data may be considered as a proof of concept of the feasibility of using pCT for treatment planning but it should not serve as an example of the achievable accuracy. For a reliable quantitative statement regarding the accuracy of high energy pCT a pCT of the original x1 phantom would be required.
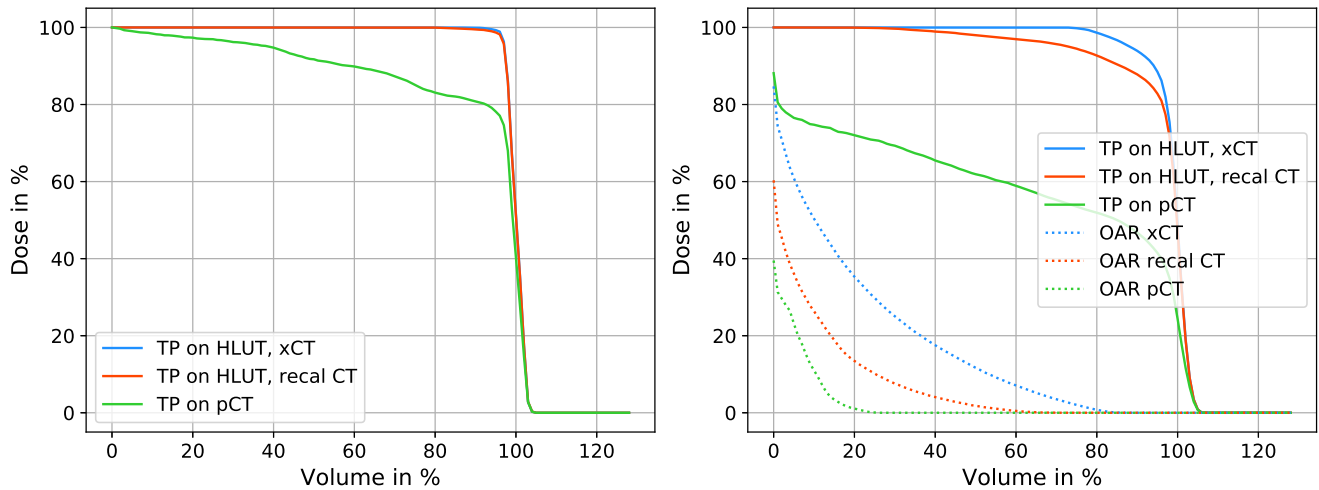
Figure 4.20.: Dose-Volume histograms of the soft tissue scenario (left) and of the OAR scenario (right) for treatment planning with xCT and HLUT, the recalibrated xCT and the pCT.

4.7 Dosimetric measurements

Dosimetric measurements were performed with the clinical phantoms during the experiments with the x1 identity lens and the x3em magnifier as well as with different X-ray CT machines at the university clinic in Heidelberg. The technical details of the measurement are described in Sec. 3.5, the arrangement of the TLDs on two grids facilitates the position dependent dose analysis. As an example the dose maps for the TLD sets C, used during the x3em measurements, and E, for the x1 run, are presented. Induced by the method for capturing the radiographs (Sec. 4.11(b)) we expect a centered, broadened dose channel for set C caused by the overlap of three beam spots in the left, center and right positions (top, center, bottom for the top view in the dose maps). This is confirmed by the dose maps in Fig. 4.21, also the intensity is lower by a factor of 4 in the top layer of TLDs which is obvious as they are situated farther away from the beam axis. In case of the x1 setup the beam is more broadened, the center of gravity of the proton distribution was situated more to the right of the target. This is also confirmed by the dosimetry, in the corresponding dose maps (Fig. 4.21) we can observe a lower intensity compared to the x3em data and a shift of the distribution to the right.

The average dose to the phantom has been calculated by first averaging all of the TLDs of one set, then the result has been normalized to the dose per shot. For the measurements with the x3em magnifier we assume $6.4 \cdot 10^9$ protons per pulse equaling $1.92 \cdot 10^{10}$ protons per image

(three beam positions). As no stitching is required in case of the x1 data only one pulse per image is needed leading to $6.4 \cdot 10^9$ protons per image in that case.
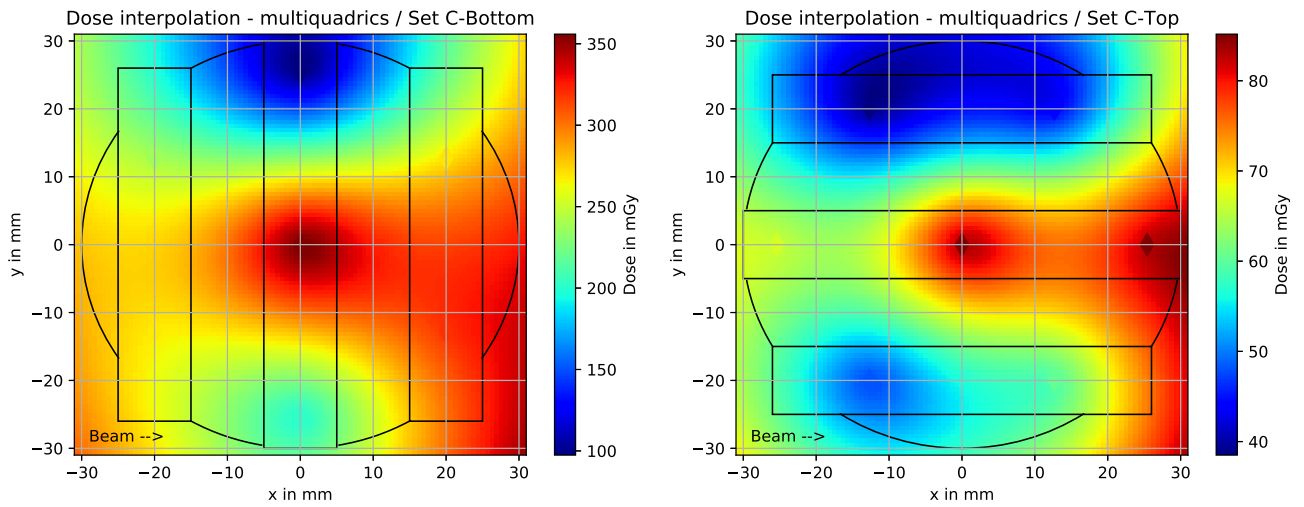
(a) x3em bottom set C.

(b) x3em top set C.
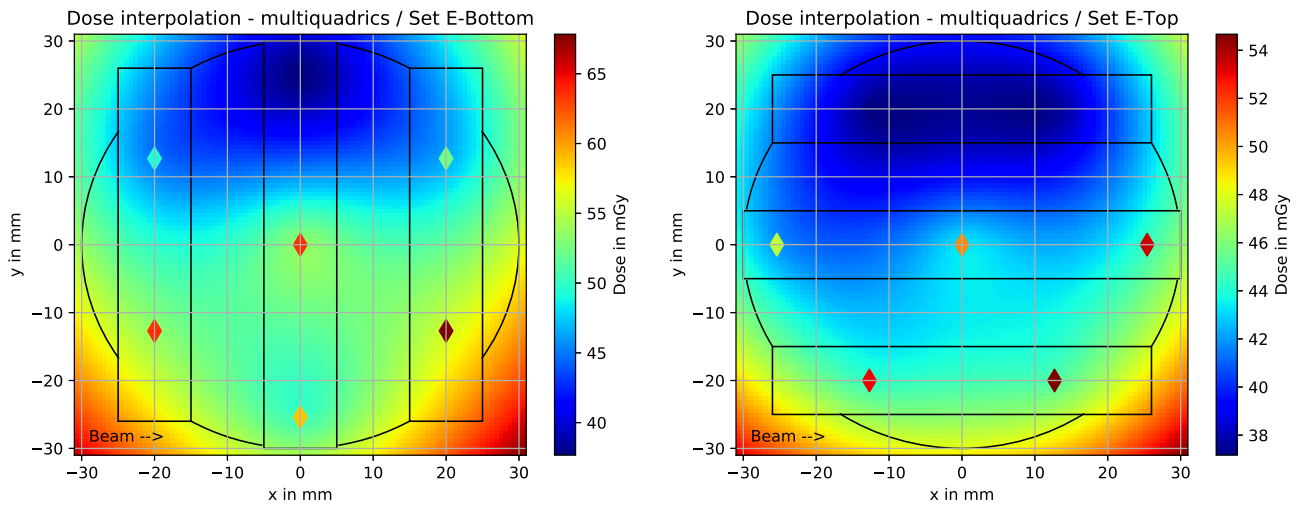
(c) x1 bottom set E.

(d) x1 top set E.

Figure 4.21.: Dose maps captured with the x3em and x1 lenses. For each map 7 data points are available corresponding to the distribution of the TLDs shown in Fig. 3.6(b). The full map was then interpolated using the radial basis function interpolation package of *scipy* for *Python*.

In case of the X-ray measurements the dosimetry has always been performed using the 'clinical' setting described in Sec. 4.3. Configurations with a smaller slice thickness, higher tube voltages and higher tube currents are used seldom as they do increase the dose given to the patient. The X-ray results reflect the dose for a full CT.

The proton data confirms the linear dose scaling, the factor of three between the proton count of the x1 data and the one of the x3em data can also be observed in the dose values. Nevertheless, the dose measured for a single proton projection is at the same order of magnitude

as the one for a full xCT. For clinical purposes, especially for pCT, which requires at least 60 projections for achieving a decent image quality, a considerably lower dose delivery would be required leading to a mandatory reduction of the proton flux. Due to restrictions regarding the used beam pattern it was not possible to perform dosimetry with lower statistics during the **SEP16** and **OCT16** beam times.

Setup	x3em			x1			full xCT		
Set	A	B	C	D	E	F	G	H	X
p_+ count $\times 10^9$	19.2	19.2	19.2	6.4	6.4	6.4	-	-	-
avg. dose in mGy	146.27	154.58	155.62	51.92	51.93	51.97	75.64	83.07	84.50

Table 4.3.: Averaged dose normalized to a single image.

4.8 Investigations on error sources

During the course of the 4 beam times with different experimental settings and setups it became obvious that the initial goal of a density resolution below the 1 % threshold is difficult to achieve since many factors contribute to the overall error of the measurement. This starts with the stability of the accelerator itself which cannot be influenced and may – in the case of LANL due to the age of the machine – even vary from day to day depending on factors like air humidity and temperature. Whereas the ion optics are pretty well understood and can be adjusted precisely, the detector setup consisting of the scintillator and camera setup is the second prominent source of errors. In the following subsections several of the occurred issues are discussed and evaluated regarding their quantitative influence on the final result.

4.8.1 Beam instabilities

Although plenty of tuning measurements prior to the actual experiments were conducted, the beam profile showed an unstable behavior during most of the beam times. This was investigated by considering just the beam pictures from each beam time and fitting a two dimensional Gaussian to those profiles. This does not consider any distortion of the beam profiles itself but it shows the spatial fluctuation of the beam in the detector plane and gives a rough estimate on the stability of the accelerator during the respective run. From the fit only the center position of the beam was considered and then plotted as a deviation from the average position of the beam during the respective cycle (see Fig. 4.22).

The most stable operation was achieved during the first beam time in September 2016 where the position of the beam varies less than ±0.5 mm from the average beam position. During all of the other beam times we can observe fluctuations of up to 2.0 mm which severely affect the accuracy of the flattening. An interesting behavior can be observed for the pco.dimax/**NOV16**
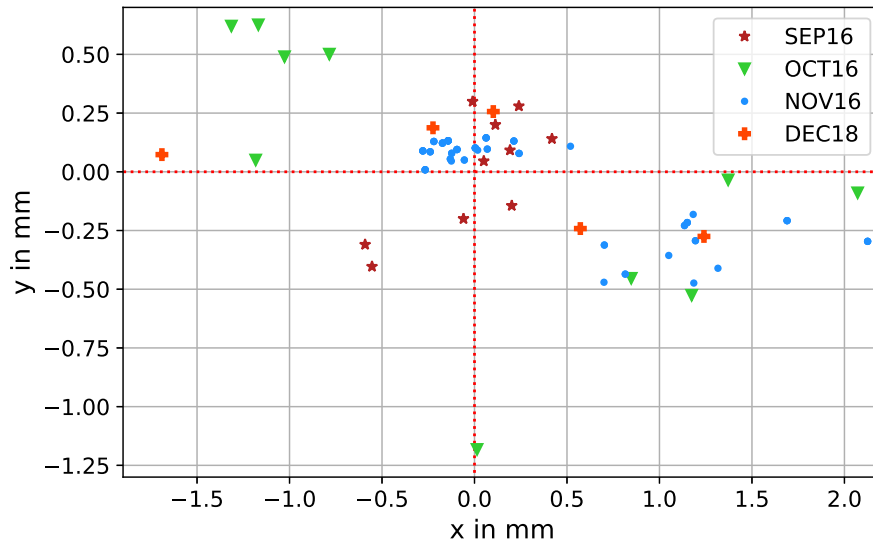
Figure 4.22.: Position of the different beam spots relative to the average position for the respective beam time.

beam time where the central positions of the beam spots seem to be scattered over two separate areas. This is the case although the accelerator settings did not change during the 4 days of beam time and indicates that theoretically also a shift of the initial angular spread of the beam prior to the diffuser might have occurred. Thus fitting and averaging the initial θ_0 for the pco.dimax/**NOV16** data presented in Sec. 4.1 and 4.2 could introduce an additional unknown error. However, the two different areas cannot be attributed to a series of measurement with a single collimator, it seems like the accelerator is switching between different states within a cycle without any obvious cause. Therefore, the impact of this behavior cannot be quantified, it is not considered in the results presented in the discussed sections.
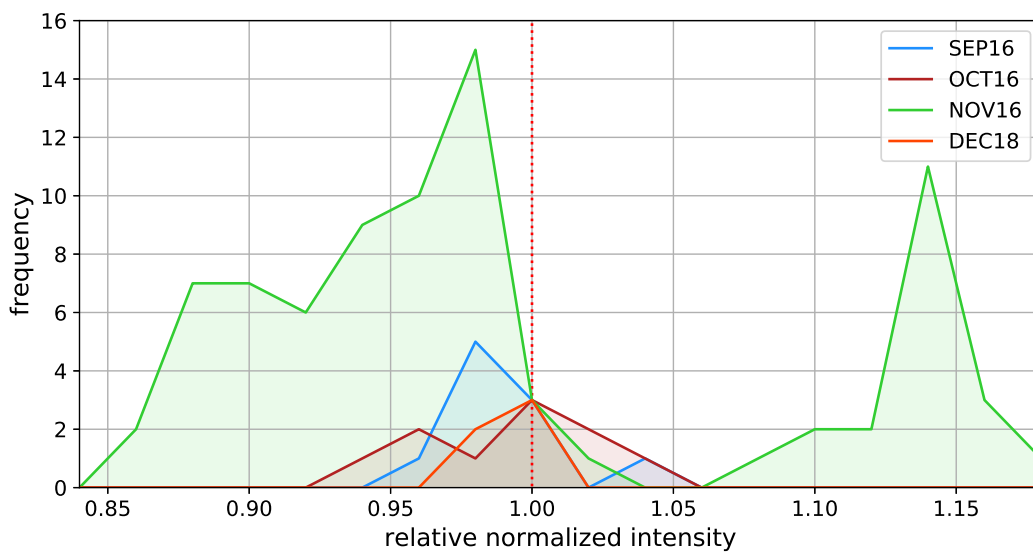
Figure 4.23.: Relative beam intensity of the respective beam times.

In addition to the spatial instability and the neglected distortion of the profile also the intensity of the beam profile varies, typically around 5 % but in extreme cases such as the **NOV16** beam time up to 15 % and more. Just as it was the case with the beam spot positions this beam time shows two different intensity distributions above and below the average intensity but again, the different distributions cannot be assigned to a test series with a collimator supporting the previous statement. This effect in general also affects the quality of the flattening procedure and is even harder to compensate for. Due to the reduced intensity in the target image it is impossible to correlate both quantities and to perform an intensity correction. The intensity fluctuation is mostly caused by the chopper described in Sec. 3.1.1 causing an deviation of the number of particles reaching the detector from shot to shot.

4.8.2 CDS on the pco.dimax

Correlated double sampling, or CDS, is a feature of the used pco.dimax camera which is supposed to assist with the *dark field* handling of captured images. The camera constantly monitors the pixel values in between the actual frames and subtracts an average of those from the final images. A detailed analysis of this feature using different inter-frame times was performed with the lens cap mounted revealing a severe dependence of this method on the chosen frame spacing. With the cap mounted the captured image should show no counts at all, this however, is not the case as plotted in Fig. 4.24(a). The produced image is neither empty nor is it flat. In order to investigate the influence of this behavior on the **NOV16** data, an analysis of a stack of 20 *dark field* images with the lens cap mounted and a 1 s inter-frame time was performed. The corresponding actual dataset was also captured with a 1 Hz repetition rate. The result is plotted in Fig. 4.24(b) for a border region with a width of 200 px as well as for the center region excluding the border to consider also the non-flat shape of the image. The analysis shows that the automated subtraction algorithm clearly fails to always correct the first image of a sequence making this frame unusable for analysis. After this frame the average pixel value decreases with a slight oscillation. No clear dependence on the area of the selection can be found in the 1 Hz dataset.

During the **NOV16** beam time no separate *dark fields* without the lens cap mounted were captured as the CDS was assumed to work properly at that time. Therefore, it is difficult to predict the influence of the CDS at all. By analyzing the intensity of the *white fields* captured during the beam time it can be observed that the first image of each stack shows a decreased intensity level by around 10 % which can be attributed to the issue described above caused by CDS. The first frame is therefore always skipped during the data analysis. The overall quantitative influence of CDS remains to be unknown, due to the feature being hard-coded in the firmware of the camera it was furthermore not possible to disable it.

The extended analysis of the CDS also revealed another bug in the firmware of the pco.dimax camera. The last frame of each stack of images is never saved but instead replaced by a duplicate of the second to last frame. This is independent of the number of images in a stack and can e.g. be seen in Fig. 4.24(b) where the pixel values of both of the last frames are absolutely identical.
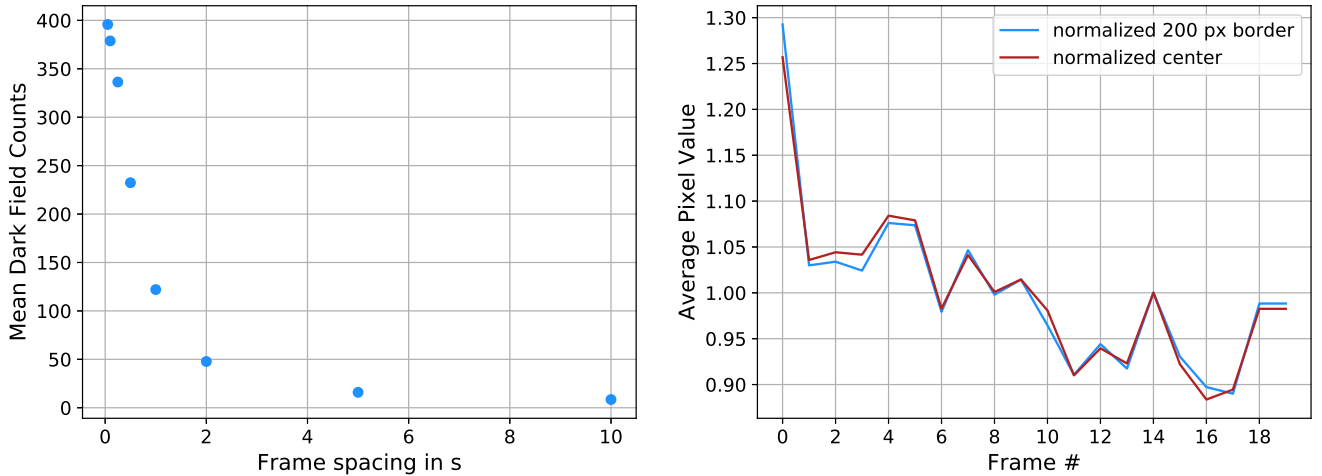
(a) Mean *dark field* counts depending on the inter-frame time.

(b) Normalized average *dark field* value for 1 Hz image capture.

Figure 4.24.: Analysis of the CDS behavior of the pco.dimax camera.

4.8.3 Newton's rings

Newton's ring artifacts usually occur in optical lens systems where a small gap between two single lenses with a different curvature is not filled with another medium. At the transition between the lens surface and air total reflection can happen, the interference of the reflected rays may then cause either constructive or destructive interference if the gap equals $n \cdot \lambda/2$. As lenses are usually axially symmetric, this causes either dark or light ring artifacts on the image.

Newton's ring artifacts occurred in the HiSense data from the **DEC18** beam time caused by the poor quality lens of the HiSense camera. For a detailed analysis the *white field* images were considered. By fitting a two dimensional Gaussian to the beam (see also Sec. 4.8.1) the image itself can be flattened leaving only the artifacts for analysis. One of the flattened beam pictures is shown in Fig. 4.25(a). It is not completely flat as the shape of the beam does not necessarily coincide with a Gaussian, however, the ring artifacts are now visible but they are not axially symmetric. The image was converted into polar coordinates and an analysis of the 4th quadrant was performed where two dark rings are visible. The center of the coordinate system was assumed to be the center of gravity of the beam. Averaging the polar image over 90 degrees in this quadrant we can clearly observe the effect of the dark rings. The averaged profile is plotted in Fig. 4.25(b), for a better visualization the profile is flattened in a second step by fitting a spline with the order of k=3. This leaves only the dark ring artifacts which are on the order of 1-2 % transmission.

Correcting the ring artifacts is extremely challenging as they are not symmetric and equally distributed over the image. Furthermore, they have to be filtered before flattening, otherwise the division of two separate images with irregular artifacts would create a new, even more complicated irregular artifact pattern on the final image. This is even more challenging in case of the target images because the transmission profile of the object is overlapping the beam
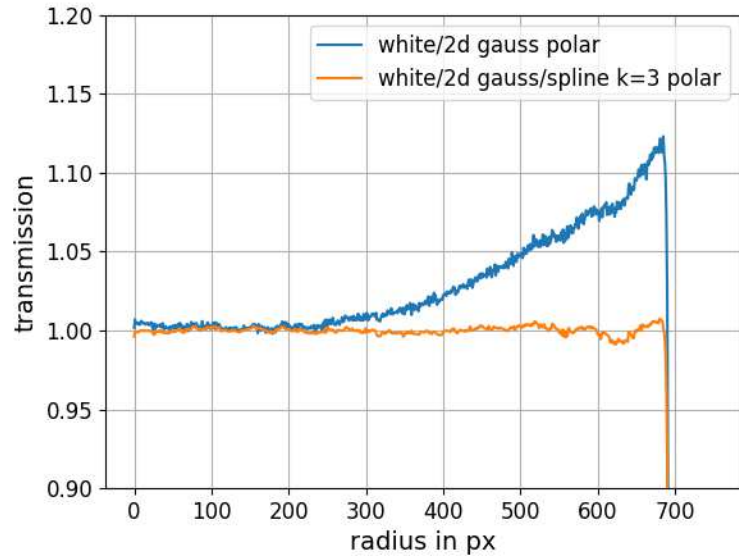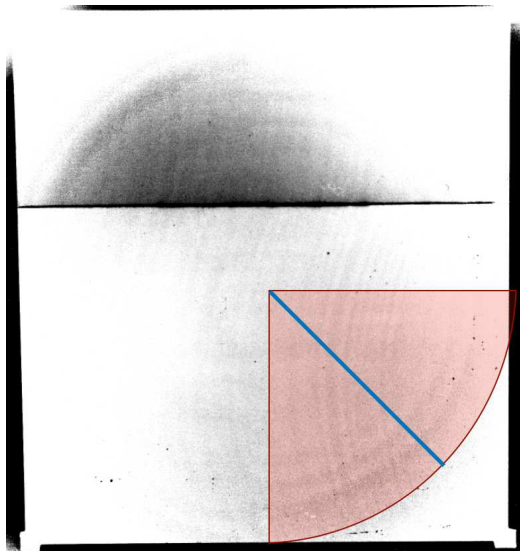
(a) Flattened beam picture of the x7 magnifier.

(b) Average profile of the 4th quadrant of the flattened beam picture in polar coordinates.

Figure 4.25.: Result of the Newton's ring analysis of the x7/HiSense data.

profile complicating the above described method for flattening by fitting a Gaussian. Therefore, the ring artifacts were neglected for the final analysis as for future experiments a suppression by changing the responsible components of the lens system during the experiment itself is less complicated than the development of a filtering algorithm.

4.8.4 Aging effects of TE plastics

Within the scope of the head phantom experiments also a set of tissue equivalent plastic insets was available and imaged during the **SEP16** and **OCT16** beam times. The insets were provided by the external manufacturer QRM and are manufactured from a plastic resin with similar atomic properties as water (see Sec. 3.4.2). Before hardening it is possible to add air bubbles with a diameter of 30-70 μm to decrease the density of the resin. This was done in case of 5 of the 6 insets to obtain density differences from 0.36 % up to 7.56 %. Measurements conducted in December 2016 confirmed the densities specified in the QRM data sheet within a predicted error range of ± 0.5 %. Note that the specified error in density in the data sheet is already larger than the smallest difference in density that was mimicked by adding bubbles to the insets.

A second measurement at the beginning of 2019 revealed a severe shrinking of the insets. The insets containing air bubbles shrinked on average by 1.9 %, the base resin shrinked by 1.0 %. Simultaneously, the mass of the insets also decreased leading to a similar overall density as before. As the structure of the plastic is still stable and no mechanical damage was observed the loss must have occurred by outgasing of liquid components in the insets. The effect of this process on the stopping power of the material is unknown as no particle range measurements

were performed. Due to the possible uncertainties caused by the effect the evaluation of the tissue equivalent targets is not presented in this work.

date		Inset 0	Inset 1	Inset 2	Inset 3	Inset 4	Inset 5
31.08.16	density in g/cm^3	**1.083**	**1.079**	**1.062**	**1.048**	**1.030**	**1.007**
19.12.16	diameter in mm	14.80	14.85	14.80	14.85	14.90	14.85
	height in mm	29.70	29.70	29.65	29.70	29.70	29.75
	volume in cm^3	5.109	5.144	5.101	5.144	5.179	5.153
	mass in g	5.553	5.561	5.441	5.377	5.323	5.197
	density in g/cm^3	**1.087**	**1.081**	**1.067**	**1.045**	**1.028**	**1.009**
01.02.19	diameter in mm	14.75	14.75	14.75	14.75	14.80	14.75
	height in mm	29.60	29.50	29.45	29.50	29.50	29.50
	volume in cm^3	5.059	5.041	5.032	5.041	5.075	5.041
	mass in g	5.465	5.425	5.346	5.294	5.220	5.079
	density in g/cm^3	**1.081**	**1.076**	**1.062**	**1.050**	**1.029**	**1.008**

Table 4.4.: Bulk density measurement results of the TE insets provided by QRM conducted at the beginning and end of the project.

5 Discussion

The performed studies have shown that high energy proton radiography using high energy protons in the GeV range is capable of satisfying the needs of medical imaging regarding image quality and density reconstruction. The current image processing and preparation procedures require lots of manual interaction with the data, mostly caused by the instable behavior of the accelerator and detector system. By eliminating those, a future clinical application could be fully automated. In order to rank the presented findings in the entire field of medical imaging, the results are compared to other techniques currently under development. Furthermore, several technological possibilities but also challenges for an actual implementation are discussed.

5.1 Biomedical applications of high energy proton radiography

With respect to the results presented in this work, several applications in the medical imaging sector are conceivable exploiting the advantages of high energy proton radiography.

Proton Computed Tomography
Just as in the single proton tracking approach from Sec. 2.3.2, high energy proton radiography can be used for computed tomography. First attempts have already been made [3] and the feasibility of treatment planning has been presented in this work, however, several technical challenges of this technique remain unsolved. Those issues regarding the patient or beam rotation are discussed in detail in Sec. 5.4.

IGSpRS - Image guided stereotactic proton radiosurgery
Increasing the energy of protons leads to an extended range of those particles, e.g., in water, the residual range of protons with a kinetic energy of 800 MeV is around 2.37 m. This prohibits the use of conventional approaches exploiting the Bragg peak for particle therapy as described in Sec. 2.1. Instead, higher particle energies will lead to a decreased scattering and therefore to a smaller blow-up of the spatial beam distribution. Those benefits could be utilized by firing high energetic beams from several directions at the tumor volume, which could enable the treatment of extremely small tumors on the mm-scale. Although the dose deposition of high energy ions is nearly constant over the whole target range, a multi-field crossfiring plan would still produce a dose distribution concentrated at the intersection volume of several different beams [86]. This procedure would then be similar to conventional X-ray therapy where multi-field plans are commonly used. Choosing suitable entrance and exit channels could still allow for a sparing of OAR. The beam exiting the patient can furthermore be used for proton radiography allowing an immediate position verification either via density reconstruction or – in case of a broadened beam

– even via feature recognition. A facility employing this technique has already been proposed by scientists at the LANL [87].

5.2 High energy proton radiography vs. other techniques

Currently, the most prominent contestants for future medical imaging alongside high energy proton radiography are single tracking pCT and DECT. DECT is already clinically available and proved to deliver good results for treatment planning (see Sec. 2.2.4), however, the capability of material separation is mainly used for an improvement of the image quality. This includes a reduction of the artifacts originating in parasitic high-Z materials or simply the visualization of contrast agents used, e.g., for an analysis of the renal function or renal stones. Compared to conventional xCT it does neither offer an increased data acquisition speed nor does it improve the spatial resolution performance of a setup.

Tracking pCT offers – in contrast to the current high energy proton radiography – the possibility to simultaneously measure both the density of the sample via scattering and the stopping power employing a range telescope. As the requirements on the accelerator side are low (see Sec. 2.3.2) there's a vast amount of work groups worldwide addressing the challenges of this technique. Despite significant advancements during the last years the biggest issues of this method are still the speed of the data acquisition (especially the scattering data) as well as the size constraints of the object being investigated. Both are crucial parameters for a clinical adoption because keeping the patient steady in a certain position is even more challenging in a constricting environment which may cause stress. In terms of dose deposition and image quality tracking pCT is quite similar to conventional xCT.

Category	Parameter	Value
Accuracy	Spatial resolution	$< 1\,\mathrm{mm}$
	Electron density resolution	$< 1\,\%$
Time efficiency	Installation time	$< 10\,\mathrm{min}$
	Data acquisition time	$< 5\,\mathrm{min}$
	Reconstruction time	$< 15\,\mathrm{min}$
Reliability	Measurement stability	$1\,\%$
Safety	Maximum dose per scan	$< 50\,\mathrm{mGy}$
	Minimum distance to patient surface	$10\,\mathrm{cm}$

Table 5.1.: Design requirements for a pCT scanner (or any novel imaging technique) for clinical application. Taken from [88].

The requirements for novel pCT scanners, but technically also for any new imaging technique for clinical applications, have already been discussed at the beginning of the 2000s [88] and are still valid today as the parameters of conventional xCT, which serve as base values, have not

changed significantly since. An overview is given in Tab. 5.1. When comparing high energy proton radiography to tracking pCT the benefits of proton radiography are clearly the outstanding spatial resolution performance in the μm-range, the extremely short data acquisition time just limited by the capabilities of the accelerator as well as the generous space constraints allowing an easy placement and handling of the patient due to the long range of high energy protons in air. The crucial factors to address are the dose deposition which is still too high in case of the performed measurements but may be lowered as suggested by the performed investigations on proton flux dependent density measurements. The technical challenges of the technique are discussed further in the Sections 5.3 and 5.4.

The tracking pCT performance may increase further during the next years due to more computing power and better detector systems, however, the outlined problem of the narrow space for placing patients will remain. Summing up those findings, high energy proton radiography presents a promising alternative to current imaging techniques. Several improvements and upgrades (Sec. 5.5) will be mandatory but might become available during the next years. The unique possibility of real-time online imaging during the treatment procedure as well as the outstanding spatial resolution performance could significantly boost the accuracy of the present heavy ion therapy and makes it very useful for clinics.

5.3 Ion optical challenges

As demonstrated, the use of high energy protons for medical imaging purposes would offer several benefits for the health sector, however, the technical requirements for the application of this technique at a conventional clinical facility are comparably high.

High energy proton radiography using short proton pulses demands a specialized HEBT configuration and is – due to the required beam matching (Sec. 2.3.3) – not compatible to the present raster scanning because the fast dipoles affect the mandatory matching conditions. Raster scanning is usually practiced with pencil beams which are either weakly (de)focused or not focused at all. In case of fixed beam lines this is usually achieved using a quadrupole doublet or triplet (for decoupling x- and y-planes), for gantries the ion optical design is a lot more challenging. A common approach is to design the whole gantry as an imaging system enabling point-to-point focusing from the coupling point of the gantry to the iso-center of the gantry and to simultaneously use point-to-parallel focusing from the center of the sweeper magnets used for the scanning again to the iso-center of the gantry. The correction of chromatic aberrations affecting the beam spot shape is achieved using sextupole magnets [89]. Technically, a gantry does therefore resemble an achromatic imaging system. It is obvious that this is not compatible to proton radiography which – depending on the imaging setup – requires always converging or diverging beam envelopes [68].

Even when skipping the point-to-parallel focusing the scanning technique is not intermateable with chromatic matching. Assuming a simple fixed beam line this can be demonstrated analyzing the first order beam transport and therefore dipole matrix in the x-plane [56] reading

$$\mathbf{M}_{\text{Dipole}} = \begin{pmatrix} \cos(k \cdot L) & \frac{1}{k}\sin(k \cdot L) \\ -k\sin(k \cdot L) & \cos(k \cdot L) \end{pmatrix} \tag{5.1}$$

with $k = \sqrt{1-g} \cdot 1/r$ where L is the path length of the central trajectory, g the field gradient and r the bending radius of the trajectory [55]. A dipole element will therefore affect both, x_0 and a_0 coordinates of an initially matched beam vector leading to

$$\mathbf{M}_{\text{Dipole}} \cdot \begin{pmatrix} x_0 \\ a_0 \end{pmatrix} = \begin{pmatrix} x_0 \cos(k \cdot L) + a_0 \frac{1}{k} \sin(k \cdot L) \\ -x_0 k \sin(k \cdot L) + a_0 \cos(k \cdot L) \end{pmatrix} = \begin{pmatrix} x_f \\ a_f \end{pmatrix}. \tag{5.2}$$

With the initial assumption $a_0 = W_x \cdot x_0$ from Sec. 2.3.3 we have to prove

$$\frac{a_0}{x_0} = W_x \overset{?}{=} \frac{a_f}{x_f} = W_f. \tag{5.3}$$

Assuming of course $L, g, r \neq 0$ Eqn. 5.3 does have only discrete solutions. A continuous scanning operation with simultaneous imaging is therefore not possible but also not necessarily mandatory. It would still be feasible to perform imaging between irradiating a slice of a certain energy, e.g. for position verification.

For both approaches introduced in Sec. 5.1 further requirements on the ion optical configuration exist which have to be fulfilled to enable the use of high energy proton radiography at all. A minimum of three freely configurable quadrupoles upstream of the patient location are mandatory accepting already a x-y correlation of the FOV. The distance between the last quadrupole and the patient should furthermore be reduced to a minimum to maximize the FOV. Such a configuration is currently only available at very few medical accelerator facilities as plane decoupling is not applied everywhere leading to only a quadrupole doublet available in front of the patient. The facilities using raster-scanning with fixed beam lines mostly also have long drift distances between the sweeper magnets and the patient location which are drastically shrinking the possible field of view. An overview of the situation and possibilities at present available accelerator facilities is presented in Sec. 5.4. For an effective implementation of this imaging technique at medical facilities it has to be considered already in the design stage of the ion optical system.

5.4 Technical and mechanical challenges at current facilities

Besides the ion optical challenges of high energy proton radiography another issue are the possible dimensions of such a radiographic setup. Depending on the desired magnification the length of the setup varies, e.g. the new PRIOR-II facility (Sec. 2.5) has a fixed object-detector distance of 8.9 m. A potential facility for medical applications could be a lot shorter due to lower energies possibly around 1 GeV. Nevertheless, those energies would in turn require much higher precautions in terms of radiation safety at present facilities. For those two reasons it is improbable that such a system can be used at present medical treatment facilities, e.g. at a fixed beam nozzle.

In general it would be possible to use proton radiography in combination with heavy ion gantries. The challenging matching conditions could be established already in front of the gantry and then mapped to the patient position (point-to-point focusing). The additional size of
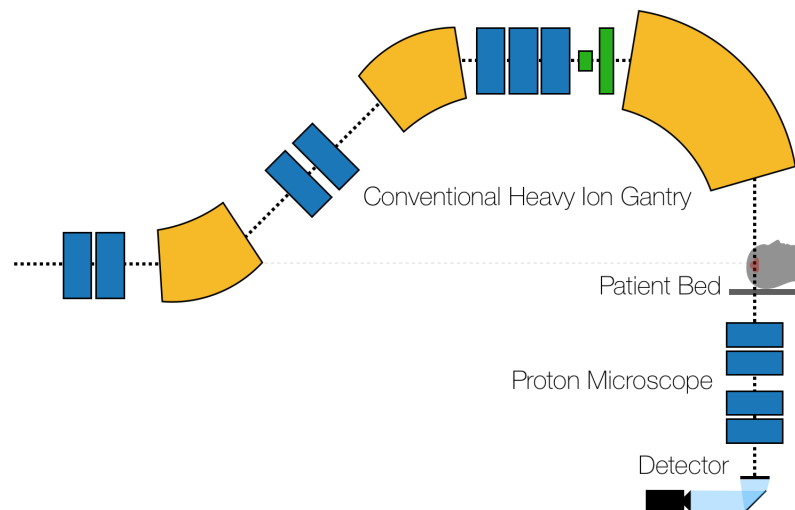
Figure 5.1.: Conceptual design of a combined assembly of a radiographic setup and a conventional heavy ion gantry.

the proton microscope makes the gantry design (e.g. Fig. 5.1) more complicated. However, as a counterweight for the beam line magnets is mandatory anyway, at least the balancing of the machine could be simplified. Due to the higher proton energies the bending magnets would have to be superconducting dipoles significantly increasing the operation costs. Furthermore, the long distance between the last focusing element of the gantry and the patient position significantly limits the available FOV as already discussed in Sec. 5.3. In such a configuration a FOV covering e.g. the dimensions of a human head (~30 cm) cannot be achieved. Additionally, the radiation safety issues which are also present at the fixed nozzle locations remain especially at a horizontal orientation of the gantry. Considering those issues, the most promising approach is using a fixed beam and rotating the patient which correspondingly limits the maximum rotation speed. Simultaneously, it is more challenging from the medical side as the most stable position of a patient is always considered to be recumbency.

With respect to the situation at present accelerator facilities, especially the problem of an extremely long drift between the last ion optical elements and the patient is present at the GSI facility [90] as well as at the spin-offs in Heidelberg (HIT) and in Marburg (MIT) [91] which operate with a maximum proton energy of just 250 MeV. The medical beam lines at the CNAO in Pavia, Italy also have a too long drift distance [92], however, at the experimental cave [93] high energy proton radiography would be possible. This also holds for the OncoRay facility in Dresden where three quadrupoles are available upstream of the target location. However, the proton energy provided by the cyclotron is even lower reaching just 230 MeV. The most promising location is the MedAustron in Wiener Neustadt, Austria, where proton spills up to 800 MeV are available. The pulse width can be as short as 100 ms with a repetition rate below 1 Hz [94]. This is still several orders of magnitude higher than the typical pulse width at current proton radiography facilities but should not affect static imaging. Furthermore, after the takeover spot for the experiment beam line a total of 5 quadrupoles would be available [95].

In general, it is difficult to find any information about the ion optical design and capabilities of clinical accelerators as most modern machines are built by manufacturers such as Varian or iba which do not provide extended technical specifications. Those machines are not foreseen to undergo changes of the ion optical system, neither in terms of a modification of the magnet parameters nor in terms of actual modifications of the ion optical configuration. Summing up the above findings it can be concluded that – due to size constraints and the need of a new form of particle therapy – proton radiography could hardly be employed at current facilities. A general proof of concept of the applicability at clinical facilities could be possible especially at the MedAustron, detailed approaches are discussed in Sec. 5.5. An extended range of experimental possibilities satisfying the constraints for medical imaging while simultaneously providing the required flexibility of the accelerator will only be available at the new PRIOR-II facility for GSI and FAIR.

5.5 Further developments and future perspectives

High energy proton radiography has proven to offer several advantages for medical imaging, however, several challenges remain which have to be solved in the near future. With the high quality imaging and the precise density reconstruction an online position verification during the treatment would already be possible, capturing high quality CTs of a small volume has also been proven to be feasible. The mandatory image processing is currently performed manually mostly due to the discussed issues regarding the stability of the accelerator performance but could be automated as partly demonstrated with the newly developed software. The stability problems, mainly being caused by the fact that the current radiographic facility at LANL is not optimized for this kind of measurements, are one of the critical issues for clinical applications in tumor therapy, e.g. treatment planning. Another challenge is the determination of the stopping power which cannot be extracted employing the present methods.

Combined stopping power measurements might become available with the introduction of time of flight (TOF) measurements currently tested at LANL employing a single pixel fast diamond detector[1]. In a first approach the timing structure of the beam was recorded behind the scintillation detector and compared to the initial timing, allowing for an estimation of the average energy loss in the target. Using pixelated diamond detectors instead this method could provide a rough spatial energy loss map and thus a stopping power map of the target. However, it has to be noted that in any case the signal propagation delay is in the order of magnitude as the measured timing resulting in rather large uncertainties. Those uncertainties will obviously increase with higher proton energies which is especially challenging for an implementation at GSI or FAIR. In addition, more than one measurement from separate angles is required for a decomposition of the stopping power map.

Future experiments on medical imaging with high energy proton radiography can be performed at the new PRIOR-II facility at GSI and FAIR (Sec. 2.5), drastically simplifying their planning and execution. Those in-house experiments will – in contrast to the LANL facility –

---

[1] Personal communication with L. Neukirch, LANL.

allow a much more flexible optimization of the setup regarding typical clinical requirements. Due to the small available FOV the attempts will be limited to either small clinical phantoms or small animal imaging, e.g. preserved mice. The experience on animal handling on site can – in the far future – also facilitate experiments with live animals.

Another recent development, the so-called *inverse collimation*, may introduce further advantages of high energy proton radiography by offering a significant boost of the image contrast in volumes with small differences in density. By cutting the angular distribution of the protons in a way that not only protons with large scattering angles, but also the ones with small scattering angles are removed, a narrow density window can be created, significantly boosting the image contrast. This would be especially useful for the differentiation of different types of tissue without the application of contrast agents. Unfortunately, this adds more complications as it would require a custom collimator for a single specific scenario. First experiments have already been performed at LANL [96] proving the suitability of this method for the visualization of low-density scenarios, e.g. the propagation of shock waves in a gaseous medium. An overview of possible future experiments at GSI/FAIR during FAIR phase 0 employing the PRIOR-II facility is presented in Tab. 5.2.

For a general demonstration of the applicability of this technique at clinical accelerators experiments at an actual clinical facility will be required, preferably at MedAustron due to the higher available energies. Also at OncoRay experiments would be possible from a technical point of view but with very limited target dimensions mostly due to the low available proton energies. In both cases PMQs would be the best choice for a proof of concept, conventional electromagnets are a lot more difficult to handle and are also considerably more expensive. The remaining non-demagnetized PMQ segments of the PRIOR-I prototype could be refurbished for this purpose, shorter lenses could be assembled from the modules to accommodate for the lower proton energies. This approach would result in a rather small available FOV but could still serve as a general demonstration of the capabilities of this type of technique.

low statistics / low dose pCT

Within the scope of this work a pCT with high proton statistics was already captured as well as the dose of single proton images was recorded. Further steps will include a pCT with lower statistics and simultaneous dose recording to compare the dose to the patient at an image quality similar to present xCT. Those experiments can be performed with suitable clinical phantoms as well as with preserved small animals for an estimation of the image quality in actual tissue. Dose measurements could be conducted using either TLDs or a suitable configuration of pinpoint ionization chambers. The GSI treatment planning software TRiP98 could then be used for a verification of the accuracy of potential treatment planning on this data.

anti-collimation for soft tissue

The presented approach for enhancing the contrast in soft tissue can be tested at the PRIOR-II facility. The ion optical theory (Sec. 2.3.3) enables the calculation of the required geometry of custom collimators suitable for imaging phantoms composed of real tissue.

IGSpRS

Just as proposed in Sec. 5.1 the feasibility of IGSpRS can be tested using a custom clinical phantom that can either be equipped with a grid of TLDs or with actual cell holders. A cross-fire treatment plan will be irradiated in both targets, verifying the dose build-up in the target volume as well as the dose delivered to surrounding areas. Simultaneously, the current beam position can be checked with the help of the density information and with feature recognition (e.g. lock on a TLD chip). The cross-fire treatment planning itself without imaging has already been used in clinics at the PNPI in St. Petersburg [97]. Besides the insights on IGSpRS, data collected with cell stacks could also provide new insights on the radio biological effectiveness (RBE) of high energetic protons, which is believed to increase due to nuclear scattering [98].

Table 5.2.: Overview of possible PaNTERA experiments at GSI/FAIR during FAIR phase 0 employing PRIOR-II.

A Appendix

A.1 Custom software overview

During the course of the project numerous software has been developed which was mandatory for image processing and data handling for treatment planning. This section is not intended to serve as a documentation but should give an overview of the purpose of the respective programs. All of the described software is part of the GSI-HHT git repository and can be accessed on an open-source basis. Next to those programs, a vast amount of simple scripts for one-time analysis of various data was developed which is not presented here.

flatten_gui.py

The *flatten_gui* tool marks the second step in data processing and allows for a correction of the initial flattening procedure with *quickpr*. It provides an advanced graphical user interface based on the *Tkinter* package and was specifically designed for handling experimental data. Flattened radiographs can be analyzed and refitted with 2D polynomials up to an order of 3 to compensate for the instabilities of the LANL beam profile. The software can also be used for stand-alone flattening of experimental data in case of a missing *white field*.

fwdct.py

fwdct is a simple tool for tomographic reconstruction of arbitrary datasets. The only requirements are, that the input data is numbered, in a .tif format and located in a separate folder. It is based on the *iradon* package inside *skimage* and supports multi-threading for speeding up the calculation of full CTs with several layers. For enhancing the image quality it contains an optional method for filtering ring artifacts, which are common in non-commercial CTs due to possible detector anomalies. Furthermore, several reconstructed slices can be averaged to reduce the noise level of the output.

hlut_gen.py

The HLUT handling tool is mostly required for the preparation of proton data for treatment planning. It can create .hlut files for TRiP98 out of HIT data as well as HLUTs can be applied to any experimental data in .tif format. This is not only needed for the general processing of xCT data but also for treatment planning on pCT data, as TRiP98 cannot handle WEPL CTs.

pcal.py

The calibration tool is needed for converting the transmission values of the proton radiography into density values. It can handle single images and stacks providing a multi-core support for

speeding up the recalibration. The transmission function (Sec. 2.3.5) cannot be inverted analytically, therefore the transmission curve is first fitted using a polynomial of the order of 5. If this solution does not meet the specified accuracy (in default mode up to 0.2 % deviation is accepted), a considerably slower binning approach is used.

pdetect.py / xdetect.py

The detection software has been specifically developed for use with the clinical head phantom in order to identify the insets and the orientation rod. A detailed description of the functionality is already given in Sec. 3.6.2. Both tools create feature files (.feat) which are required for the *trchk* tool.

pygd2.py

GDisplay files (.gd) are created as a graphical output of TRiP98. Providing an alternative to the native plotting tool *gd*, a simple program based on the *matplotlib* package for *Python* has been developed for reading and plotting .gd files. The latest version can read and visualize 2D dose maps along with an underlying CT as well as Dose-Volume histograms.

quickpr.py

The *quickpr* tool is used in the first step of the data processing. It is capable of identifying and reading different experimental data from different detector setups (Rockwell, pco.dimax and HiSense) and used for the initial data flattening. An interactive graphical output based on the *matplotlib* package is included for the determination of suitable white field images for the flattening process. Single images as well as image stacks (e.g. in case of pCT) can be processed.

revct.py

revct is – analogous to *fwdct* – a simple tool for backwards tomographic reconstruction of arbitrary CTs. It is based on the *radon* package and also supports multi-threading. It was mainly developed for the recalibration attempt where no raw X-ray transmission data could be extracted from the clinical machines. As the initial CT possibly contains not enough slices an interpolation mode is available enabling vertical stretching of the calculated projections.

stitch.py

The stitching tool was specifically designed for handling the x3em data. It is based on the *matplotlib* graphical interface, a detailed description is given in Sec. 4.3.1.

trchk.py

trchk is a semi-automatic tool for fitting the calibration curve between relative HUs and proton transmission. A detailed description is provided in Sec. 3.6.2. It requires input data from the feature detection software and produces output for the *xct2pctp* tool.

xct2pctp.py

This program recalibrates stacks of X-ray projections with proton data. The recalibration curves

from *trchk* can be loaded and applied to arbitrary X-ray data. To speed up the processing, the tool also has a multi-core branch.

A.2 Treatment planning (TRiP98)

The treatment planning was performed using the TRiP98-64 version of the TRiP98 treatment planning software of GSI. For this purpose, the software *3D Slicer* [99] was first used for a conversion of the initial tif image stacks into integer HU values, which could then be exported to uncompressed .nhdr files containing the full CTs. This output was converted into a format suitable for use with TRiP98, which was done using the GSI internal *nrrd2hed.sh* script[1]. In case of the x7 phantom the data was first scaled up to the size of the x1 phantom. The output from the conventional xCT was then used for the optimization and recalculation of the dose in the recalibrated CT and pCT (scripts provided in Sec. A.2.1).

The visualization of the treatment planning was again executed in *3D Slicer*, the dose output from TRiP can be overlapped with the original CT data.

A.2.1 TRiP98 code

Phantom.exec

```
1  9*******************************************************************************
2  *
3  * Exec for dose optimization on Head Phantom
4  *
5  * patient: Head Phantom x1s
6  *
7  * author: Martin Schanz (m.schanz@gsi.de)
8  *
9  * $Id$
10 *                                                                          **
11 *******************************************************************************
12
13 *
14 * Scancaps, use HIT scanner magnet distances
15 *
16 scancap / offh2o(2.89) rifi(0) bolus(0.0) couch(0.0) gantry(90.0) minparticles(8000) path(uw2)
        scannerx(6521.9) scannery(7223.5) xmax(120) ymax(120)
17
18 *
19 * HIT base data
20 *
21 hlut * / delete
22 dedx * / delete
23 ddd * / delete
24 spc * / delete
25 sis * / delete
26
27 *
28
29 *
30 hlut "HIT_Schaedel_151216.hlut" / read
31 sis "/d/bio/stephan/hit/1H_1.1.2009.sis" / read
32 ddd "/d/bio/rgruen/1H_HIT/DDD/RF0MM/1H*.ddd" / read
33 spc "/d/bio/rgruen/1H_HIT/SPC/RF0MM/1H*.spc" / read
```

---

[1] By Kristjan Anderle (2014).

```
34  dedx "/d/bio/stephan/hit/dEdxFLUKAxTRiP.dedx" / read
35
36  *
37  * Random numbers
38  *
39  random 500
40
41
42  *
43  * CT
44  *
45  ct "CT" / read
46  *
47  * VOI
48  *
49  voi "Phantom" / read
50
51  plan / dose(2)
52
53  *
54  * OAR
55  *
56  *voi OAR / maxdosefraction(0.5) oarset
57  *voi * /list
58
59  *
60  * Optimize proton plan (OAR)
61  *field 1 / raster(3,3) proj(1H) fwhm(8) zstep(2) couch(270) gantry(152.0) new contour(1) distal
         (5.0)  doseext(1.8) target(116.8 95.4 42.9869)
62  * Optimize proton plan (SoftTissue)
63  field 1 / raster(3,3) proj(1H) fwhm(8) zstep(2) couch(90) gantry(-60.0) new contour(1) distal(5.0)
         doseext(1.8) target(107.8 110.4 42.9869)
64  opt / phys ctbased dosealg(msdb) bioalg(ld) optalg(fr) eps(1E-3) geps(1E-4) iter(300) nopreopt
         pyramid(1,1)
65
66  *field 1 / write file(X_Field_1.rst) * for OAR mode
67  field 1 / write file(X_Field_2.rst) * for SoftTissue mode
68
69  dose X_PhantomDose_ / calc field(*) alg(ms) bioalg(ld) nosvv norbe write maxthreads(32) datatype(
         float)
70
71  dvh  X_PhantomDVH / calc ex(gd)
72
73  quit
```

Phantom_doseRecalc.exec

```
1   9*****************************************************************************
2   *
3   * Exec for recal xCT dose recalculation
4   *
5   * patient: x1 HeadPhantom
6   *
7   * author: MSchanz (m.schanz@gsi.de)
8   *
9   * $Id$
10  *                                                                          **
11  *****************************************************************************
12
13  *
14  * Scancaps, use HIT scanner magnet distances
```

```
15  *
16  scancap / offh2o(2.89) rifi(3) bolus(0.0) couch(0.0) gantry(0.0) minparticles(8000) path(uw2)
        scannerx(6521.9) scannery(7223.5) xmax(120) ymax(120)
17
18  *
19  * HIT base data
20  *
21  hlut * / delete
22  dedx * / delete
23  ddd * / delete
24  spc * / delete
25  sis * / delete
26
27  *hlut "identity.hlut" / read
28  hlut "HIT_Schaedel_151216.hlut" / read
29  *sis "/u/rgruen/PHD_ION/TRIPDATA/1H_1.6.2008.sis" / read
30  sis "/d/bio/stephan/hit/1H_1.1.2009.sis" / read
31  ddd "/d/bio/rgruen/1H_HIT/DDD/RF0MM/1H*.ddd" / read
32  spc "/d/bio/rgruen/1H_HIT/SPC/RF0MM/1H*.spc" / read
33  dedx "/d/bio/stephan/hit/dEdxFLUKAxTRiP.dedx" / read
34  *
35  * Random numbers
36  *
37  random 500
38
39
40  *
41  * CT
42  *
43  ct "CT_Recalc_HU" / read
44  *
45  * VOI
46  *
47  voi "Phantom" / read
48
49  plan / dose(2)
50
51  *
52  * OAR
53  *
54  *voi OAR / maxdosefraction(0.5) oarset
55  *voi * /list
56
57
58  *
59  * Optimize plan on reference phase (OAR)
60  * field 1 / raster(3,3) proj(1H) fwhm(8) file(X_Field_1.rst) zstep(2) couch(270) gantry(152.0) read
        contour(1) distal(5.0)  doseext(1.8) target(116.8 95.4 42.9869)
61  * Optimize plan on reference phase (SoftTissue)
62  field 1 / raster(3,3) proj(1H) fwhm(8) file(X_Field_2.rst) zstep(2) couch(90) gantry(-60.0) read
        contour(1) distal(5.0)  doseext(1.8) target(107.8 110.4 42.9869)
63
64
65  dose X_PhantomDose_Recalc_ / calc field(*) alg(ms) bioalg(ld) nosvv norbe write maxthreads(32)
        datatype(float)
66
67  dvh  X_PhantomDVH_Recalc / calc ex(gd)
68
69  quit
```

PhantompCT_doseRecalc.exec

```
1  9******************************************************************************
2  *
3  * Exec for pCT dose recalculation
4  *
5  * patient: x7 HeadPhantom (scaled)
6  *
7  * author: MSchanz (m.schanz@gsi.de)
8  *
9  * $Id$
10 *                                                                        **
11 ******************************************************************************
12
13 *
14 * Scancaps, use HIT scanner magnet distances
15 *
16 scancap / offh2o(2.89) rifi(3) bolus(0.0) couch(0.0) gantry(0.0) minparticles(8000) path(uw2)
       scannerx(6521.9) scannery(7223.5) xmax(120) ymax(120)
17
18 *
19 * get HIT base data
20 *
21 hlut * / delete
22 dedx * / delete
23 ddd * / delete
24 spc * / delete
25 sis * / delete
26
27 hlut "HIT_Schaedel_151216.hlut" / read
28 sis "/d/bio/stephan/hit/1H_1.1.2009.sis" / read
29 ddd "/d/bio/rgruen/1H_HIT/DDD/RF0MM/1H*.ddd" / read
30 spc "/d/bio/rgruen/1H_HIT/SPC/RF0MM/1H*.spc" / read
31 dedx "/d/bio/stephan/hit/dEdxFLUKAxTRiP.dedx" / read
32
33 *
34 * Load CT
35 *
36 ct "CT_pCT" / read
37 *
38 * Load VOI
39 *
40 voi "Phantom" / read
41
42 plan / dose(2)
43
44 *
45 * OAR
46 *
47 *voi OAR / maxdosefraction(0.5) oarset
48 *voi * /list
49
50 *
51 * Optimize plan on reference phase (OAR)
52 * field 1 / raster(3,3) proj(1H) fwhm(8) file(X_Field_1.rst) zstep(2) couch(270) gantry(152.0) read
       contour(1) distal(5.0)  doseext(1.8) target(116.8 95.4 42.9869)
53 * Optimize plan on reference phase (SoftTissue)
54 field 1 / raster(3,3) proj(1H) fwhm(8) file(X_Field_2.rst) zstep(2) couch(90) gantry(-60.0) read
       contour(1) distal(5.0)  doseext(1.8) target(107.8 110.4 42.9869)
55
```

```
56  dose X_PhantomDose_pCT_ / calc field(*) alg(ms) bioalg(ld) nosvv norbe write maxthreads(32)
        datatype(float)
57
58  dvh  X_PhantomDVH_pCT / calc ex(gd)
59
60  quit
```

Bibliography

[1] R. Koch-Institut, *"Krebs in Deutschland für 2013/2014,"* Zentrum für Krebsregisterdaten **11** (2017).

[2] C. Morris, J. Hopson, and P. Goldstone, *"Proton Radiography,"* Los Alamos Science **30** (2006).

[3] M. Prall, M. Durante, T. Berger, B. Przybyla, C. Graeff, P. M. Lang, C. LaTessa, L. Shestov, P. Simoniello, C. Danly, and et al., *"High-energy proton imaging for biomedical applications,"* Scientific Reports **6** (2016), 10.1038/srep27651.

[4] M. Lederman, *"The early history of radiotherapy: 1895–1939,"* International Journal of Radiation Oncology*Biology*Physics **7**, 639 – 648 (1981).

[5] R. R. Wilson, *"Radiological Use of Fast Protons,"* Radiology **47**, 487–491 (1946).

[6] E. C. Halperin, *"Particle therapy and treatment of cancer,"* The Lancet Oncology **7**, 676–685 (2006).

[7] E. Pedroni, R. Bacher, H. Blattmann, T. Böhringer, A. Coray, A. Lomax, S. Lin, G. Munkel, S. Scheib, U. Schneider, and A. Tourovsky, *"The 200-MeV proton therapy project at the Paul Scherrer Institute: Conceptual design and practical realization,"* Medical Physics **22**, 37–53 (1995).

[8] H. Eickhoff, T. Haberer, G. Kraft, U. Krause, M. Richter, R. Steiner, and J. Debus, *"The GSI Cancer Therapy Project,"* Strahlentherapie und Onkologie **175**, 21–24 (1999).

[9] T. Elsässer, W. K. Weyrather, T. Friedrich, M. Durante, G. Iancu, M. Krämer, G. Kragl, S. Brons, M. Winter, K.-J. Weber, and M. Scholz, *"Quantification of the Relative Biological Effectiveness for Ion Beam Radiotherapy: Direct Experimental Comparison of Proton and Carbon Ion Beams and a Novel Approach for Treatment Planning,"* International Journal of Radiation Oncology*Biology*Physics **78**, 1177 – 1183 (2010).

[10] P. Peschke, C. P. Karger, M. Scholz, J. Debus, and P. E. Huber, *"Relative Biological Effectiveness of Carbon Ions for Local Tumor Control of a Radioresistant Prostate Carcinoma in the Rat,"* International Journal of Radiation Oncology*Biology*Physics **79**, 239 – 246 (2011).

[11] M. Jermann, ed., *Particle Therapy Statistics (per end of 2016)*, Particle Therapy Co-Operative Group (PTCOG, 2017).

[12] O. Sokol, E. Scifoni, S. Hild, M. Durante, and M. Krämer, *"216. Biological treatment planning with multiple ion beams,"* Physica Medica **56**, 193 – 194 (2018), Abstracts of the 10th National Congress of the Associazione Italiana di Fisica Medica.

[13] W. C. Röntgen, *"Über eine neue Art von Strahlen,"* Sitzungberichte der Physik.-Mediz.-Gesellschaft zu Würzburg , 132 (1895).

[14] J. Radon, *"Über die Bestimmung von Funktionen durch ihre Integralwerte längs gewisser Mannigfaltigkeiten,"* Berichte Sächsische Academie der Wissenschaften **69** (1917), 10.1090/psapm/027.

[15] A. M. Cormack, *"Reconstruction of densities from their projections, with applications in radiological physics,"* Physics in Medicine and Biology **18**, 195 (1973).

[16] G. N. Hounsfield, *"Computerized transverse axial scanning (tomography): Part 1. Description of system,"* The British Journal of Radiology **46**, 1016–1022 (1973).

[17] J. H. Hubbell, *Photon Cross Sections, Attenuation Coefficients, and Energy Absorption Coefficients From 10 keV to 100 GeV* (Center for Radiation Reserach - National Bureau of Standards, Washington D.C. 20234, 1969).

[18] R. Zhang and W. D. Newhauser, *"Calculation of water equivalent thickness of materials of arbitrary density, elemental composition and thickness in proton beam irradiation,"* Physics in Medicine and Biology **54**, 1383–1395 (2009).

[19] W. R. Leo, *Techniques for Nuclear and Particle Physics Experiments* (Springer Berlin Heidelberg, 1994).

[20] S. J. Goetsch, *"Atoms, Radiation and Radiation Protection by J. E. Turner,"* Medical Physics **14**, 156–156 (1987).

[21] E. Rietzel, D. Schardt, and T. Haberer, *"Range accuracy in carbon ion treatment planning based on CT-calibration with real tissue samples,"* Radiation Oncology **2** (2007), 10.1186/1748-717x-2-14.

[22] H. Paganetti, *"Range uncertainties in proton therapy and the role of Monte Carlo simulations,"* Physics in Medicine and Biology **57**, R99–R117 (2012).

[23] W. van Elmpt, G. Landry, M. Das, and F. Verhaegen, *"Dual energy CT in radiotherapy: Current applications and future outlook,"* Radiotherapy and Oncology **119**, 137 – 144 (2016).

[24] M. Tsukihara, Y. Noto, T. Hayakawa, and M. Saito, *"Conversion of the energy-subtracted CT number to electron density based on a single linear relationship: an experimental verification using a clinical dual-source CT scanner,"* Physics in Medicine and Biology **58**, N135–N144 (2013).

[25] G. Landry, J. Seco, M. Gaudreault, and F. Verhaegen, *"Deriving effective atomic numbers from DECT based on a parameterization of the ratio of high and low linear attenuation coefficients,"* Physics in Medicine and Biology **58**, 6851–6866 (2013).

[26] N. Hudobivnik, F. Schwarz, T. Johnson, L. Agolli, G. Dedes, T. Tessonnier, F. Verhaegen, C. Thieke, C. Belka, W. H. Sommer, K. Parodi, and G. Landry, *"Comparison of proton*

therapy treatment planning for head tumors with a pencil beam algorithm on dual and single energy CT images," Medical Physics **43**, 495–504 (2016).

[27] P. Wohlfahrt, C. Möhler, V. Hietschold, S. Menkel, S. Greilich, M. Krause, M. Baumann, W. Enghardt, and C. Richter, "*Clinical Implementation of Dual-energy CT for Proton Treatment Planning on Pseudo-monoenergetic CT scans,*" International Journal of Radiation Oncology*Biology*Physics **97**, 427 – 434 (2017).

[28] A. M. Koehler, "*Proton Radiography,*" Science **160**, 303–304 (1968).

[29] J. A. Cookson, "*Radiography with protons,*" Naturwissenschaften **61**, 184–191 (1974).

[30] J. Cookson, B. Armitage, and A. Ferguson, "*Proton radiography,*" Non-Destructive Testing **5**, 225 – 228 (1972).

[31] D. West, "*The Potential of Proton Radiography,*" , 503–506 (1975), 7th International Conference on Cyclotrons and their Applications: Zürich, Switzerland, 19–22 August 1975.

[32] N. King, E. Ables, K. Adams, K. Alrick, J. Amann, S. Balzar, P. B. Jr, M. Crow, S. Cushing, J. Eddleman, T. Fife, P. Flores, D. Fujino, R. Gallegos, N. Gray, E. Hartouni, G. Hogan, V. Holmes, S. Jaramillo, J. Knudsson, R. London, R. Lopez, T. McDonald, J. McClelland, F. Merrill, K. Morley, C. Morris, F. Naivar, E. Parker, H. Park, P. Pazuchanics, C. Pillai, C. Riedel, J. Sarracino, F. S. Jr, H. Stacy, B. Takala, R. Thompson, H. Tucker, G. Yates, H. Ziock, and J. Zumbro, "*An 800-MeV proton radiography facility for dynamic experiments,*" Nuclear Instruments and Methods in Physics Research Section A: Accelerators, Spectrometers, Detectors and Associated Equipment **424**, 84 – 91 (1999).

[33] A. V. Kantsyrev, A. A. Golubev, V. I. Turtikov, A. V. Bogdanov, B. Y. Sharkov, V. S. Demidov, V. S. Skachkov, N. V. Markov, V. B. Mintsev, V. E. Fortov, and et al., "*ITEP proton microscopy facility,*" 2013 19th IEEE Pulsed Power Conference (PPC) (2013), 10.1109/ppc.2013.6627498.

[34] D. Varentsov, A. Bogdanov, V. S. Demidov, A. A. Golubev, A. Kantsyrev, P. M. Lang, D. N. Nikolaev, N. Markov, F. Natale, L. Shestov, P. Simoniello, G. N. Smirnov, and M. Durante, "*First biological images with high-energy proton microscopy,*" Physica Medica **29**, 208–213 (2013).

[35] Y. Antipov, A. Afonin, A. Vasilevskii, I. Gusev, V. Demyanchuk, O. Zyat'kov, N. Ignashin, Y. Karshev, A. Larionov, A. Maksimov, A. Matyushin, A. Minchenko, M. Mikheev, V. Mirgorodskii, V. Peleshko, V. Rud'ko, V. Terekhov, N. Tyurin, Y. Fedotov, Y. Trutnev, V. Burtsev, A. Volkov, I. Ivanin, S. Kartanov, Y. Kuropatkin, A. Mikhailov, K. Mikhailyukov, O. Oreshkov, A. Rudnev, G. Spirov, M. Syrunin, M. Tatsenko, I. Tkachenko, and I. Khramov, "*A radiographic facility for the 70-GeV proton accelerator of the institute for high energy physics,*" Instruments and Experimental Techniques **53**, 319–326 (2010).

[36] C. L. Morris, E. Ables, K. R. Alrick, M. B. Aufderheide, P. D. Barnes, K. L. Buescher, D. J. Cagliostro, D. A. Clark, D. J. Clark, C. J. Espinoza, E. N. Ferm, R. A. Gallegos, S. D. Gardner, J. J. Gomez, G. A. Greene, A. Hanson, E. P. Hartouni, G. E. Hogan, N. S. P. King, K. Kwiatkowski, R. P. Liljestrand, F. G. Mariam, F. E. Merrill, D. V. Morgan, K. B. Morley, C. T. Mottershead, M. M. Murray, P. D. Pazuchanics, J. E. Pearson, J. S. Sarracino, A. Saunders, J. Scaduto, A. E. Schach von Wittenau, R. A. Soltz, S. Sterbenz, R. T. Thompson, K. Vixie, M. D. Wilke, D. M. Wright, and J. D. Zumbro, "*Flash radiography with 24 GeV/c protons,*" J. Appl. Phys. **109**, 104905 (2011).

[37] D. Varentsov, O. Antonov, A. Bakhmutova, C. W. Barnes, A. Bogdanov, C. R. Danly, S. Efimov, M. Endres, A. Fertman, A. A. Golubev, and et al., "*Commissioning of the PRIOR proton microscope,*" Review of Scientific Instruments **87**, 023303 (2016).

[38] Y. Zhao, R. Cheng, Y. Wang, X. Zhou, Y. Lei, Y. Sun, G. Xu, J. Ren, L. Sheng, Z. Zhang, and et al., "*High energy density physics research at IMP, Lanzhou, China,*" High Power Laser Science and Engineering **2** (2014), 10.1017/hpl.2014.44.

[39] L. Sheng, Y. Zhao, G. Yang, T. Wei, X. Jiang, X. Zhou, R. Cheng, Y. Yan, P. Li, J. Yang, and et al., "*Heavy-ion radiography facility at the Institute of Modern Physics,*" Laser and Particle Beams **32**, 651–655 (2014).

[40] Y. Yan, L. Sheng, Z. Huang, J. Wang, Z. Yao, J. Wang, Z. Wei, J. Yang, and Y. Yuan, "*Simulation of proton radiography terminal at the Institute of Modern Physics,*" Laser and Particle Beams **33**, 439–447 (2015).

[41] J. Yang, J. Xia, G. Xiao, H. Xu, H. Zhao, X. Zhou, X. Ma, Y. He, L. Ma, D. Gao, J. Meng, Z. Xu, R. Mao, W. Zhang, Y. Wang, L. Sun, Y. Yuan, P. Yuan, W. Zhan, J. Shi, W. Chai, D. Yin, P. Li, J. Li, L. Mao, J. Zhang, and L. Sheng, "*High Intensity heavy ion Accelerator Facility (HIAF) in China,*" Nuclear Instruments and Methods in Physics Research Section B: Beam Interactions with Materials and Atoms **317**, 263 – 265 (2013), XVIth International Conference on ElectroMagnetic Isotope Separators and Techniques Related to their Applications, December 2–7, 2012 at Matsue, Japan.

[42] X. Ma, W. Wen, S. Zhang, D. Yu, R. Cheng, J. Yang, Z. Huang, H. Wang, X. Zhu, X. Cai, Y. Zhao, L. Mao, J. Yang, X. Zhou, H. Xu, Y. Yuan, J. Xia, H. Zhao, G. Xiao, and W. Zhan, "*HIAF: New opportunities for atomic physics with highly charged heavy ions,*" Nuclear Instruments and Methods in Physics Research Section B: Beam Interactions with Materials and Atoms **408**, 169 – 173 (2017), Proceedings of the 18th International Conference on the Physics of Highly Charged Ions (HCI-2016), Kielce, Poland, 11-16 September 2016.

[43] U. Schneider, J. Besserer, P. Pemler, M. Dellert, M. Moosburger, E. Pedroni, and B. Kaser-Hotz, "*First proton radiography of an animal patient,*" Medical Physics **31**, 1046–1051 (2004).

[44] D. L. Presti, G. Gallo, D. L. Bonanno, F. Longhitano, D. G. Bongiovanni, S. Reito, N. Randazzo, E. Leonora, V. Sipala, and F. Tommasino, "*An Innovative Proton Tracking System for*

Qualification of Particle Beam in Real-Time," IEEE Transactions on Radiation and Plasma Medical Sciences **1**, 268–274 (2017).

[45] J. Taylor, C. Waltham, T. Price, N. Allinson, P. Allport, G. Casse, A. Kacperek, S. Manger, N. Smith, and I. Tsurin, "*A new silicon tracker for proton imaging and dosimetry*," Nuclear Instruments and Methods in Physics Research Section A: Accelerators, Spectrometers, Detectors and Associated Equipment **831**, 362–366 (2016).

[46] M. Bucciantonio, U. Amaldi, R. Kieffer, F. Sauli, and D. Watts, "*Development of a fast proton range radiography system for quality assurance in hadrontherapy*," Nuclear Instruments and Methods in Physics Research Section A: Accelerators, Spectrometers, Detectors and Associated Equipment **732**, 564 – 567 (2013), Vienna Conference on Instrumentation 2013.

[47] V. A. Bashkirov, R. W. Schulte, R. F. Hurley, R. P. Johnson, H. F.-W. Sadrozinski, A. Zatserklyaniy, T. Plautz, and V. Giacometti, "*Novel scintillation detector design and performance for proton radiography and computed tomography*," Medical Physics **43**, 664–674 (2016).

[48] M. Scaringella, M. Bruzzi, M. Bucciolini, M. Carpinelli, G. A. P. Cirrone, C. Civinini, G. Cuttone, D. L. Presti, S. Pallotta, C. Pugliatti, and et al., "*A proton Computed Tomography based medical imaging system*," Journal of Instrumentation **9** (2014), 10.1088/1748-0221/9/12/c12009.

[49] M. Esposito, T. Price, S. Manger, C. Waltham, T. Anaxagoras, D. J. Parker, J. Nieto-Camero, and N. Allinson, "*A large area CMOS Active Pixel Sensor for imaging in proton therapy*," Journal of Instrumentation **13** (2018), 10.1088/1748-0221/13/11/p11017.

[50] J. Telsemeyer, O. Jäkel, and M. Martišíková, "*Quantitative carbon ion beam radiography and tomography with a flat-panel detector*," Physics in Medicine and Biology **57**, 7957–7971 (2012).

[51] H.-W. Sadrozinski, R. Johnson, S. Macafee, A. Plumb, D. Steinberg, A. Zatserklyaniy, V. Bashkirov, R. Hurley, and R. Schulte, "*Development of a head scanner for proton CT*," Nuclear Instruments and Methods in Physics Research Section A: Accelerators, Spectrometers, Detectors and Associated Equipment **699**, 205 – 210 (2013), Proceedings of the 8th International "Hiroshima" Symposium on the Development and Application of Semiconductor Tracking Detectors.

[52] J. Müller, C. Neubert, C. von Neubeck, M. Baumann, M. Krause, W. Enghardt, R. Bütof, A. Dietrich, and A. Lühr, "*Proton radiography for inline treatment planning and positioning verification of small animals*," Acta Oncologica **56**, 1399–1405 (2017).

[53] B. E. Fischer and R. Spohr, "*Heavy ion microlithography — a new tool to generate and investigate submicroscopic structures*," Nuclear Instruments and Methods **168**, 241 – 246 (1980).

[54] A. Dymnikov and S. Yavor, *"Four quadrupole lenses as an analogue of an axially symmetric system,"* Zh. Tekh. Fiz. **33**, 851 (1963).

[55] D. C. Carey, K. L. Brown, and F. Rothacker, *Third-order TRANSPORT: a computer program for designing charged particle beam transport systems*, Tech. Rep. SLAC-R-95-462 (Stanford Linear Accelerator Center, 1995).

[56] H. Wollnik, *Optics of Charged Particles*, ISBN 0-12-762130-X (Academic Press, Inc., 1987).

[57] C. T. Mottershead and J. D. Zumbro, *"Magnetic optics for proton radiography,"* in *Particle Accelerator Conference, 1997*, Vol. 2 (1997) pp. 1397–1399.

[58] F. E. Merrill, *"Flash Proton Radiography,"* Reviews of Accelerator Science and Technology **08**, 165–180 (2015).

[59] M. Tanabashi and et al., *"Review of Particle Physics - Passage of particles through matter,"* Physical Review D **98** (2018), 10.1103/PhysRevD.98.030001.

[60] G. Moliere, *"Theorie der Streuung schneller geladener Teilchen I: Einzelstreuung am abgeschirmten Coulomb-Feld,"* Z. Naturforsch. Phys. Sci. **2a**, 133ff (1947).

[61] G. Moliere, *"Theorie der Streuung schneller geladener Teilchen II: Mehrfach- und Vielfach-streuung,"* Z. Naturforsch. Phys. Sci. **3a**, 78ff (1948).

[62] H. A. Bethe, *"Molière's Theory of Multiple Scattering,"* Physical Review **89**, 1256–1266 (1953).

[63] V. L. Highland, *"Some Practical Remarks on Multiple Scattering,"* Nucl. Instr. and Meth. **129**, 497 (1975).

[64] G. R. Lynch and O. I. Dahl, *"Approximations to multiple Coulomb scattering,"* Nucl. Instr. and Meth. B **58**, 6–10 (1991).

[65] B. Gottschalk, A. Koehler, R. Schneider, J. Sisterson, and M. Wagner, *"Multiple Coulomb scattering of 160 MeV protons,"* Nuclear Instruments and Methods in Physics Research Section B: Beam Interactions with Materials and Atoms **74**, 467 – 490 (1993).

[66] F. G. Mariam, F. E. Merrill, C. J. Espinoza, J. A. Heidemann, B. J. Hollander, K. K. Kwiatkowski, J. D. Lopez, R. P. Lopez, M. Marr-Lyon, W. V. McNeil, and et al., *"Proton radiography: its uses and resolution scaling,"* Penetrating Radiation Systems and Applications XIII (2012), 10.1117/12.930569.

[67] P.-M. Lang, *Aufbau und Test des Protonenmikroskops PRIOR (Construction and test of the PRIOR microscope)*, Ph.D. thesis, Technische Universität, Darmstadt (2015).

[68] M. Schanz, *Design of a 5 GeV Proton Microscope for FAIR*, Masters thesis, TU Darmstadt (2015).

[69] M. Schanz, *Einfluss protoneninduzierter Strahlung auf NdFeB-Permanentmagnete*, Bachelor thesis, TU Darmstadt (2013).

[70] C. R. Danly, F. E. Merrill, D. Barlow, and F. G. Mariam, "*Nonuniform radiation damage in permanent magnet quadrupoles*," Review of Scientific Instruments **85**, 083305 (2014).

[71] M. Schanz, M. Endres, K. Löwe, T. Lienig, O. Deppert, P. M. Lang, D. Varentsov, D. H. H. Hoffmann, and O. Gutfleisch, "*High energy proton induced radiation damage of rare earth permanent magnet quadrupoles*," Review of Scientific Instruments **88**, 125103 (2017).

[72] Z. Li, Y. Jia, R. Liu, Y. Xu, G. Wang, and X. Xia, "*Investigation on demagnetization of Nd2Fe14B permanent magnets induced by irradiation*," Nuclear Instruments and Methods in Physics Research Section B: Beam Interactions with Materials and Atoms **413**, 68 – 74 (2017).

[73] P. Lisowski and K. Schoenberg, "*The Los Alamos Neutron Science Center*," Nuclear Instruments and Methods in Physics Research Section A: Accelerators, Spectrometers, Detectors and Associated Equipment **562**, 910 – 914 (2006), Proceedings of the 7th International Conference on Accelerator Applications.

[74] F. Merrill, D. Barlow, C. Espinoza, B. Hollander, K. Kwiatkowski, J. Lopez, F. Mariam, D. Morley, C. Morris, P. Nedrow, A. Saunders, A. M. Tainter, D. Tupa, and J. Tybo, "*Imaging Systems for 800 MeV Proton Radiography*," Proceedings of IPAC2014 (2014).

[75] K. Kwiatkowski, P. Nedrow, C. Morris, F. Mariam, F. Merrill, A. Saunders, and G. Hogan, "*Ultra-Fast Hybrid-CMOS Imaging System for Multi-Frame Proton Radiography*," 29th International Congress on High-Speed Imaging and Photonics **Morioka, Japan** (2010).

[76] K. Makino and M. Berz, "*COSY INFINITY Version 9*," Nuclear Instruments and Methods in Physics Research Section A: Accelerators, Spectrometers, Detectors and Associated Equipment **558**, 346 – 350 (2006), Proceedings of the 8th International Computational Accelerator Physics Conference.

[77] D. Varentsov, "*PROSIT Documentation*," GSI internal (2016).

[78] F. Heuck and K. Vanselow, *Radiologische Analyse des Knochens: Bestimmmung der Mineralkonzentration* (Springer-Verlag, 2005).

[79] J. Laubenberger, *Technik der medizinischen Radiologie*, 1st ed., 978-3769111323 (Deutscher Ärzteverlag, 1999).

[80] H. Hundeshagen, *Radiologie*, 1st ed., 978-3-642-66701-5 (Springer Verlag, 1978).

[81] N. Peters, *X-Ray CT Recalibration for Particle Therapy using 2D Flash Proton Radiography*, Masters thesis, Martin Luther University of Halle-Wittenberg (2017).

[82] W. Schlegel and J. Bille, *Medizinische Physik 2 - Medizinische Strahlenphysik*, ISBN 3-540-65254-X (Springer Verlag, 2002).

[83] D. A. Kartini, *"Imaging and Radiobiological Applications for Ion Beam Therapy,"* GET IN-volved Internship and Training Project Report (2018).

[84] M. Krämer, O. Jäkel, T. Haberer, G. Kraft, D. Schardt, and U. Weber, *"Treatment planning for heavy-ion radiotherapy: physical beam model and dose optimization,"* Physics in Medicine and Biology **45**, 3299–3317 (2000).

[85] M. Krämer, E. Scifoni, C. Wälzlein, and M. Durante, *"Ion beams in radiotherapy - from tracks to treatment planning,"* Journal of Physics: Conference Series **373**, 012017 (2012).

[86] M. Durante and H. Stöcker, *"Relativistic protons for image-guided stereotactic radiosurgery,"* Journal of Physics: Conference Series **373**, 012016 (2012).

[87] M. S. Freeman, J. Allison, C. Espinoza, J. J. Goett, G. Hogan, B. Hollander, K. Kwiatkowski, J. Lopez, F. Mariam, M. Martinez, and et al., *"800-MeV magnetic-focused flash proton radiography for high-contrast imaging of low-density biologically-relevant targets using an inverse-scatter collimator,"* Medical Imaging 2016: Physics of Medical Imaging (2016), 10.1117/12.2216862.

[88] R. Schulte, V. Bashkirov, , J. Z. Liang, K. Mueller, J. Heimann, L. R. Johnson, B. Keeney, H. F. . Sadrozinski, A. Seiden, D. C. Williams, , , S. Peggs, T. Satogata, and C. Woody, *"Design of a proton computed tomography system for applications in proton radiation therapy,"* **3**, 1579–1583 Vol.3 (2003), 2003 IEEE Nuclear Science Symposium. Conference Record (IEEE Cat. No.03CH37515).

[89] E. Pedroni, D. Meer, C. Bula, S. Safai, and S. Zenklusen, *"Pencil beam characteristics of the next-generation proton scanning gantry of PSI: design issues and initial commissioning results,"* The European Physical Journal Plus **126** (2011), 10.1140/epjp/i2011-11066-0.

[90] N. Chaudhri, N. Saito, C. Bert, B. Franczak, P. Steidl, M. Durante, E. Rietzel, and D. Schardt, *"Ion-optical studies for a range adaptation method in ion beam therapy using a static wedge degrader combined with magnetic beam deflection,"* Physics in Medicine and Biology **55**, 3499–3513 (2010).

[91] U. Scheeler, C. Krantz, S. Sievers, M. Strohmeier, R. Cee, E. Feldmeier, M. Galonska, K. Höppner, J. Mosthaf, S. Scheloske, T. Winkelmann, C. Schömers, A. Peters, and T. Haberer, *"Recommissioning of the Marburg Ion-beam Therapy Centre (MIT) Accelerator Facility,"* (2016) Proceedings of IPAC2016, Busan, Korea.

[92] S. Rossi, *"The status of CNAO,"* The European Physical Journal Plus **126** (2011), 10.1140/epjp/i2011-11078-8.

[93] M. G. Pullia *et al.*, *"The Experimental Beam Line at CNAO,"* in *Proc. of International Particle Accelerator Conference (IPAC'16), Busan, Korea, May 8-13, 2016*, 7 (JACoW, Geneva, Switzerland, 2016) pp. 1334–1336.

[94] M. Benedikt, J. Gutleber, M. Palm, W. Pirkl, U. Dorda, and A. Fabich, *"Overview of the MedAustron design and technology choices,"* Proceedings of IPAC'10, Kyoto, Japan (2010).

[95] U. Dorda, M. Benedikt, and P. Bryant, *"Layout and Optics of the MedAustron High Energy Beam Transfer Line,"* Proceedings of IPAC2011, San Sebastián, Spain (2011).

[96] M. S. Freeman, J. Allison, M. Andrews, E. Ferm, J. J. Goett, K. Kwiatkowski, J. Lopez, F. Mariam, M. Marr-Lyon, M. Martinez, and et al., *"Inverse-collimated proton radiography for imaging thin materials,"* Review of Scientific Instruments **88**, 013709 (2017).

[97] N. K. Abrosimov, Y. A. Gavrikov, E. M. Ivanov, D. L. Karlin, A. V. Khanzadeev, N. N. Ya-lynych, G. A. Riabov, D. M. Seliverstov, and V. M. Vinogradov, *"1000 MeV Proton beam therapy facility at Petersburg Nuclear Physics Institute Synchrocyclotron,"* Journal of Physics: Conference Series **41**, 424–432 (2006).

[98] F. A. Cucinotta, R. Katz, J. W. Wilson, L. W. Townsend, J. Shinn, and F. Hajnal, *"Biological Effectiveness of High-Energy Protons: Target Fragmentation,"* Radiation Research **127**, 130–137 (1991).

[99] R. Kikinis, S. D. Pieper, and K. G. Vosburgh, *"3D Slicer: A Platform for Subject-Specific Image Analysis, Visualization, and Clinical Support,"* Intraoperative Imaging and Image-Guided Therapy , 277–289 (2013).

Acknowledgments

Despite the incredibly short time frame of just three years a huge number of people have contributed and actively supported this project in many ways, which was – at least at the beginning – not even meant to be the primary focus of my PhD. It was an exciting period and I'm grateful for all of the support I received along the way!

PhD facts	
Category	**Value**
Travel	
Total distance traveled by car	53356.12 km
Amount of diesel burned	2865.23 l
Total number of flights	48
Total distance traveled by plane	127965.48 km
CO_2 footprint	47.24 t
Tree equivalence (*Naturefund e.V. Deutschland*)	107
Experiments	
Number of beam times (X-ray & p^+)	5
Amount of data collected	104.53 GB
Working Hours	
Working hours in office (excluding travel)	4897 h
Full travel days (conference or experiment)	85 days

First of all, the most gratitude has to be expressed to my advisor, Michael Krämer, who was curious about the idea of medical imaging and agreed to shift the focus of my thesis on this topic. Not only did he support the numerous business trips for experiments and conferences but also provided valuable ideas and was always available for fruitful discussions on all sorts of physical issues. I would also like to thank the Co-referent of my thesis, Prof. Marco Durante, and my PhD committee, Prof. Dieter H.H. Hoffmann and Prof. Reinhold Walser. Thanks to the whole *Treatment planning and validation group* and especially to Martina Fuss, who supported me coaching the undergraduate students and helped with all sorts of organizational and physical issues.

Furthermore, on the GSI side, I want to thank Christian Graeff, Christjan Anderle and Matthias Prall for the help with Slicer, TRiP and all sorts of technical and administrative is-

sues regarding the beam times. Thanks to the GSI plasma physics group, especially to Dmitry Varentsov from the German PRIOR project, who helped a lot with all sorts of preparation for the beam times and with simulations. Without his long term experience and advice I would have struggled running the experiments at LANL on my own. Thanks also to Michael Endres for the wonderful discussions and various experiments which finally resulted in the paper on radiation damage of permanent magnets.

A big thanks receives the pRAD team at Los Alamos, especially the P-25 team leader Dale Tupa, who made the collaboration on biomedical imaging between GSI and LANL possible. She helped dealing with the complicated paperwork and even managed to invite me to push the acceptance of this project and this collaboration at LANL. Special thanks to Levi Neukirch and Matthew Freeman for the help during the beam times and the good communication on all sorts of technical issues. We had plenty of fruitful discussions also together with the rest of the team, Fesseha Mariam, Frank Merrill and Michelle Espy.

Next to GSI and LANL the dosimetry was supported by the DLR (Thomas Berger and Bartos Pryzbylla) and the X-ray imaging at the HIT would not have been possible without the commitment and patience of Hannah Prokesch.

During my PhD I further had the chance to work with some excellent undergraduate students and to support them on their scientific career. Nils Peters from the TU Dresden worked a lot on the recalibration part and successfully completed his masters on the project, Dea Kartini from SUT, Thailand helped with the density resolution predictions and Sarat Lewsirirat helped setting up small and simple rotation stages for future pCT experiments at LANL.

I also want to mention the *mixed BIO lunch & coffee group* with all its current and past members (Antonia, Tabea, Christoph, Bahar, Kim, Celine, Ellen, Paul, Susanne, Christian, David, Florian, Franziska, Jona, Laura, Milana, Izabella, Suleiman, Maik, Alina, Timo, Emily, etc.), it was delightful to be part of such a welcoming and friendly family. Thanks for the exciting travel all across Europe, for the sports events and parties and for the interesting and sometimes absurd discussions during the lunch breaks.

Last but not least I would like to thank my old friends from gymnastics and music, who always allow my mind to come to a rest. I also thank my parents for their support and Franziska Wolf for always bearing with me during the past years and of course for the unphysical remarks to this work.

Curriculum Vitae

Personal

	Martin Schanz *21.11.1989, Langen, Germany
04/2016 - 04/2019	**GSI Helmholtzzentrum für Schwerionenforschung GmbH** PhD Researcher in the Biophysics Department
04/2014 - 02/2016	**Technische Universität Darmstadt** Master of Science in Physics **Thesis:** "High Energy Proton Microscopy at FAIR"
10/2010 - 04/2014	**Technische Universität Darmstadt** Bachelor of Science in Physics **Thesis:** "Influence of Proton Induced Radiation on NdFeB Permanent Magnets"
08/2009 - 08/2010	Alternative Civilian Service at Sportjugend Hessen e.V.
06/2009	Abitur at Claus von Stauffenberg Schule, Rodgau

Scientific Disclosures

Publications	M. Endres and M. Schanz, **Investigation of Proton induced Demagentisation Effects in Permanent Magnet Quadrupoles**, *News and Reports from High Energy Density generated by Heavy Ion and Laser Beams 2017*, 2018
	M. Schanz, **Applications for proton radiography in radiation oncology**, *GSI Scientific Report*, 2017
	M. Schanz, M. Endres, K. Löwe, T. Lienig. O. Deppert, P.M. Lang, D. Varentsov, D.H.H. Hoffmann and O. Gutfleisch, **High energy proton induced radiation damage of rare earth permanent magnet quadrupoles**, *Rev. Sci. Instrum.*, **88**(125103), 2017
	M. Schanz, **High energy proton imaging for medical applications at FAIR**, *GSI Scientific Report*, 2016

M. Endres, M. Schanz., P.M. Lang and D.H.H. Hoffmann, **Demagnetisation of PRIOR Permanent Quadrupol Magenet**, *News and Reports from High Energy Density generated by Heavy Ion and Laser Beams 2015*, 2016.

M. Schanz, **Flash Proton Radiography: Recent Results**, *News and Reports from High Energy Density generated by Heavy Ion and Laser Beams 2015*, 2016

D. Varentsov, O. Antonov, A. Bakhmutova, C. W. Barnes, A. Bogdanov, C. R. Danly, S. Efimov, M. Endres, A. Fertman, A. A. Golubev, D. H. H. Hoffmann, B. Ionita, A. Kantsyrev, Ya. E. Krasik, P. M. Lang, I. Lomonosov, F. G. Mariam, N. Markov, F. E. Merrill, V. B. Mintsev, D. Nikolaev, V. Panyushkin, M. Rodionova, M. Schanz, K. Schoenberg, A. Semennikov, L. Shestov, V. S. Skachkov, V. Turtikov, S. Udrea, O. Vasylyev, K. Weyrich, C. Wilde, and A. Zubareva, **Commissioning of the prior proton microscope**, *Rev. Sci. Instrum.*, **87**(023303), 2016

M. Schanz, **Design of a 5GeV Proton Microscope for FAIR**, *GSI Scientific Report*, 2015

Talks	**Proton Radiography towards medical applications** (invited), *Proton Radiography for Materials Discovery: Mesoscale and Beyond*, 2018, Santa Fe, USA

PRIOR-II - A novel Proton Radiography Facility for FAIR (invited), *3nd International Conference on Matter and Radiation in Extremes*, 2018, Qingdao, China

PRIOR - Proton Radiography for FAIR, *Workshop on Sino-German Collaboration on HEDP*, 2017, Xi'An, China

The PaNTERA Project - Recalibrating xCT Data with Flash Proton Radiography, *Workshop on Ions for Cancer Therapy, Space Research and Material Science*, 2017, Chania, Greece

PRIOR - Proton Radiography for FAIR (invited), *2nd International Conference on Matter and Radiation in Extremes*, 2017, Beijing, China

PaNTERA - Proton Therapy and Radiography, *37th International Workshop on Physics of High Energy Density in Matter*, 2017, Hirschegg, Austria

The PRIOR Project, *HIT Physics Seminar Series*, 2016, Heidelberg, Germany

Erklärung zur Dissertation

Hiermit versichere ich, dass ich die vorliegende Dissertation selbstständig angefertigt und keine anderen als die angegebenen Quellen und Hilfsmittel verwendet habe. Alle wörtlichen und paraphrasierten Zitate wurden angemessen kenntlich gemacht. Die Arbeit hat bisher noch nicht zu Prüfungszwecken gedient.

Darmstadt, den 12.04.2019

_____

(M.Sc. Martin Schanz)